THERMAL STRESS EVALUATION OF THERMO-BLAST JET NOZZLE MATERIALS

I.A. GORLACH

Thesis submitted for
the degree of Philosophiae Doctor in Mechanical Engineering
at the North-West University

Promoter: **Prof. J. Markgraaff**
Assistant Promoter: **Dr. A. Kolesnikov**

2004

Potchefstroom

PREFACE

To my wife, Irina

I would like to thank Prof. J. Markgraaff for his support and guidance during my studies at the Potchefstroomse Universiteit vir Christelike Hoër Onderwys.

SUMMARY AND KEY TERMS

In the last few years a new method for surface preparation has evolved, namely thermo-abrasive blasting. This technique utilises a high enthalpy thermal jet to propel abrasive particles. The thermo-abrasive blasting gun, also called a thermal gun, is based on the principles of High Velocity Air Fuel (HVAF) processes. Nozzles used for thermo-abrasive blasting are subjected to thermal loading, wear and mechanical stresses. Therefore, the nozzle geometry and materials are critical for reliable performance of a thermo-abrasive system. In this investigation, the thermal stresses developed in the nozzle materials for thermo-abrasive blasting were analysed. The analytical and the computational models of the thermo-abrasive gun and the nozzle were developed. The computational fluid dynamics, thermal and structural finite element analyses have been employed in this study. The nozzle materials investigated were tungsten carbide, hot pressed silicon carbide, nitride-bonded cast silicon carbide and SIALON.

The simulation and experimental results show that the highest thermal stresses occur during the first two minutes from the start of the thermal gun. However, thermal stresses are also high after the system is shut off. The nozzle geometry was optimised, which provided high cleaning rates with evidence of improved thermal loading, based on the experimental results.

A new design of the thermal gun and the ignition method associated with a HVAF system were developed in this study.

It is also concluded that the computation fluid dynamic and the finite element technique can be used to optimise the design of thermo-abrasive blasting nozzles.

Keywords: HVAF, Nozzle, Thermal stresses

LIST OF ILLUSTRATIONS

Page number

Background

Section 1

Section 2

Section 3

Section 6

Section 7

CONTENTS

4. DESIGN OF THE THERMAL GUN

5. COMPUTATIONAL MODELLING OF THE THERMAL GUN

6. FINITE ELEMENT ANALYSIS OF THE NOZZLES

BACKGROUND

The increasingly competitive world market demands shorter throughput times for products and services. Metal fabrication requires the preparation of surfaces for painting, coating and other processes. Therefore, the target for the surface preparation industry is to clean the manufactured steel in the shortest possible time and to provide good surface quality for adhesion of paints and other coatings.

Abrasive blasting is the most common method of surface preparation. Conventional abrasive blasting methods use a stream of high velocity air to propel abrasives against the surface to be cleaned. Figure 1 shows the schematic of a conventional abrasive blasting system. Compressed air is supplied to a pressure blast unit and blasting hoses. Abrasives are forced out of the pressure blast unit by the air into the hose and out through a blasting nozzle. The blasting nozzle accelerates the abrasive particles, which in turn bombard a surface, thereby removing scale and coatings.

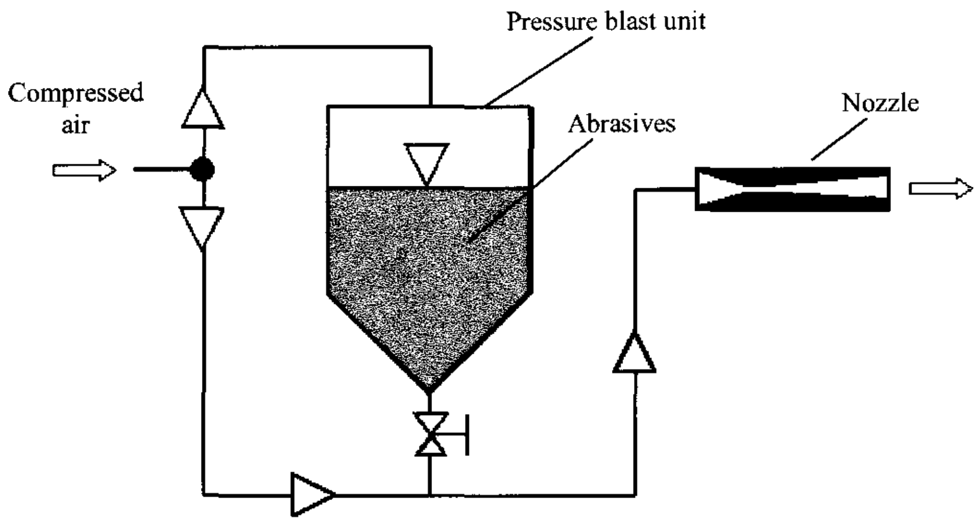

Figure 1. Schematic of a conventional abrasive blasting system

Despite numerous developments in nozzle design, the productivity of conventional abrasive blasting methods is still mainly dependent on the power output of the compressor being used. Conventional abrasive blasting systems have reached their limit in terms of performance, mainly due to the difficulties of obtaining and maintaining the high pressure of required compressed air.

Conventional abrasive blasting methods are inefficient when the coating to be removed is hard or elastic like rubber or polyurethane. However, the biggest drawback of conventional sandblasting is moisture and impurities introduced by the compressor, which contaminate cleaned surfaces.

In the yearly 1980's, a new method of using a ram-jet engine (Fig. 2) for propelling particles appeared in American and Russian patents (Browning, (1983), Galchenko, (1982)). This method of abrasive blasting is called thermo-abrasive blasting because combustion is the major source of energy for the propulsion of abrasives. Combustion of fuel releases heat and generates a high temperature pressurized gas, which is directed through a nozzle to form a high velocity flow stream. Modifications of the ram-jet engine, whereby abrasive particles are introduced into the gas flow and accelerated by it, led to the design of an apparatus called the thermo-abrasive gun or in short thermal gun.

The combustion process generated by a thermal gun is classified as High Velocity Air Fuel (HVAF) or High Velocity Oxy Fuel (HVOF) process depending on the oxidizer. HVOF processes have been successfully applied in metal spraying for a decade. HVAF processes, on the other hand, are not used in industry and very little scientific data is available.

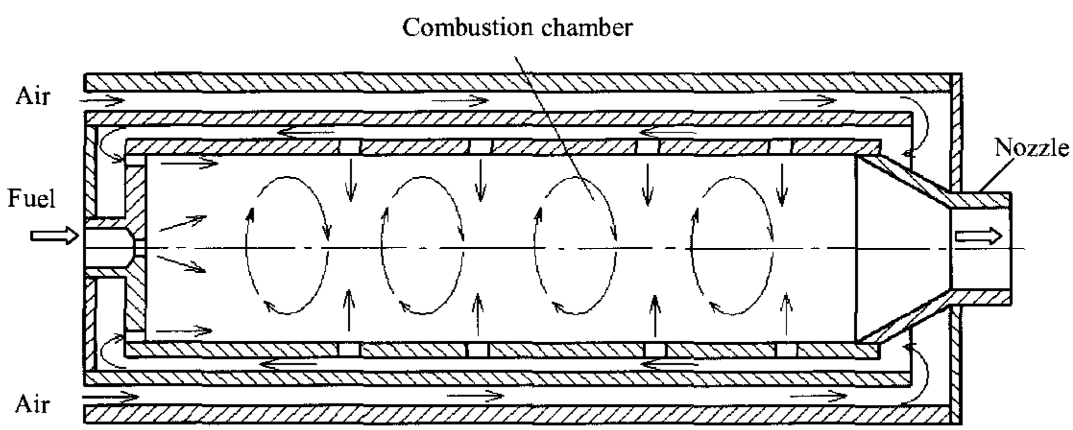

Figure 2. Simplified schematic of a ram jet engine

Over two decades attempts were made to produce thermal guns for thermo-abrasive blasting, for example, Browning's thermal gun (1993), Galchenko's thermal gun (1982) and Evdokimenko's thermal gun (1997). However, it appears that up to date thermal guns for thermo-abrasive blasting did not find an application in industry.

In 2000 the author, together with Mr. S. Kotov, developed a thermal gun prototype, Kotov (2000). This prototype featured a regenerating air supply method similar to a ram-jet engine (Fig. 2) and the abrasive delivery nozzle positioned in the centre of the combustion chamber at some distance from the nozzle (Fig. 3).

The features and description of the thermal gun prototype are as follows:

- The thermal gun prototype has three housings, a fuel valve, an injector, a nozzle and two electric spark electrodes (Fig. 3).

- The three concentric housings are used for the regenerating air supply, where the compressed air is used for combustion and cooling of the housings.

- Liquid fuel under pressure is delivered to fuel valve 6, which has needle 8. The primary goal of needle 8 is to regulate the amount of fuel delivered to the system. The needle has a cylindrical part and a tapered end. The cylindrical part provides an annular passage for the fuel, hence dispersing the fuel. The gap between the tapered end and the delivery opening of fuel valve regulates the amount of fuel when needle 8 moves up and down.

- The bottom of the fuel valve is positioned inside of the gun concentric with the radial hole of fuel injector 7 with gap D. The end of the fuel valve and the radial hole of fuel injector have chamfers, therefore, creating an annular passage for the air. Gap D allows about 10% of the compressed air to go into fuel injector 7 braking fuel into droplets, thus providing a first stage of fuel/air mixing.

- Fuel and air mix further in annular passage E, which is formed by the inner core of fuel injector 7 and nozzle 9. In the annular passage the second stage of fuel/air mixing takes place. The fuel/air mixture is then ejected through holes F of fuel injector 7 into combustion chamber G, which are positioned at an angle to the axis of the gun. Going though holes F, the mixture is broken into small droplets of high velocity.

- The main stream of compressed air is directed first to annular passage A. Then it goes through holes B in nozzle holder 4 and into annular passage C. A portion of this air enters combustion chamber G through radial holes H in combustion chamber housing 3.

The rest of the air turns around and goes through the spiral grooves of fuel injector 7 into combustion chamber G. The spiral groove gives a swirling movement to the air. While going through annular passage C the air heats up by absorbing the heat from combustion chamber housing 3 while cooling it. The two streams, fuel/air mixture and hot swirled air, intersect with each other at the entrance of combustion chamber G, creating turbulence. This is a final stage of fuel-air mixing.

- Combustion chamber housing 3 has the rows of radial and tangential holes H. These holes are important for various purposes. Firstly, they bring the oxidizer in along a combustion zone providing a stable combustion process in varying conditions. Secondly, they bring in cold air, which protects the combustion housing from overheating and subsequent collapsing. Thirdly, the radial holes help to hold a flame inside the combustion zone providing complete burning of the fuel.

- Ignition of the fuel/air mixture is achieved by means of an electric spark between two electrodes positioned inside the combustion chamber. The gap between the electrodes is 2 mm. An electronic ignition transformer provides a high voltage spark (14 kV). The supply voltage of the transformer is 12V DC. The power can be drawn from a car battery. This gives the thermal gun mobility, which is needed for applications in areas where there is no electricity. The gun is started at low volumes of the fuel/air mixture. Once started the combustion process is self-sustaining.

- The abrasive/air mixture is supplied through delivering nozzle 9 (Fig. 3). The flow is then directed through a converging-diverging nozzle.

The schematic of the thermo-abrasive blasting system is shown in Figure 4. The thermo-abrasive blasting system consists of a thermal gun with a blasting nozzle, a pressurized fuel container, a fuel line and a compressed air line for combustion. The compressed air is supplied to the sandblasting unit, which delivers abrasives to the thermal gun, similar to a conventional sandblasting system.

1. Outer housing
2. Middle housing
3. Combustion chamber housing
4. Nozzle holder
5. Nozzle
6. Fuel valve
7. Injector
8. Fuel regulating Needle
9. Sand delivery nozzle
10. Air delivering housing
11. Spark Electrode

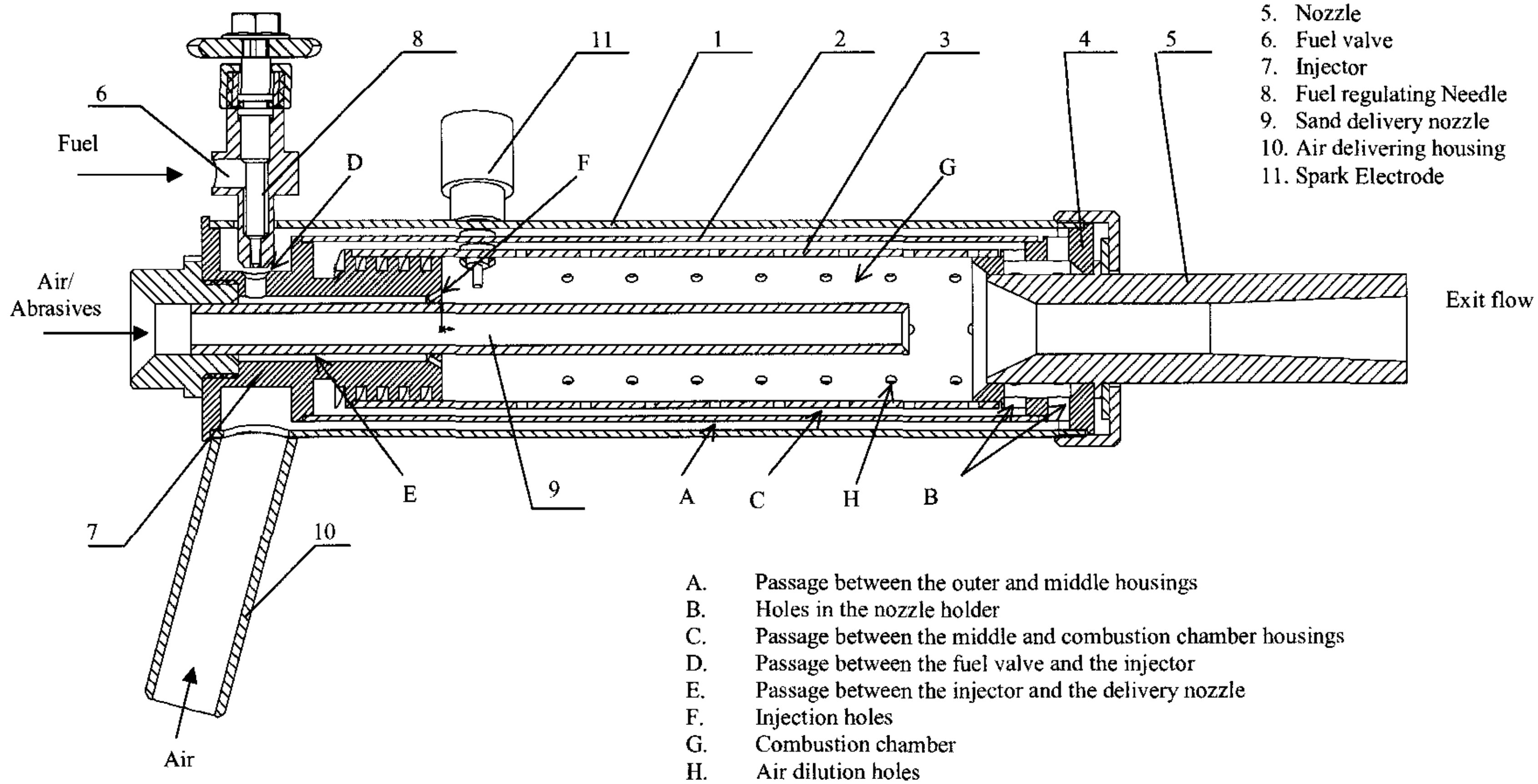

A. Passage between the outer and middle housings
B. Holes in the nozzle holder
C. Passage between the middle and combustion chamber housings
D. Passage between the fuel valve and the injector
E. Passage between the injector and the delivery nozzle
F. Injection holes
G. Combustion chamber
H. Air dilution holes

Figure 3. Schematic cross section of the prototype of the thermal-gun

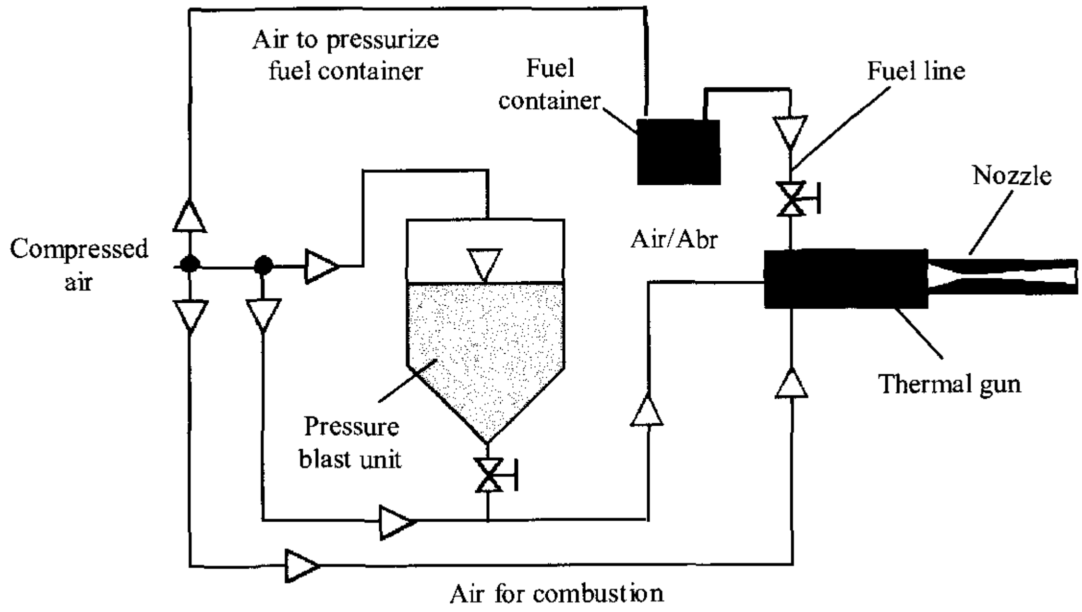

Figure 4. Schematic of the thermo-jet system for abrasive blasting

The rate of cleaning using the thermo-abrasive blasting is higher due to higher particle velocities. The high temperature jet also improves the quality of blasted surfaces as a result of a heat factor, which is responsible for removal of impurities, oil and moisture from surfaces. Also, due to the heat factor, the painting process can be done in cold weather, and in general the curing time of paint is reduced.

The thermal gun prototype was successfully used for the removal of:

- metal coatings from dam gates at Vaal Dam,
- rubber from mining equipment and pipes,
- ceramic coatings from chemical equipment,
- polyurethane from components in the automotive industry,
- hard scale from components after sand casting.

In all the above applications the cleaning rate obtained was far better than with a conventional sand blasting system. In many instances, a conventional system failed to do the job at all. An economic comparison of the blasting methods showed that thermo-abrasive blasting is twice as economical as conventional blasting (See page E 9 of Appendix E).

PROBLEM STATEMENT

During trials, the following problems associated with thermo-abrasive blasting were identified:

Short life of the blasting nozzle

- Practical experience showed that the biggest drawback of thermo-abrasive blasting is the short life of blasting nozzles due to extreme conditions combining heat, abrasive wear and mechanical stress.

- Initially the blasting nozzles were made of heat resistant steel, which retains its hardness at high temperatures. Nevertheless, due to abrasion, the nozzles wore out in a short time period.

- Attempts were made to use conventional blasting nozzles made of tungsten carbide and ceramic (SIALON). Trials showed that the tungsten carbide nozzles deteriorated by flaking on the outer surface due to heat. The SIALON blasting nozzles cracked during the start-up of the thermal gun, which was attributed to the thermal shock.

- Furthermore, it was noticed that cleaning rates, whether using short or long thermo-jet nozzles, were not substantially different, although traditionally long blasting nozzles provide much higher cleaning rates than short nozzles in conventional abrasive blasting. This raised concerns regarding optimum nozzle geometry for thermo-abrasive blasting.

Limiting power output of the thermal gun prototype

The thermal gun prototype provided a stable performance and good overall results. However, it was noticed that the power of the thermal gun was limited and could not be increased further even if more fuel was provided. It is believed that the main reasons for this were the way the air and fuel mixed, as well as the small size of the combustion chamber.

Furthermore, poor mixing of the fuel and the compressed air did not provide reliable ignition, especially at low temperatures.

Unreliable ignition

A small combustion volume and the requirements of mobility create difficulties in designing a compact and efficient ignition system. A high voltage spark gives the highest temperature, which ignites fumes easily. However, the spark plug points may get wet from paraffin, thus insulating them, preventing a spark.

1. LITERATURE SEARCH

1.1 High Velocity Air/Oxy Flame Systems

The closest system in terms of the combustion process to the thermal abrasive gun is a HVOF system. HVOF systems are used in thermal spraying. Thermal spraying incorporates a number of processes whereby molten/semi-molten material is deposited at high velocities by gas onto a surface. Typical types of coatings applied to surfaces using thermal spraying are metals, cermets, ceramics, carbides, intermetallics, or a combination of any of these material groups. Wire or fine powders are the most commonly used thermal spraying consumables. Thermal spraying can be divided into two major designs, low or high velocity processes. The biggest difference between high and low velocity processes is the coating quality. Low velocity processes produce coating particle sizes larger than 100 μm in diameter. These particles, when they oxidize during application, produce large undesirable oxide structures. With high velocity techniques, the particle sizes are small by comparison, and any oxides formed are of sub-particle size and well bonded between the metal layers. High particle velocities, furthermore, result in better bonding to the substrate. All metal spray applications are done using the high velocity equipment. A schematic of cross section of thermal spray gun is shown in Figure 1.1.

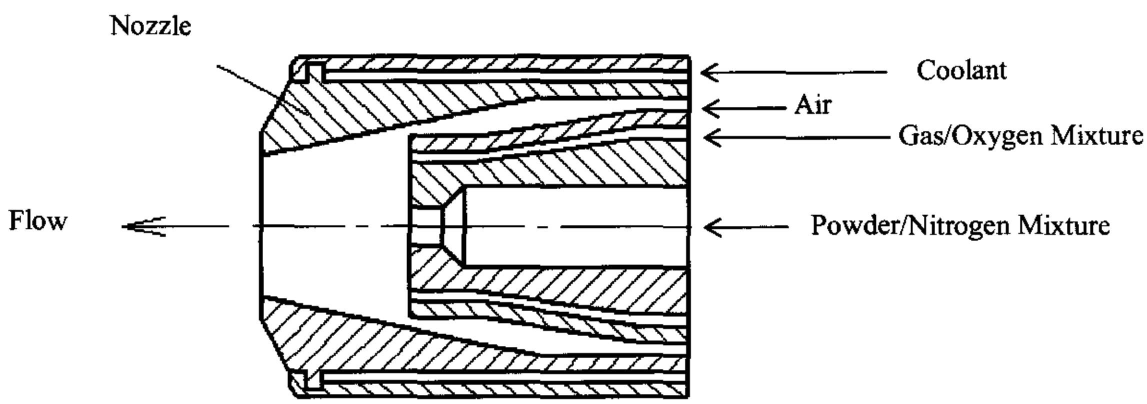

Figure 1.1. Schematic cross section of a thermal spray gun, Mostaghimi (2003)

HVOF is a process in which a mixture of fuel and oxygen ignites in a high pressure combustion chamber and the combustion products are accelerated through a converging – diverging nozzle.

A number of studies have been done on the quality of coatings, simulation of the coating process, application of CFD analysis, etc., in the field of metal spraying with HVOF systems. However, on the topic of analytical modelling of a HVOF system and the nozzle there are only few reported studies. The geometry of a nozzle for thermal spraying does not play such an important role because the particles are fine and are accelerated by the gas over a short distance. The nozzle of the thermal spraying gun is typically cooled by water, therefore, is it not subjected to high thermal stresses. Oberkampf (1996) modelled the internal and external flows in a sonic nozzle during a HVOF process. He assumed that the flow was axisymmetric and used Eulerian and Lagrangian formulations for the gas and particle phases. Sinha (1995) used a Lagrangian stochastic model to predict particle trajectories and the temperature history as a function of particle size and other coating parameters. Mostaghimi (2003) incorporated the above models into one model. Mostaghimi's model consists of several complementary parts and includes sub-models to simulate: (a) gas flow and heating; (b) particle heating and acceleration; (c) impact, spread, and solidification of particles on the substrate; (d) heat transfer within the coating and substrate; and (e) agglomeration of splats and formation of porosity.

Reference to HVAF processes could only be found in literature in applications such as thermal spallation, Turns (2000). Thermal spallation is a technique used for drilling through rocks with high-temperature impinging flames. This technique was invented in the middle of the last century. It was extensively used in Siberia and other regions of the former Soviet Union. Thermal spallation has many advantages over mechanical drilling where rapid drill bit wear or expensive diamond cutters can be a problem. In thermal spallation, the flames rapidly heat the rocks, which crack due to the extremely high temperature gradients near the surface. Such high gradients cause the rock to crack due to the high thermal stresses. Thermal spallation differs from abrasive blasting due to the considerably higher temperature of the flame. Also, thermal spallation does not employ any abrasive particles. Thermal spallation guns are basically burners with short nozzles, which do not wear and are usually made of heat-resistant steel. Examples of the thermal gun for thermal spallation are shown in Figures 1.2 and 1.3. A picture of a thermal gun for thermal spallation is shown on page E11 of Appendix E.

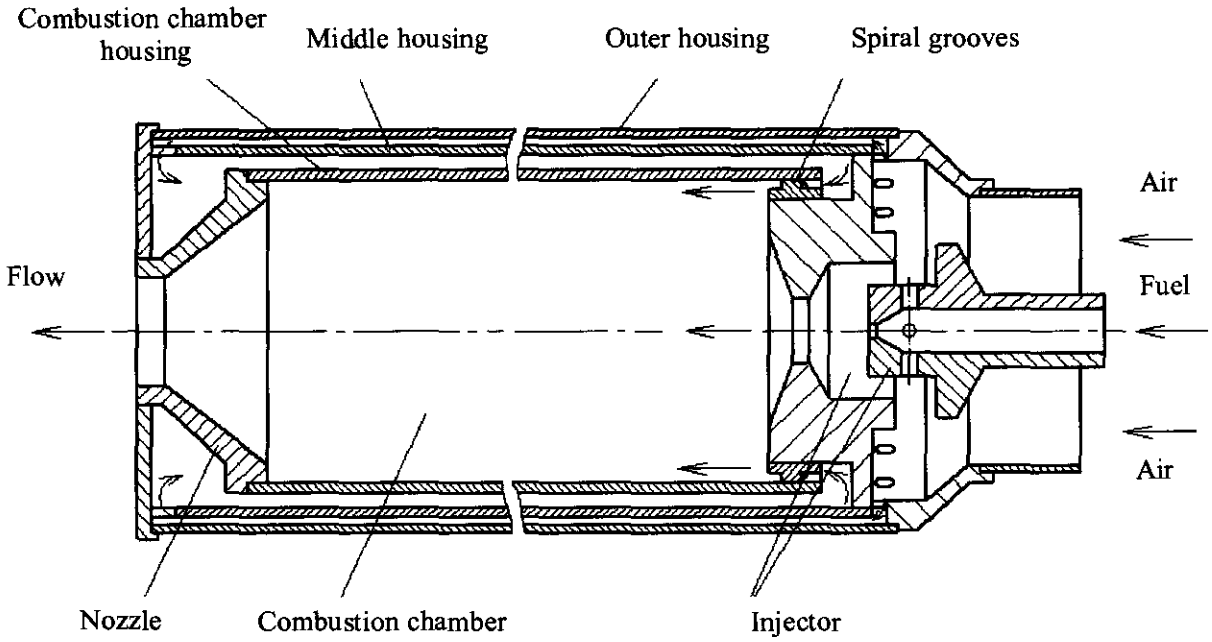

Figure 1.2. Schematic cross section of Varushin's N 1 HVAF gun for thermal spallation, (1973)

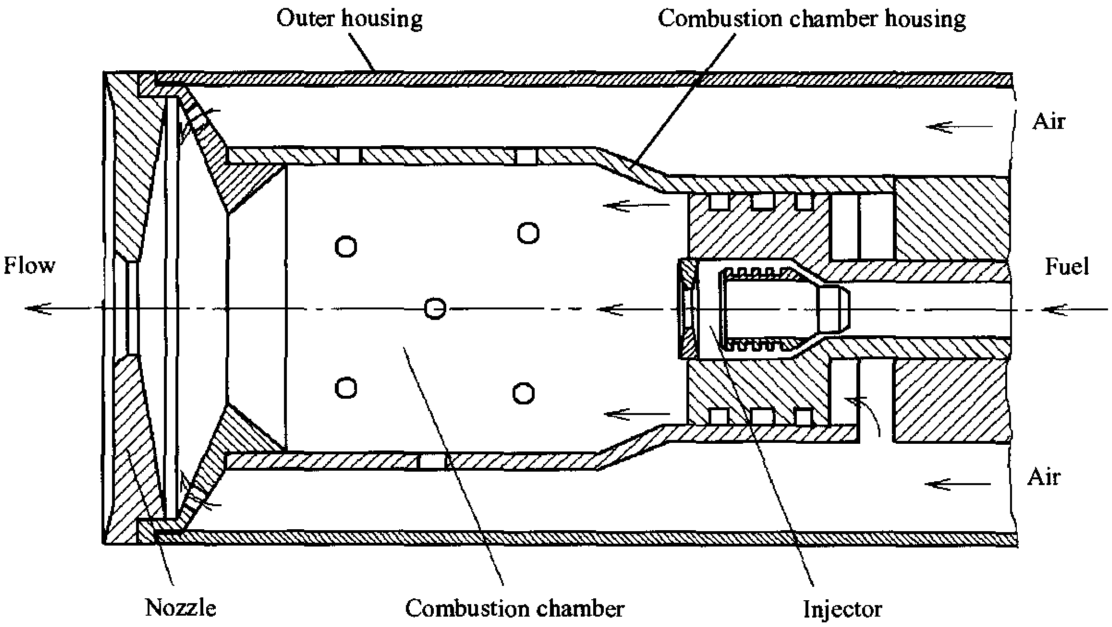

Figure 1.3. Schematic cross section of Varushin's N 2 HVAF gun for thermal spallation, (1973)

Rauenzahn and Tester (1991) studied supersonic flames impinging on rocks in a bore hole. In Rauenzahn's model, the reactant gases were assumed to be at equilibrium, thus the chemical reactions were not modelled. The effect of the chips on the flow field was ignored, so that only single-phase, compressible, axisymmetric, transient fluid flow was modelled. Turbulence was modelled using a combined k-ε technique in the bulk of flow and the traditional law-of–the-wall in the boundary region. The rock surface temperature was calculated using Weibull's statistical failure theory, Weibull (1939). The primary objectives of Rauenzahn's (1991) study were to find the effects of the standoff distance between the nozzle and the rock and the inlet pressure ratio on the heat transfer and the drilled hole radius.

Wilkinson and Tester (1993) studied thermal spallation drilling to further improve the understanding of this phenomenon. The rock temperature was modelled using Dey's thermal spallation rock mechanical model, which is based on a failure mechanism characterized by Weibull's statistical failure theory that requires some empirical parameters. The primary objective was to study the drilling rate and a hole diameter as a function of various parameters, using improved empirical parameters derived from experiments. Compressible, axisymmetric fluid flow and energy equations were discretised, using the finite volume formulation. The chemistry was not directly modelled, but was simulated by varying the gas properties.

Rauenzahn, Tester and Wilkinson's work mainly concentrated on the relationship between the heat and rate of drilling in thermal spallation. Their models did not take into account chemistry and combustion reactions, and only 2-D single-phase flow was simulated. No particle simulation was included because it was not required for the simulation of the thermal spallation of rocks.

Browning (1983) proposed a HVOF thermal gun for abrasive blasting where part of the air is separated from the air/abrasive mixture and used for stabilising the combustion process (Fig. 1.4). The other distinct feature of the Browning's thermal gun is a combustion chamber, which is perpendicular to the flow of abrasives. The thermal gun works on fuel and oxygen. The Browning's thermal gun has a tubular, slotted sand separator that permits air free of sand to pass along the rear side through a bend to the combustion chamber. According to Browning (1983), the air entering the combustion chamber through the radial holes stabilises the combustion.

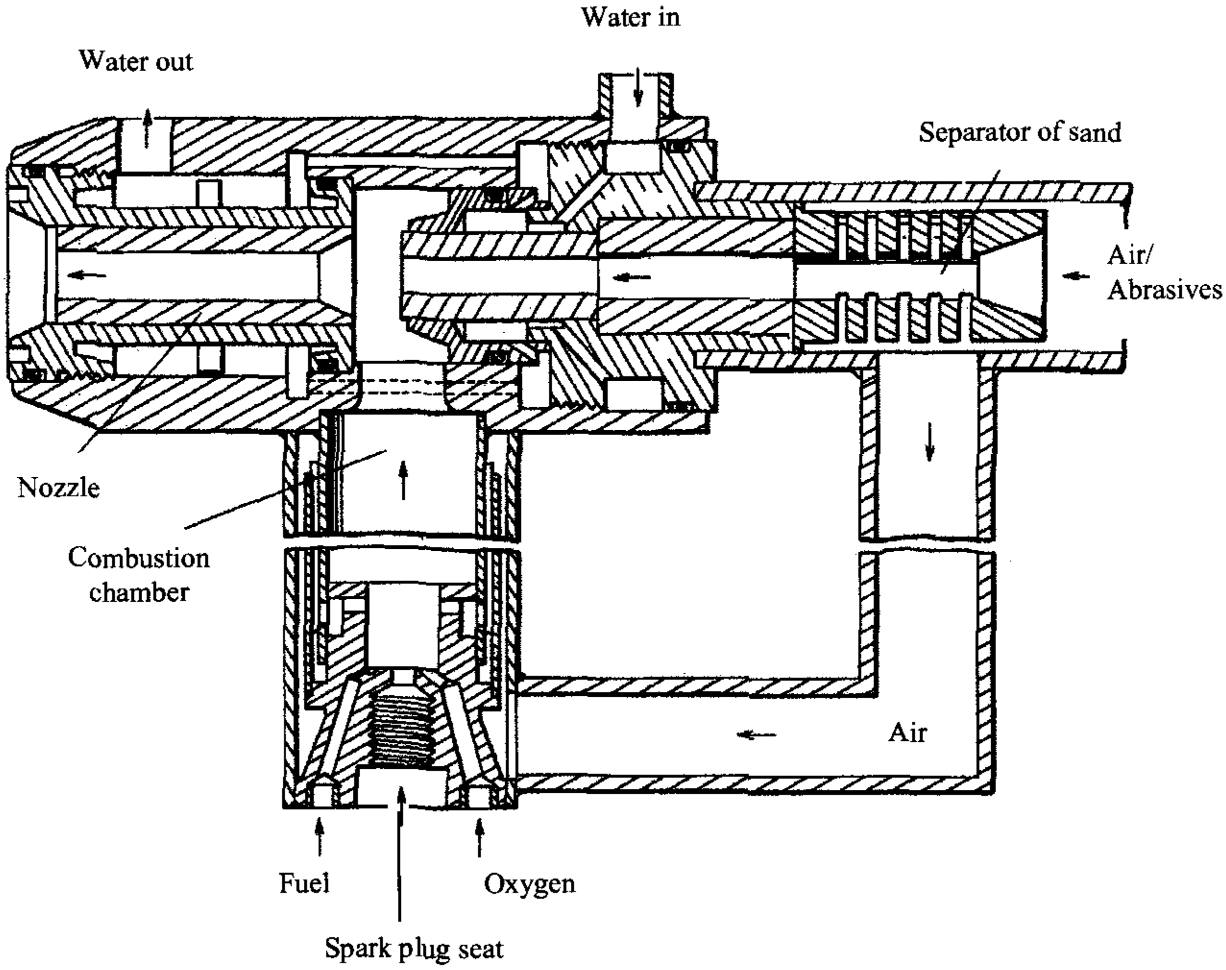

Figure 1.4. Schematic cross section of Browning's HVOF thermal gun, (1983)

The position of the combustion chamber perpendicular to the air/abrasive flow would result in turbulence, which would reduce the flow velocity. The use of a sand separator, in the above patent, implies that all the abrasive particles must be relatively large, which is impractical. In addition, the apparatus requires pure oxygen for operation and water for cooling.

The HVAF thermal gun shown in Figure 1.5 was presented by Galchenko (1982). This thermal gun has a regenerating cooling system, meaning that the main volume of air is used for combustion and for cooling of the parts, especially the nozzle. The blasting nozzle has a wide, but short, diverging section. The main disadvantage of this thermal gun is that it does not provide sufficient mixing of air and fuel because the air, after passing between two chambers, is losing pressure and is not entering through the spiral grooves of the injector.

The author has built a similar thermal gun and tested it. It was found in experiments that the thermal gun had unstable combustion and a low thrust.

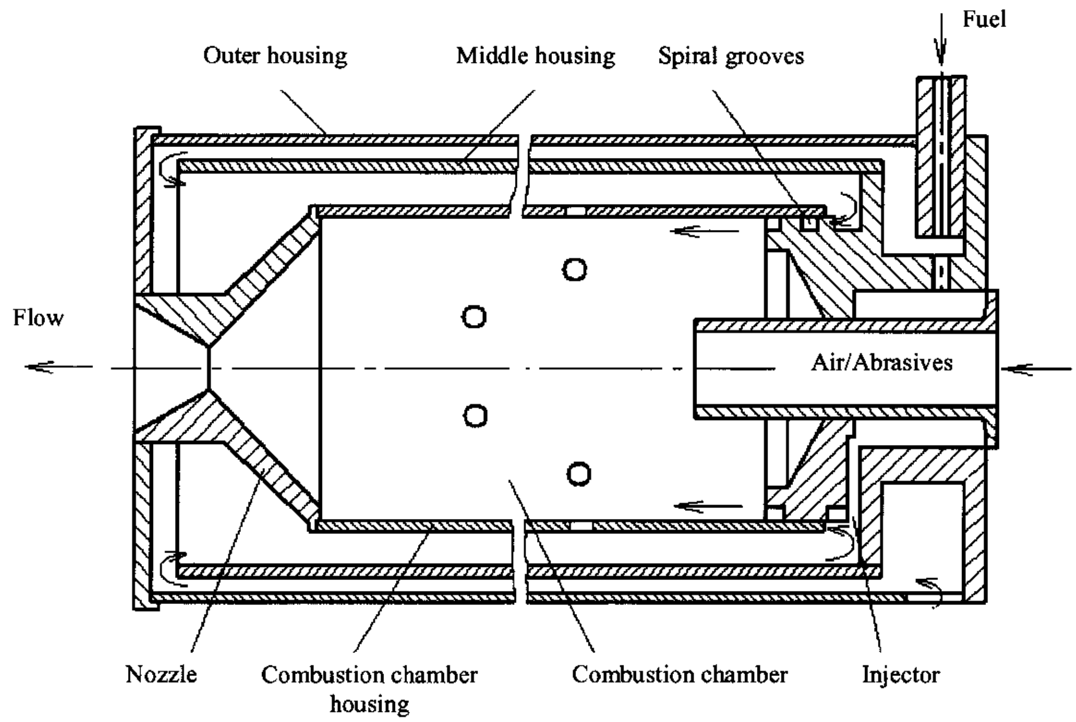

Figure 1.5. Schematic cross section of Galchenko's HVAF thermal gun, (1982)

The HVAF thermal gun shown in Figure 1.6 was presented by Evdokimenko (1997) in a US patent 5607342. Referring to Figure 1.6, the high velocity flame jet apparatus includes a supersonic gun with a main combustion chamber having two parts, one of which is air-cooled and the other of which is water cooled. The air-cooled portion of the chamber is provided with radial air inlet holes to allow the cooling air to enter the chamber and stabilize combustion. The water-cooled portion of the chamber is elongated and terminates in a bend. A powder sprayer is arranged axially in the bent end of the combustion chamber. A removable exit nozzle is coupled to the end of the combustion chamber. Different nozzles are used for abrasive treatment and coating treatments. The first portion of the combustion chamber is provided with an ignition device attached to a gun. The removable igniter is connected to fuel and oxygen sources and supplies the flame to the combustion chamber when the apparatus is started. After the gun is ignited, the igniter is removed.

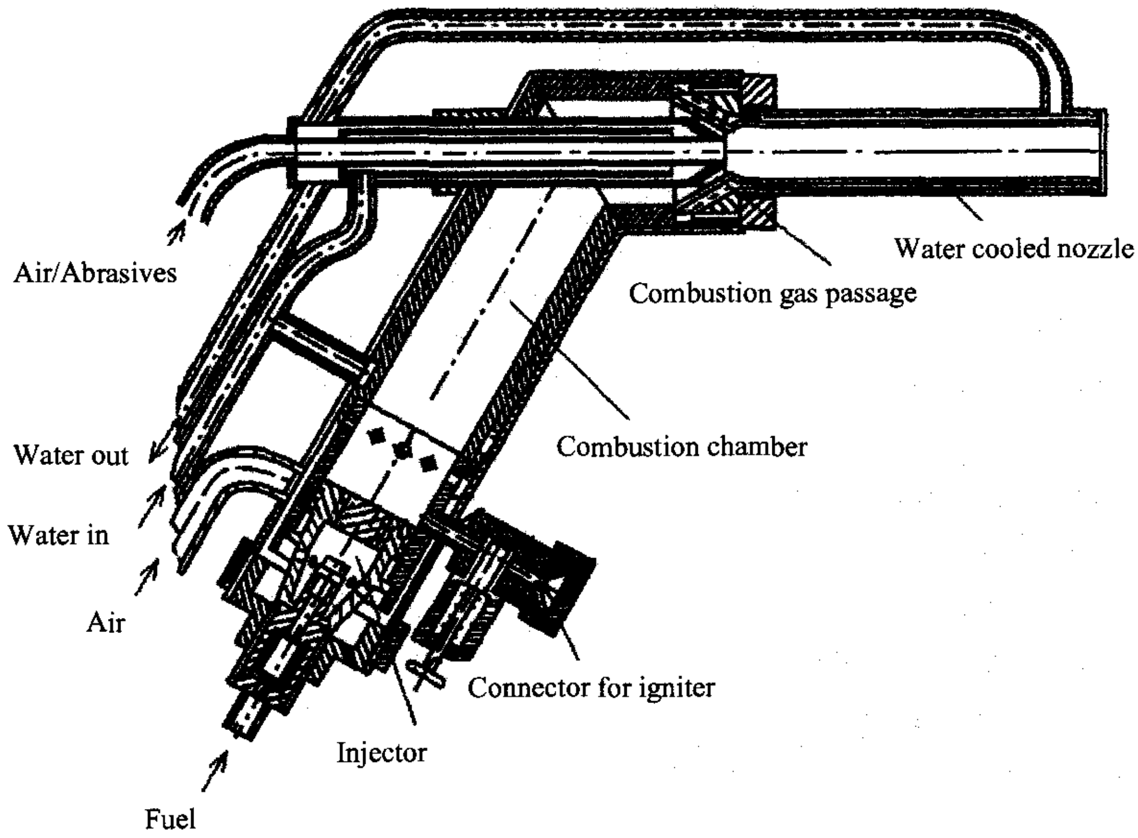

Figure 1.6. Schematic cross section of Evdokimenko's HVAF thermal gun, (1997)

In the above design, the fuel mixes with cold air ultimately reducing the specific heat coefficient of the mixture. Another disadvantage of Evdokimenko's apparatus is that the fuel-air mixture cannot be regulated, which is impractical. Furthermore, the apparatus requires oxygen for starting up and water for cooling during operation.

All of the above thermal guns have not found general applications in abrasive blasting due to many factors, such as low cleaning rates, complexity, reliability etc. In general, a thermal gun should have a high efficiency under varying process conditions and provide sustainable performance over a long period of use. The ignition system of the thermal gun should be simple and reliable. The parameters of a thermal gun should be regulated and controlled with ease by an operator. It is suggested that, for economic and safety reasons, a thermal gun should utilize liquid fuels, such as diesel or paraffin, and not oxygen and gas or petrol. The requirement of water cooling complicates the design and operation of thermal guns and should be avoided.

1.2 Nozzle Design

1.2.1 Abrasive Blasting Nozzle Designs

In sandblasting applications, the air/abrasive flow is directed out through a blasting nozzle. A nozzle has three main features, a converging section, a throat and a bore. The bore of a nozzle can be straight or diverging (Fig. 1.7). If a nozzle has converging - diverging geometry it is called a Laval (or Venturi) type of nozzle.

Considerations in the design of the nozzle include:

- throat diameter,
- exit diameter,
- included angle of the diverging section,
- length of the diverging section,
- length of the converging section.

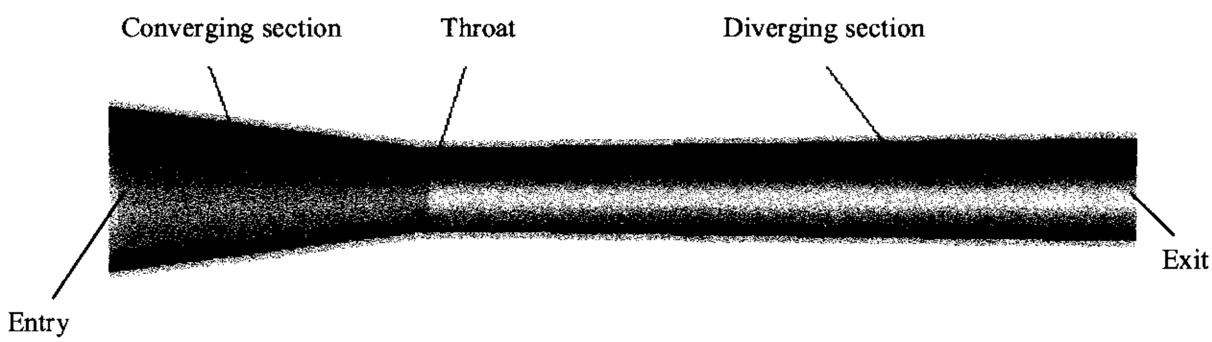

Figure 1.7. Abrasive Blasting nozzle

The development of abrasive blasting nozzles has a long history, with some patents registered in the beginning of the 20th century. Up to the 1950's, only straight bore nozzles were used for sandblasting, Seavey (1985). It was then observed that blasting becomes more efficient as the nozzle exit diameters eroded. This led to the development of a converging-diverging shape of nozzle geometry currently used in conventional abrasive blasting. In further studies to improve nozzle efficiency, examinations of various modifications in nozzle sizes and contours were done.

As it appears in literature, the Laval nozzle was never actually transferred to abrasive blasting, but rather evolved there on its own. The Laval nozzle is often referred to as a Venturi nozzle.

In the last twenty years, a number of studies were done on the topic of nozzle design for conventional blasting. But up to the 1980's, there was no evidence of a scientific approach to abrasive nozzle design. Seavey (1985) studied long Laval nozzles for sandblasting. These studies revealed that there is little or no particle acceleration up to the nozzle throat. Figure 1.8 shows the relationship between nozzle length, gas velocity and particle velocity, indicating that the particle velocity depends on the length of the diverging part. According to Seavey (1985), at an air velocity below Mach 2 and in a 180 mm long nozzle (diverging section), the particle velocity reaches 230 m/min for 870 μm sand particles.

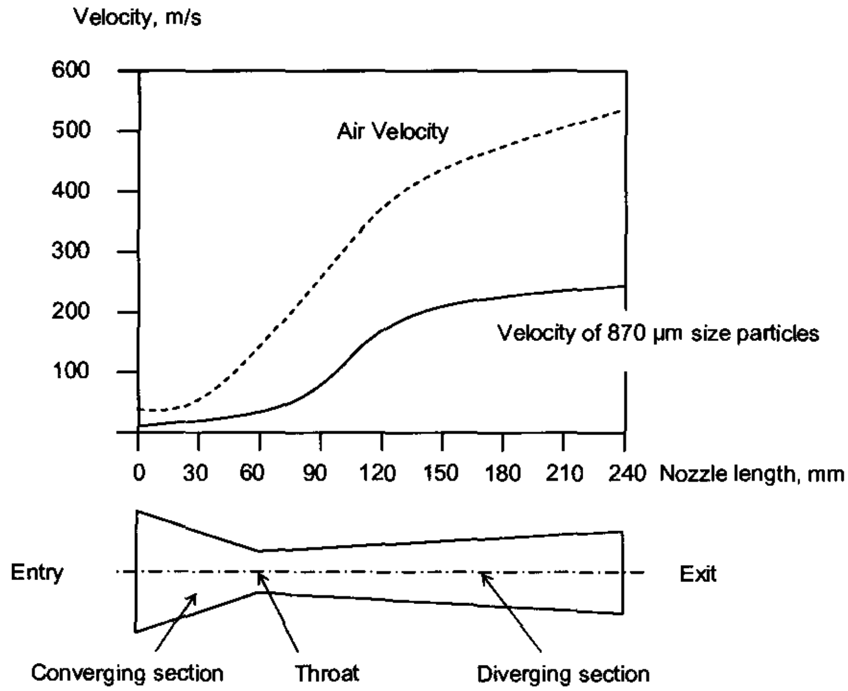

Figure 1.8. The relationship between nozzle length, air velocity and particle velocity, Seavey (1985)

There were attempts to the transfer technology of rocket nozzles to abrasive blasting nozzles. Settles and Garg (1995) investigated the relationship between the nozzle design and productivity, and suggested the use of a 150 mm Laval type of nozzle.

Settles and Garg (1995) measured velocities for particle sizes between 10 μm and 1000 μm. At an air volumetric flow rate of 6 m^3/min, a pressure of 7 bar and a nozzle throat diameter of 9,5 mm, the particle velocity attained was 173 m/s for 870 μm sand particles, while the air velocity reached Mach 2. For 100 μm particles, velocities of up to 350 m/s were reported [Settles, 1995:35]. At a size of 1000 μm, particles basically did not accelerate, whereas 10 μm particles approached the air stream velocity.

It is generally accepted that three factors influence productivity of blasting. These are:

- correct nozzle geometry,
- running a nozzle at the designed pressure,
- smallest possible size of grit.

Running a nozzle at the designed pressure means selecting the throat and exit diameters according to the power output of the compressor. Settles and Garg (1995) suggested that there is a linear relationship between the area ratio and the design pressure (Fig. 1.9). The area ratio is

$$\text{Area Ratio} = \left(\frac{\text{Exit Diameter}}{\text{Throat Diameter}}\right)^2 \qquad [1.1]$$

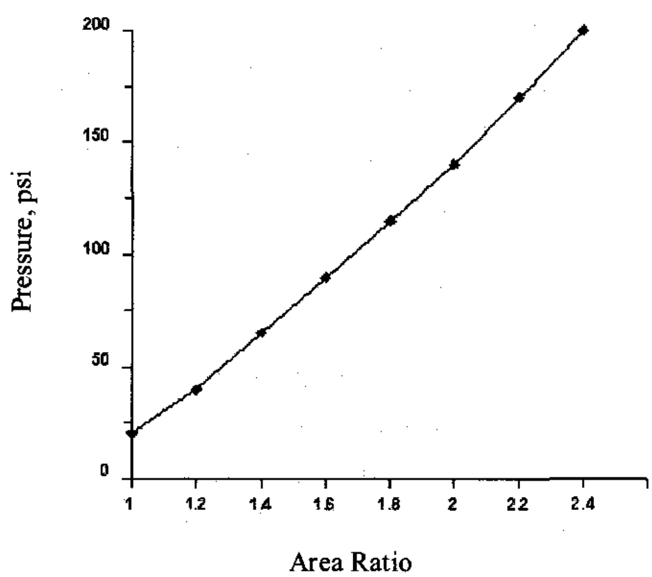

Figure 1.9. Nozzle pressure versus nozzle area ratio, Settles and Garg (1995)

Settles's calculated the flow using a two-phase flow of air and particles. However, Settles's model did not include particle collision and coupling of the dispersed and continuous phases. Also, the calculations did not include thermodynamics of a high enthalpy flow, which is thought to take place in a thermo-abrasive jet gun.

The size of the nozzle throat also plays an important role in the working conditions of sandblasting, as it gives rise to thrust. In general sandblasting, a thermal gun is a handheld apparatus. An operator's fatigue must be taken into account. Glushko (1973) suggested that the nozzle throat area can be determined as follows [Glushko, 1973: 23]:

$$A_{throat} = \frac{F}{C_T \cdot p} \qquad [1.2]$$

where F = the thrust, N,

p = the pressure in the nozzle, MPa,

C_T = the thrust coefficient, which depends on the nozzle pressure, (Fig 1.10).

If the limiting thrust is not to be exceeded the trust coefficient C_T increases with a pressure, hence reducing a nozzle throat diameter. For example, if a thrust is limited to 100 N then at the pressure of 1 MPa and C_T = 1,2 the nozzle diameter, according to equation [1.2], should not exceed 10 mm.

Glushko (1973) further suggested the use of a flanging coefficient for calculating the exit diameter of the nozzle as follows:

$$D_{exit} = \varphi \cdot D_{throat} \qquad [1.3]$$

where D_{throat} = the throat diameter of nozzle, mm,

φ = the flanging coefficient, (Fig 1.10).

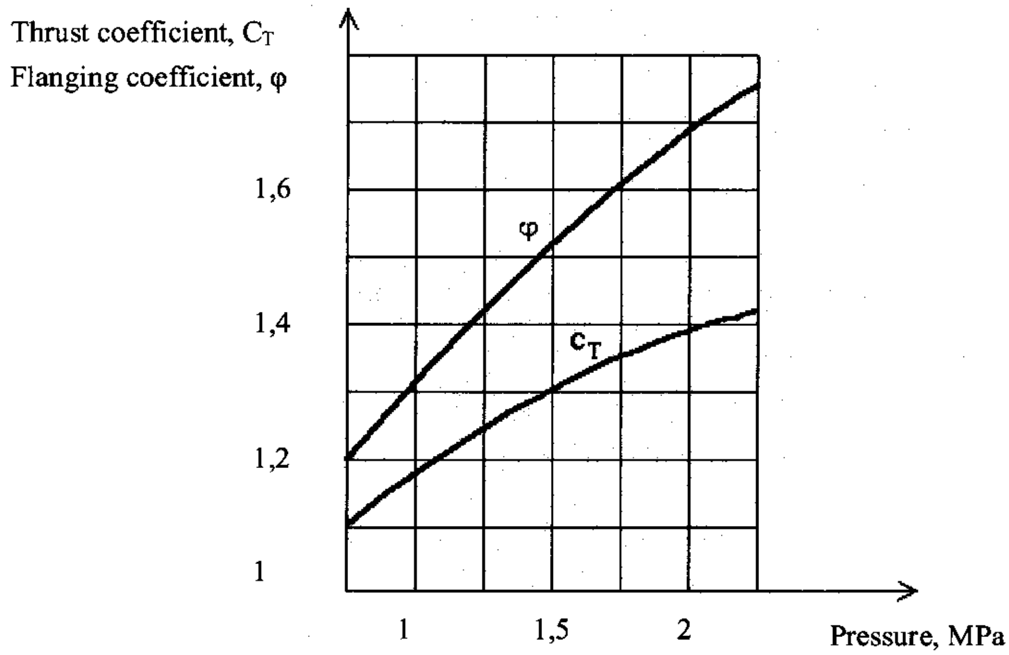

Figure 1.10. Thrust and flanging coefficients versus pressure, Glushko (1973)

According to Glushko (1973), it appears that the exit diameter of the nozzle also plays an important role in reducing the thrust as it depends on the pressure. This suggests that high pressure nozzles should have a wide exit.

Figure 1.11 shows different nozzle designs used for conventional abrasive blasting. Straight bore nozzles (Fig. 1.11a) are mainly used for low pressures of 4 - 5 bar, in suction blasting systems or when the application requires a bead pattern (www.airblast.com). The straight bore nozzle gives a concentrated blasting pattern. Venturi-type nozzles are more productive than straight bore nozzles because they increase particle velocity and create a wider blasting pattern (Fig. 1.11b). The Venturi nozzle with a wide opening exit, called Bazooka™, is used for higher pressures in the region of 12 bar (Fig. 1.11c).

According to the studies done by the author, the majority of companies in South Africa and Europe use compressors producing a 250 CFM flow rate at 5 – 7 bar pressure. At pressures above 7 bar the operator's fatigue is far too high, due to thrust. Double Venturi bore nozzles (Fig. 1.11d) were designed to increase productivity by means of suction of atmospheric air through an additional opening and boosting air velocity. However, according to data obtained from Storm Machinery (Pty) Ltd, in practice, it does not give a significant increase in productivity.

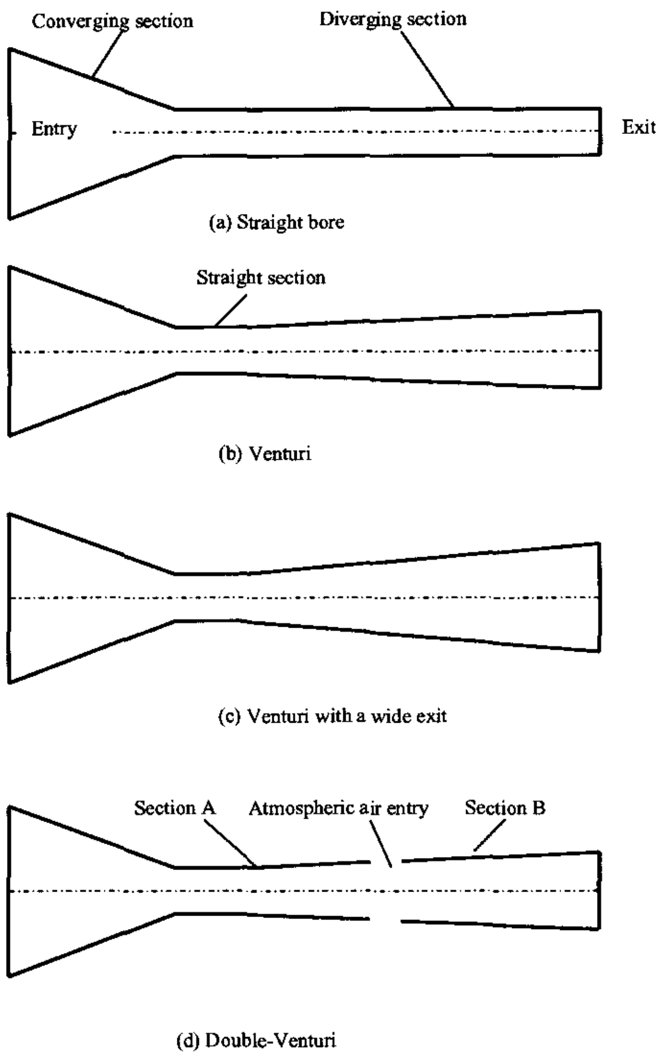

Figure 1.11. Abrasive blasting nozzle designs, (www.airblast.com)

1.2.2 Nozzle Design - Multiphase Flow Approach

Gas and particle velocities are determined by the physics of air/abrasive flow, which is a multiphase flow described by coupling effects between phases. Many years ago multiphase flow was a subject of study in pneumatic conveying of solids, Butters (1981). Later multiphase flow was applied for such processes and systems as plasma coating, water-jet cutting, solid propellant rockets, fire suppression etc.

Multiphase flow consists of a continuous phase, which may be gaseous or liquid, and one or more dispersed phases in the form of solid particles, liquid droplets or gas bubbles. In general, the motion of the dispersed phase is influenced by that of the continuous one and *vice versa* via displacement and inter-phase momentum, mass and heat transfer effects. The strength of the interactions will depend on the dispersed particle's size, density and volumetric loading.

Particle-fluid interaction refers to the exchange of properties between phases and is responsible for coupling in dispersed phase flow. Mass coupling can occur through a variety of mechanisms such as evaporation, condensation or chemical reaction. Because the particles of abrasives are solids, the mass coupling is not used here. Therefore, the two conservation equations, momentum and energy, are used in the calculations. The governing equations of multiphase flows are as follows, Crowe (1998):

The general momentum equation for a particle is

$$m_d \frac{dU_d}{dt} = F_{dr} + F_p + F_{am} + F_b \qquad [1.4]$$

where F_{dr} = the drag force, N,

F_p = the pressure force, N,

F_{am} = 'virtual mass' force, i.e. the force that is required to accelerate the carrier fluid 'entrained' by the droplet, N,

F_b = general body force term which represents the effects of gravity, N,

U_d = the particle velocity, m/s,

m_d = the particle mass, kg,

The subscripts *c* and *d* are for continuous and dispersed flows respectively.

In the above formula, the most important is the drag force given by

$$F_{dr} = \frac{1}{2} C_d \rho_c A_d / U_c - U_d /(U_c - U_d) \qquad [1.5]$$

where C_d = the drag coefficient (a function of the 'droplet Reynolds number')

A_d = the area of particle surface, m^2,

ρ_c = the density of the continuous phase, kg/m^3,

U_c = the fluid velocity, m/s,

term $(U_c - U_d)$ is used to establish the sign of the drag force.

The drag coefficient for flows with high Reynolds numbers is as follows:

$$C_d = \frac{24}{\mathrm{Re}_r}(1 + \frac{3}{16}\mathrm{Re}_r) \qquad [1.6]$$

where Re_r = the particle Reynolds number, which is based on relative velocity

$$\mathrm{Re}_r = \frac{\rho_c |U_c - U_d| D_d}{\mu_c} \qquad [1.7]$$

where μ_c = the kinematic viscosity, N s/m^2.

D_d = the particle diameter, m.

When the drag force acts on the particle in a uniform pressure field it is called steady-state drag. No acceleration of the relative velocity between the particle and conveying fluid takes place. Crowe (1998) suggested the use of the following equation of motion for a particle using the steady-state drag coefficient.

$$m_d \frac{dU_d}{dt} = 3\pi\mu_c D_d f(U_c - U_d) + mg \qquad [1.8]$$

where g = the acceleration due to gravity, m/s^2,

f = the drag factor.

The drag factor is determined as follows:

$$f = \frac{C_d \mathrm{Re}_r}{24} \qquad [1.9]$$

Energy coupling can be effected in three ways; radiation, convection and internal heating. Energy conservation is a statement of the first law of thermodynamics for an open system. The first law states that the rate of accumulation of energy in a control volume plus the net efflux of energy across control surfaces is equal to the rate of heat transfer to the system minus the work rate of the system on the surroundings.

$$m_d c_{p,d} = -A_s q_d^{''} + h_l \frac{dm_d}{dt} \tag{1.10}$$

where h_l = the latent heat of phase change, kJ/kg,

$q_d^{''}$ = the surface heat transfer rates per unit surface area,

A_s = the particle surface area, m^2,

$c_{p,d}$ = the particle material specific heat, kJ/kg K.

The surface heat flux, $q_d^{''}$, is given by the following relation,

$$q_d^{''} = h(T_d - T_c) \tag{1.11}$$

where h = the heat transfer coefficient, W/·m^2 °C,

T_d = the particle temperature, K,

T_c = the temperature of the continuous phase, K.

The heat transfer coefficient (h) is evaluated from a correlation applicable in the absence of mass transfer and then multiplied by a correction factor to account for the latter process.

The corrected transfer coefficient is given by

$$h = \frac{kNuZ}{(e^z - 1)D_d} \tag{1.12}$$

where Nu = the Nusselt number,

Z = the particle loading,

k = the thermal conductivity, W/m °C.

Nu is obtained from the following Ranz-Marshall correlation for forced convection effects [Crowe, 1998:103].

$$Nu = 2 + 0{,}6\sqrt{\mathrm{Re}_r}\sqrt[3]{\mathrm{Pr}} \qquad [1.13]$$

where Pr = the Prandtl number.

Thermal coupling between the phases effects the gas velocity. With thermal coupling the gas is cooled down by particles which absorb some heat from the gas. Therefore, the density increases and the velocity of the gas decreases. The coupling effects have to be included in the calculations especially when the volumetric loading of particles is high.

There are two generic approaches for numerical simulation of particles in a fluid namely, the Lagrangian approach and the Eulerian approach. In the Lagrangian approach the velocity, mass and temperature history of each particle is calculated. In the Eulerian approach, the packet of particles is considered to be a second fluid, which behaves like a continuum, and equations are developed for the average properties of the particles. Each approach has its advantages and disadvantages depending on the nature of the flow.

The Lagrangian approach appears to be the commonly used method for solving multiphase flows and determining fluid flow characteristics. The Lagrangian approach is applicable to both dilute and dense flows. If the flow is steady and dilute a form of the Lagrangian approach, known as the trajectory method, is used. If the flow is unsteady, the more general approach is the discrete element method.

In the discrete element method, the motion and position of individual particles are tracked with time. Due to practicality, the number of particles is reduced by forming a parcel of particles. It is assumed that the parcel of particles moves through the field with the same velocity and temperature as a single particle. The parcel is identified as a discrete element. The motion of each parcel over one time interval is obtained by interpolating the parcel motion equation. At the time, the particle temperature, velocity and other properties can be calculated. At every time step, the properties of the particle can be determined by summing over all the particles in a computational volume (source terms).

The Lagrangian approach can include two methods, primitive variable formulation and conservative variable formulation. The primitive variable formulation method involves particle pressure-velocity formulation directly. The continuity equation is checked for every cell. This approach is suitable for incompressible flows where a density is constant. For compressible flows, the continuity equation does not converge easily. Therefore, the conservative variable formulation method is applied.

In the primitive variable formulation method the pressure inlet and outlet boundary conditions are specified and the solution provides the mass flow. The conservative variable formulation method differs from the primitive variable formulation method in that the inlet conditions are the initial conditions and the solution provides the outlet pressure and velocity. The conservative variables are useful because they do not change rapidly in a compressible flow, therefore, the computational grid does not have to be very fine. The other big advantage is that the conservative variables are constant across a shock wave. However, once one has solved for the conservative variables it is necessary to recalculate the primitive variables such as pressure, temperature and velocity.

For multiphase flows in dusts or nozzles, the fluid velocity is determined as follows [Crowe, 1998:248]:

$$U_c = \frac{\gamma}{\gamma+1}\cdot\frac{Y}{X}\left[1 \pm \left(1 - 2\frac{XZ}{Y^2}\cdot\frac{\gamma^2-1}{\gamma^2}\right)^{\frac{1}{2}}\right] \qquad [1.14]$$

where X, Y and Z are conservative variables determined by

$$X = \rho_c U_c A \qquad [1.15]$$

$$Y = (\rho_c U_c^{\ 2} + p)A \qquad [1.16]$$

$$Z = X\left(\frac{\gamma}{\gamma-1}\cdot\frac{p}{\rho_c} + \frac{U_c^{\ 2}}{2}\right) \qquad [1.17]$$

where A = the cross sectional area of the nozzle, m^2,

γ = the ratio of the specific heat at constant pressure c_p to the specific heat at constant volume c_v.

The nozzle sectional area is presented in all the three conservative variables. Hence, the change of the nozzle diameter determines the flow velocity along the nozzle axis.

In equation [1.14], the minus sign is for a converging section and the plus sign is for a diverging section of the nozzle. If the initial velocity was chosen too high the condition of unity will be achieved before the flow reaches the minimum area at the nozzle throat and a solution is not possible (the term on the right hand side becomes negative). This means the calculation will be invalid for the rest of the nozzle. The sonic condition should be achieved at the nozzle throat. After this condition is established, the calculation is repeated with the sign on the discriminant changing from minus to plus at the nozzle throat. The flow thereafter is supersonic.

If the exit pressure is higher than or equal to the back pressure, no further changes in the calculations are needed. This corresponds to under-expanded or ideally expanded nozzle. If the exit pressure is less than the back pressure, a normal shock occurs in the diverging section. The sign on the discriminant is changed at a certain location in the nozzle, which yields an exit pressure equal to the back pressure. The location is determined by an iterative technique. If the geometry is unknown, this method would require many iterations before the balance between the flow characteristics and the nozzle geometry is achieved.

Once the fluid velocity is known, the particle velocity can be found using the following formula, Butters (1981):

$$U_d = U_c\left(1 - 0{,}008 D_d^{\,0.3} \rho_d^{0.5}\right) \qquad [1.18]$$

where D_d = the particle diameter in mm,

ρ_d = the particle density, kg/m^3.

From the above formula, a 1 mm diameter particle would obtain 50% of gas velocity, whereas a 0,01 mm diameter particle would have almost 90% of gas velocity provided there is enough time for momentum coupling between the phases.

Crowe (1998) suggested that the particle velocity continues to increase after they leave the nozzle as shown in Figure 1.12. As the air velocity accelerates, the particle velocity increases due to the increased drag force. The highest air velocity is achieved at the exit of the nozzle provided the geometry of the nozzle is correct. As the air velocity decreases after leaving the nozzle, the particle velocity continues to increase and at certain distance from the nozzle the velocities become equal. After that the particle velocity remains higher than the air velocity due to inertia of the particles.

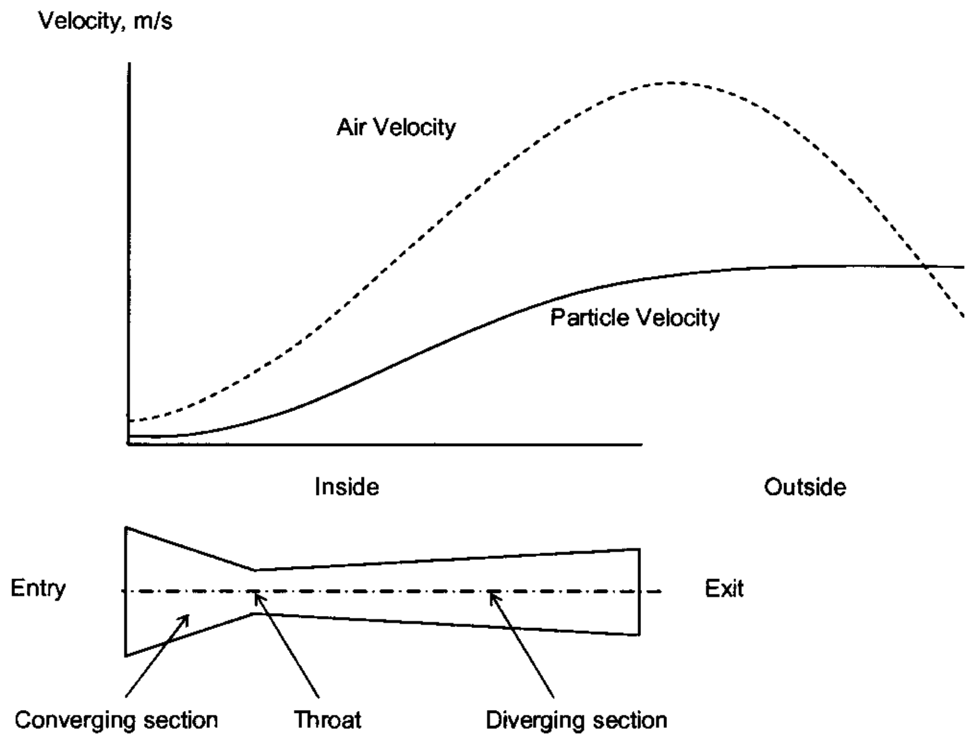

Figure 1.12. Air and particle velocities inside and outside a nozzle, Crowe (1998)

1.3 Nozzle Material

1.3.1 Wear

The wear resistance is the main property of blasting nozzles as they are subjected to abrasion by particles. Nozzle toughness is also important from the handling point of view. The other important property of abrasive blasting nozzle is porosity. If a material has high porosity, like cast ceramics, abrasive particles rapidly wear cavities in the material, causing turbulence, reducing velocity and eventually destroying the material.

The blasting nozzle of the thermal gun is also subjected to extreme thermal stresses. The nozzle temperature reaches hundreds degrees of Celsius within seconds. Therefore, the nozzle material must have good all-round mechanical properties. Materials suited for abrasive blasting nozzles are tungsten carbide and ceramics, such as boron carbide, silicon carbide, nitride-bonded silicon carbide and SIALON.

Nozzle wear is an important factor in nozzle design. However, it is not the goal of this project to study wear of thermo-abrasive nozzles. Therefore, there will be only a short description of wear of nozzle materials.

The two major wear mechanisms of brittle materials are fracture due to cracks forming and scratching. A wear resistance parameter for brittle materials was suggested by Evans (1980),

$$P = K^{0,5} E^{-0,8} H^{1,43} \qquad [1.19]$$

Where P = wear resistance parameter,

K = the fracture toughness, MPa m$^{1/2}$,

E = Young's Modulus, MPa,

H = Hardness, MPa.

The critical load for generating cracks in brittle materials is referred to as a "cracking threshold", denoted by P_c, which is measured in Newton. The cracking thresholds for various materials are shown in Table 1.1 [Schwetz, 1995:150].

Table 1.1 Cracking thresholds

Item	Material				
	WC	ZrO_2	β- Si_3N_4	α-Si_3N_4	SiC, Al_20_3, B_4 C
Cracking threshold, P_c, N	10000	1000	100	10	1

Wear of materials under dry sliding conditions depends on a sliding velocity given by $U_d^{7/3}$. For blasting nozzles, the particle velocity is higher in the diverging section of the nozzle, therefore, this section wears quicker than the converging section, which is proven in practice.

Wear of ceramics under dry sliding conditions is, besides mechanical overload, often governed by frictional heating. During the processing of the ceramics, some faults remain at the grain boundaries. These faults may be regarded as initial cracks. Because of their origin their length is related to the grain size, which is small compared to the length of the contact. Metselaar (2002) showed that severe wear is the result of the propagation of these cracks due to frictionally-induced thermal stress. Since materials expand when heated, this localized heating will generate localized strain and therefore, stresses at the surface. At the tip of a pre-existing crack, this stress will reach a maximum value. The failure condition is as follows [Metselaar, 2002:963]:

$$\beta\sqrt{\pi d}\,\sigma_{\max} > K \qquad [1.20]$$

where d = the length of crack, m,

β = constant, which depends on the type of crack,

$\sigma_{\max}$ = the thermal stress, MPa,

K = the fracture toughness, MPa $m^{1/2}$.

In the analysis of brittle materials, the probability of failure is commonly modelled using the Weibull weakest link. This is based on the concept of a chain, which when one link fails, the total chain fails. The Weibull parameter is a measure of the scatter in the failure strengths of nominally identical specimens. The probability of failure by Weibull is as follows, Weibull (1939):

$$P_f = 1 - \exp\left\{-\left(\frac{\sigma}{\sigma_0}\right)^{m_w}\left(\frac{A}{a}\right)\right\} \qquad [1.21]$$

where P_f = the probability of failure,

A = the surface area, m^2,

a = the unit area, m^2,

m_w = the Weibull modulus,

σ = the maximum stress, MPa,

σ_0 = the minimum failure stress, MPa.

Wear of nozzle materials also depends on abrasive media. The characteristics of some abrasive media is given in Table 1.2 [Schwetz,1995:152]. The most abrasive blasting media used in abrasive blasting is α-Al_2O_3.

Table 1.2 Physical properties of some erodent abrasives

Material	Composition	Density ($g\ cm^{-3}$)	Moh's Hardness number	Grit number (mesh)	Mean grain size, (μm)
Olivine	$(Mg, Fe)_2SiO_4$	3,3	6,5	90	180-1250
Garnet	$Fe_3Al_2(SiO_4)_3$	4,1	7,5	80	200
Alumina	α-Al_2O_3	3,9	9,0	100	120

1.3.2 Thermal Stresses

Thermal stresses are developed because of phase transformation, differential expansion, anisotropic expansion within crystals and temperature gradients and their effects on dimensional changes. In the case of non-uniform dimensional changes, the changes lead to differential strain and finally to failure within the material. The thermal stresses are encountered in surface treatment techniques such as plasma spraying, physical vapour deposition and chemical vapour deposition.

During thermal shock, when the change in temperature exceeds a critical temperature difference of the material, the tensile stress generated in the material due to temperature gradient exceeds its actual tensile strength, resulting in failure of the material. The basic formula for the thermal stress is as follows:

$$\sigma = \frac{E\alpha\Delta T}{1-\nu} \qquad [1.22]$$

where: σ = the thermal stress, MPa,

E = the Young's modulus, GPa,

α = the coefficient of thermal expansion, $1/^{0}C$.

ΔT = the temperature gradient, K,

ν = Poisson 's ratio.

The temperature difference or gradient, ΔT, which causes the failure of a material is known as the critical temperature difference. The temperature difference depends on thermal and mechanical properties of materials, thickness of the specimen and other conditions. Ultimately, the respective thermal expansion coefficients and mechanical properties are the most important factors determining the thermal stress sign and magnitude. The evaluation of thermal stresses is complicated by the fact that the material properties in equation [1.22] change their values with a temperature change.

Some conventional blasting nozzles are made of ceramic materials. Therefore, there was a need to investigate the ability of ceramics to withstand thermal shocks. There are many test methods available to characterise thermal shock and thermal fatigue of ceramic materials. They are mostly quench experiments, which are descending in nature. It appears that in quenching loading, the thinner the specimen the lower the thermal stress, [Panda, 2002:2195], whereas for ascending loading a thicker ceramic can withstand a greater temperature difference. Kesler (1998) obtained similar results when testing different thickness of coating layers of ceramics in plasma spraying. The thinner the layer of ceramic the higher the thermal stress the specimen could withstand [Kesler, 1998:219].

Kamiya (2001) studied thermal stress fractures of the ceramic filters due to char combustion in collected ash layers of power plants. Ceramic filters have the shape of hollow cylinders, which is similar to nozzles. Kamiya (2001) used a modified formula for the calculation of thermal stresses of a cylindrical filter. The maximum tensile thermal stress on the outside surface of the cylindrical ceramic filter is calculated using the following equation [Kamiya, 2001:143]:

$$\sigma = \frac{E\alpha\Delta T}{1-\nu}\left[\frac{1}{2\ln\left(\frac{b}{a}\right)} - \frac{1}{\left\{\left(\frac{b}{a}\right)^2 - 1\right\}}\right] \qquad [1.23]$$

where b = the outer diameter of the cylinder,

a = the inner diameter of the cylinder.

Criteria defining the resistance to crack initiation and crack propagation were first proposed by Kingery (1955). The shock resistance criteria R_1 and R_2 are for severe thermal shocks and mild thermal shocks respectively. The severe thermal shock criterion R_1 corresponds to the maximum allowable temperature difference in a body under conditions of steady-heat flow. The mild thermal shock criterion R_2 corresponds to the maximum allowable heat flux through a body, Kingery (1955).

$$R_1 = \frac{\sigma(1-\nu)}{E\alpha} \qquad [1.24]$$

$$R_2 = k \cdot \frac{\sigma(1-\nu)}{E\alpha} = kR_1 \qquad [1.25]$$

where σ = the stress, MPa,

E = Young's Modulus, MPa,

ν = Poisson's ratio,

α = the thermal expansion coefficient, 10^{-6}/°C,

k = the thermal conductivity, W/m °C.

Several fracture initiation criteria have been proposed, depending on the shapes of the structure (e.g. cylinder, plate or sphere) and the types of loading (e.g., heat flow, prescribed surface temperature, heat transfer by convection, steady state or transient heating or cooling conditions). Glandus (1981) suggested the use of the following criterion for determining a type of thermal shock:

$$\beta = \frac{b \cdot h}{k} \qquad [1.26]$$

where b = the material thickness, m,

h = the convection coefficient, W/·m^2 °C,

k = the thermal conductivity, W/m °C.

If the value of $\beta > 40$ a thermal shock is regarded as severe, if $\beta < 1$ it corresponds to a mild thermal shock.

Schmitt (2002) studied the thermal shock resistance from a micromechanical point of view and applied classical fracture initiation criteria, which was adapted to the case of heterogeneous materials by using:

- a homogenization method,
- computation of local stress state through stress concentration factors.

Schmitt (2002) stated that micromechanics can be a tool to optimize heterogeneous materials against thermal shocks, i.e., the composition of the material can be tailored to respect the macroscopic thermal shock for a given set of failure mechanisms.

Panda (2002) studied the effects of thermal conductivity and cooling of surfaces of ceramic samples. He concluded that the thermal conductivity of the interface does not affect the maximum thermal stress significantly but it changes the temperature distribution in the sample. According to Panda (2002) thermal stress is mainly influenced by the temperature distribution on a surface, which is exposed to heat flow and was not affected by the temperature distribution at the opposite surface. Therefore, measurement of temperature of the outer surface is not very critical for thermal stress calculation [Panda, 2002:332].

There are several commonly used methods of stress determination: mathematical modelling (analytical or numerical), material removal techniques (hole drilling, layer removal), mechanical methods (curvature, displacement, or strain measurement) and diffraction (X-ray or neutron) methods. Each technique has certain advantages and limitations; their applicability is determined by such factors as shape, dimensions, materials and processing conditions.

Some of the advantages of neutron diffraction include its non-destructive nature, ability to determine stress in each individual phase of a composite, and applicability to specimens of various sizes and shapes. X-ray diffraction can determine stress only in a thin surface layer, whereas the penetrating power of neutrons enables through-thickness stress profiling without any material removal.

The curvature method allows determination of stresses in thick layers of graded or inhomogeneous composition, and is a non-destructive method. This method has a narrower spatial resolution than the neutron diffraction technique, and thus allows more detailed through-thickness stress profiling of deposited layers. However, unlike the neutron diffraction technique, the curvature method can be used on only simple geometries of specimens.

Material removal techniques, mechanical methods and diffraction methods could not be used in these studies because of the process conditions and limitations. These include: high temperature, hardness of specimens, no possibility to place a working system inside of measuring equipment, etc. It was concluded, therefore, that the analytical and numerical method would be more suitable and applicable to evaluating the stress conditions of thermal jet nozzles, i.e. for the purpose of this research.

One of the most widely known analytical methodologies for determining the stress in places where the measurement can not be done is the Green's function technique (GFT), [Botto, 2003:23]. According to the GFT the response at any point of a linear system due to an external input can be evaluated by means of its response (Green's function) to the corresponding unit input, whatever the input may be (load, temperature, etc.). The principle of the method is that temperatures at the boundaries of the model are measured (on-line) and then evaluated (off-line).

In the thermal-abrasive gun, the temperature of the flow inside of the combustion chamber is in a region of 2 000 K. Theoretically, a thermocouple can be inserted into the combustion chamber. But practically it would be very difficult to achieve due to the small size of the thermal gun and many design constraints. For example, any object in the flow would create extra disturbances, and therefore, would interfere with the results. In addition the abrasives can destroy a thermocouple inside the chamber. More importantly the thermocouple can not be placed inside the blasting nozzle, where the flow temperatures must be obtained.

Finite element numerical analyses of thermal stresses have been successfully used in a number of studies of plasma spraying and coating of ceramic materials. Ucar (2001) applied the general purpose finite element code ANSYS obtaining a transient thermal/structured coupled solution for various ceramic coatings. The main conclusions were that the thermal stresses depend on purity of the coating and mechanical mismatch due to a different thermal expansion coefficient. Kocabicak (1999) also used the ANSYS code to study the transient thermal stresses in coating systems and found that the finite element technique can be used to optimise the design and the processing of ceramic coatings.

Traditionally sandblasting nozzles are mainly made of different grades of tungsten carbide. This is due to high wear resistance and mechanical properties of tungsten carbide. The main drawback of tungsten carbide is the cost of material and its weight. The erosion mechanism of WC nozzles appears to be a preferential removal of the cobalt binder followed by pluck out of the undermined WC grains [Schwetz,1995:153].

With the advances of ceramic materials, attempts were made to replace tungsten carbide with various types of ceramics, such as boron carbide and silicon carbide. Silicon carbide nozzles have up to 50% longer service life than tungsten carbide nozzles, especially when blasting media is α-Al_2O_3. However, when a blasting media is steel shot the difference is only 20%. This is according to an American company called Boride (Engineered Products Group of Greenfield Industries), which produces blasting nozzles. The other advantages of silicon carbide nozzles are low weight and low cost compared with tungsten carbide. However, they did not find wide applications in industry mainly because of their brittleness.

Boron carbide nozzles showed the highest wear resistant properties. According to Boride (Engineered Products Group of Greenfield Industries), the service life of boron carbide nozzles is at least 10 times longer than that of tungsten carbide nozzles. Again, they are not commonly used in industry mainly because of their brittleness. In order to protect boron nozzles from the mechanical shock they are covered with polyurethane. This obviously cannot be used for thermo-abrasive blasting due to the heat.

One of the latest ceramic materials used for abrasive blasting nozzles is SIALON, which possesses excellent mechanical characteristics compared to the above mentioned ceramics. For example, the tensile strength of SIALON 050 according to company KRIMETAL is 450 MPa, and the fracture toughness 7,7 MPa $m^{1/2}$. SIALON is also lighter than other materials. However, it appears that the course media creates microcracks in ceramic causing quick wear of nozzles. This was observed by Shigietaka (1993), who studied cutting of SIALON by means of water-jet cutting. When an angle of impact was close to 90^0 the fracture wear mechanism was dominating [Shigietaka, 1993:1267]. Schwetz (1995) reported similar results on brittle fracture of boron carbide nozzles.

Some rocket nozzles are made of metal/ceramic functionally graded materials, where proprietary ceramic coatings protect nozzle base materials from high temperatures.

The manufacture of a nozzle for thermo-abrasive blasting from metal/ceramic functionally graded materials is not feasible due to the length and small diameter of the nozzle bore, which would not allow a coating of ceramic inside the nozzle. The other point is that the coating layer would be worn out by the abrasive in a short period of time.

Since HVAF and HVOF systems were introduced in coating processes there was a need for nozzles, which could withstand high temperatures. There were some developments in nozzle design for thermal spraying. However, references to applications of ceramic nozzles were found mainly in patents.

According to Browning (1983), a nozzle or nozzle insert can be constructed by machining a graphite tube, and then coating the graphite tube with silicon carbide, which is a ceramic material having thermal expansion properties similar to graphite. A nozzle presented in US Patent 4384434 has a length up to 14 inches, an outside diameter of 1 inch and a straight bore of one-half inch. According to Browning (1983), the silicon carbide coating was applied by a process initially patented by Texas Instruments Incorporated, and sold under a trade name of T.I. Coat, and also referenced under a trade name of M.T.C. Dura-Cote Silicon Carbide. The silicon carbide coating includes thicknesses greater than five-thousandths of an inch with zero porosity. Browning (1983) reported good results with regard to quality and speed of spraying.

White (1996) reported on the nozzle inserts made of a solid Carborundum Hexalloy.RTM. material, which is a dense silicon carbide. Two nozzles were utilized, one, which has a central bore internal diameter of one-half inch. The other has a central bore internal diameter of seven-sixteenths inch. According to White (1996) tests with thermal spray guns yielded high deposition efficiencies and superior coating qualities. However, no data on the thermal stress or particle velocity was provided. White (1996) further stated that care must still be taken not to subject ceramic inserts and liners to thermal shock, and thus fracture, by heating up or cooling them down to quickly. Thermal shock of ceramic components is avoided in White's invention by starting-up combustion of the thermal gun at a combustion rate, which is slower than the operating combustion rate, thus preheating such ceramic components.

Also during shut-down, a slow combustion rate can again be utilized to slow down the rate at which ceramic components are cooled. In real working conditions this would be difficult to achieve.

The conditions of nozzles in thermal spraying and thermal abrasive blasting differ. The nozzle in thermal spraying needs to maintain a certain temperature in order to prevent solidification of molten particles. According to White (1996) the minimum nozzle temperature should be maintained at 600^0C. Radiant heat transfer is thought to be the primary mechanism for transferring the heat from a nozzle to particles. However, heat is also transferred to particles from high temperature pressurized gas. The uniformity of heat transfer is important in coating processes.

1.4 Conclusions from Literature Search

1.4.1 Thermal Abrasive Gun Design and Modelling

The thermal guns built for thermal spallation were the predecessors of modern thermal spray guns and new abrasive blasting guns. These thermal guns used heat induced on the rock surface to cause thermal shocks that cracked the rocks.

No complete analytical or computational models of thermo-abrasive blasting systems could be found in the literature. Some Russian scientists studied various aspects of the combustion process of HVAF systems, ignition and particle accelerations.

Very little scientific data is available on the design of thermo-abrasive systems, but some technical information has been obtained from patents. Thermo-abrasive blasting systems fall under HVAF systems. HVAF systems are less common than HVOF, which are used for thermal spraying. A number of studies have been done on analytical, numerical and computational modelling of the HVOF processes and systems. However, there are significant differences between HVOF and HVAF systems, which do not allow the application of modelling of HVOF systems to HVAF systems and more specifically abrasive blasting.

The differences are:

1. HVOF systems essentially have a small burner with an attached nozzle. Whereas HVAF systems are built on the principles of a gas turbine and a ram jet with regenerating cooling systems.

2. HVOF systems run on highly flammable gases and oxygen. HVAF systems run on any hydrocarbon fuel and air. There are different chemical reactions and therefore, different conditions.

3. The HVOF system has a low flow rate compared to an abrasive blasting system, which must produce a much higher kinetic energy jet in order to accelerate a larger mass of particles per unit time. The typical nozzle throat diameter of a thermal spray gun is less than 10 mm. The thermo-abrasive blasting nozzle throat diameter is 14 mm to 17 mm.

4. The HVOF system runs at higher temperatures in order to melt spraying materials. Therefore, it requires water cooling. HVAF systems must have an efficient air cooling system and this fact significantly changes the design of a thermal gun.

5. The high velocity nozzle of the HVOF system is made of copper and it is cooled by water. The nozzle does not have to be long since coating particles are smaller and accelerate faster. The nozzle of a thermal abrasive gun has to withstand severe thermal shocks, wear and be of sufficient length for the acceleration of much heavier and larger particles.

1.4.2 Nozzle Geometry and Material

Typical nozzle designs for abrasive blasting are of a Laval type with long converging and diverging sections. This is done for the sake of lower turbulence and in order to increase particle velocity. It is believed that the diverging section of a blasting nozzle has to be 150 – 200 mm long in order to achieve particle velocities of the order of 200 m/s for 0,5 mm particle size.

The thermo-abrasive blasting nozzles are subjected to high temperatures and they have to be designed accordingly. The goal is to achieve the maximum possible productivity of blasting using the simplest nozzle geometry to make the process economically viable.

The geometry of nozzles for thermal spaying cannot be considered for abrasive blasting because they are designed for comparably smaller size and weight particles and much smaller flow rates. Although some patents have the examples of ceramic thermal spraying nozzles, in practice copper nozzles are typically used.

Abrasive blasting nozzle materials are WC and ceramics. The WC has good all-round properties, but is expensive and heavy. Ceramic blasting nozzles are less common, but with advances in material science, there is an increase in ceramic applications for abrasive blasting.

1.4.3 Thermal Stress Analysis

Many studies have been done on thermal stresses and thermal shocks in ceramic materials used as coatings. However, no examples of thermal stress evaluation of the nozzles of high velocity flame systems could be found in the literature.

None of the methods of thermal stress measurements can be directly applied to thermo abrasive nozzles because of the different constraints, such as: extremely high temperatures, rapid temperature rise, inaccessibility of space for measurements of flow parameters, a risk of disintegration of the nozzle due to fracture etc.

Since no direct measurements are possible, the computational modelling is the approach for obtaining thermal stresses in nozzle materials. CFD software can produce a temperature distribution in the flow and in the nozzle wall using a conjugate heat transfer analysis. However, no stress analysis is done by CFD software. The information from the CFD analysis is to be transferred to FEA software for stress evaluation. A CFD analysis can be of a steady-state type because a heat transient analysis is to be done in FEA.

The rate of cleaning would be the best method to evaluate the effectiveness of nozzle geometry. While running trials on a speed of blasting, the nozzles can also be tested for thermal shock resistance. The outer temperature of the nozzle will be measured with a thermocouple and a computer program monitoring temperatures at certain time intervals.

2. PURPOSE OF THE STUDY

The biggest drawback of thermo-abrasive blasting is the short life of blasting nozzles due to extreme conditions combining heat, abrasive wear and mechanical stress. Therefore, there was a need to simulate the working conditions in order to obtain temperatures and stresses in the nozzle.

The nozzle conditions are determined by the flow characteristics, which in their turn depend on the thermal gun design and parameters. Therefore, a model of a thermal gun is required for modelling of the nozzle conditions.

The literature search results showed that there is no HVAF model of the thermo-abrasive gun or a thermo-abrasive blasting nozzle. Some studies in the field of HVOF are related to thermo-abrasive blasting or HVAF systems.

Oberkampf (1996) modelled the internal and external flow in a sonic nozzle in the HVOF process. Mostaghimi (2003) incorporated the previously developed models for thermal spraying into one model. However, there are significant differences between high velocity thermal spraying and thermo-abrasive blasting, which does not allow to apply the previously developed models to thermo-abrasive blasting.

In order to perform a stress analysis, a temperature distribution in the nozzle structure must be obtained. Due to the geometric and other constrains, this can only be done by means of modelling of the flow and the nozzle. A computational fluid dynamics analysis can provide a temperature distribution in the nozzle, which can, then, be used in a finite element analysis for stress evaluation.

The specific aims of the study can be summarised as follows:

1. To analyse the combustion and particle flow processes inside the combustion chamber and the nozzle of a thermal gun in order to optimise the design of the combustion chamber and the nozzle;
2. To develop computational fluid dynamics (CFD) models for simulations and evaluations of the combustion and thermo-abrasive blasting processes in order to obtain the

temperature distribution in the thermal gun and the nozzles of different types and geometries;

3. To apply the CFD data in a finite element analysis (FEA) to calculate/model thermal stresses in nozzles for the typical operating conditions of the thermal gun;
4. To determine the most suitable nozzle materials and to determine to what degree an improved overall nozzle geometry can contribute to a reduction in nozzle failures and
5. To optimise efficiency of thermo-abrasive blasting as a result of the improvement of the thermal gun design, the nozzle geometry and material.

The methodology followed in this study was as follows (Fig. 2.1):

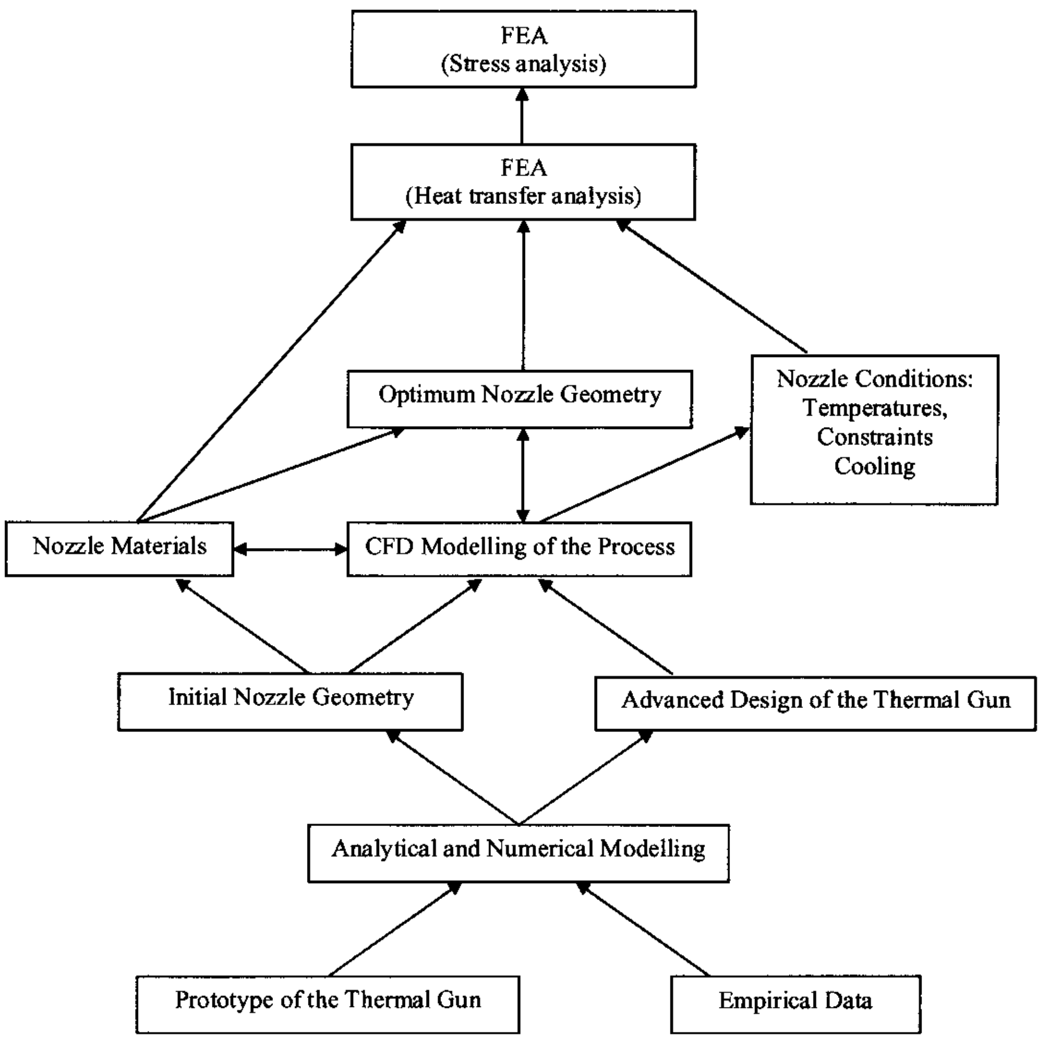

Figure 2.1. Methodology of the study

The procedure of the study was as follows:

- Analytical and numerical modelling of the process inside the thermal gun
- Design, manufacture and testing of the thermal gun
- CFD modelling of the process inside the thermal gun and nozzles
- Finite Element Analysis of the nozzle materials
- Design, manufacture and testing of the thermo jet blasting nozzles
- Comparison of the modelling with experimental results
- Conclusions

3. ANALYTICAL MODELLING OF THE THERMAL GUN

3.1 Theoretical Principles

3.1.1 Gas Cycle

The thermal gun comprises elements of a gas turbine and a ramjet. The main features of the thermo-abrasive gun are a combustion chamber and a nozzle. A thermodynamic cycle of a thermal gun is derived from an air-standard Brayton cycle (Fig. 3.1) and includes only two stages (2 - 3 and 3 - 4), i.e. combustion and expansion stages. Referring to Fig. 3.2, compressed air is supplied to the thermal gun by an external source, i.e. an air compressor (stage 1 - 2). Combustion of fuel takes place inside the combustion chamber of the thermal gun (stage 2 – 3). In the thermal gun, the expansion of gases takes place in a converging-diverging nozzle (stage 3 – 4).

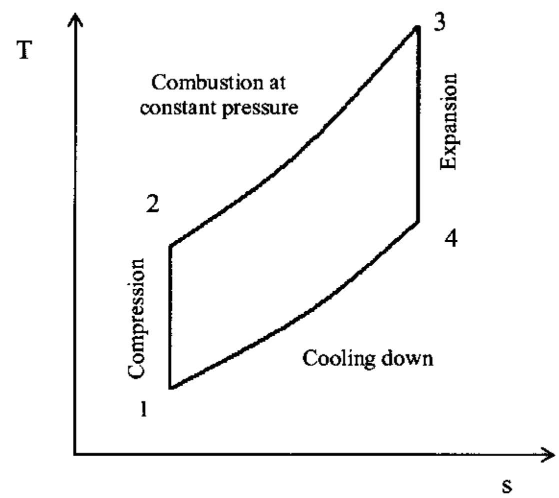

Figure 3.1. *T-s* diagram of an air-standard ideal Brayton cycle

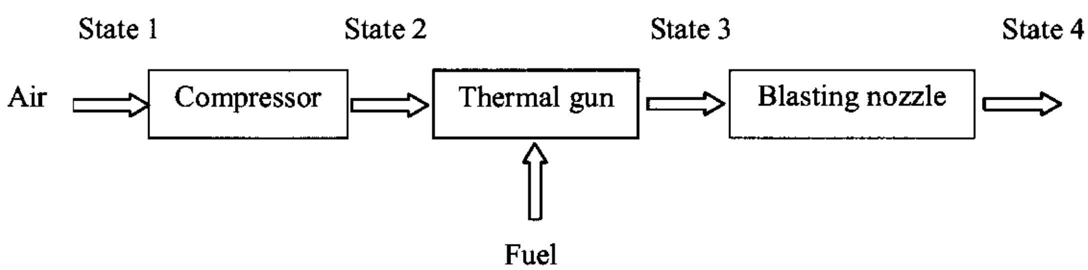

Figure 3.2. Elements and stages of a thermal gun system

The ideal Brayton cycle is applicable to the thermal gun with the following assumptions:

- Compression and expansion are reversible and adiabatic, i.e. isentropic.
- The change of kinetic energy of the working fluid between inlet and outlet of each component is negligible.
- There are no pressure losses in the components of the system.
- The working fluid is a perfect gas with constant heats.
- The mass flow is constant through the cycle.
- Heat transfer is 'complete', i.e. heat gained is equal to heat loss.

The relevant steady flow of energy equation is [Cohen, 1996:38]:

$$Q = (h_2 - h_1) + \frac{1}{2}(U_2^2 - U_1^2) + W \qquad [3.1]$$

where Q and W are the heat and work transfers per unit mass flow,

h = the specific enthalpy, kJ/kg K,

U = the velocity, m/s.

Applying this to the two stages of the thermal gun system, combustion and expansion we get

$$Q_{23} = (h_3 - h_2) = c_p(T_3 - T_2) \qquad [3.2]$$

$$W_{34} = (h_3 - h_4) = c_p(T_3 - T_4) \qquad [3.3]$$

where c_p = the specific heat at constant pressure, kJ/kg K,

T = the absolute temperature, K,

The subscripts correspond to the gas cycle stages.

According to Cohen (1996) the efficiency of the ideal gas turbine cycle is determined as follows:

$$\eta = \frac{\text{net work output}}{\text{heat supplied}} = \frac{c_p(T_3 - T_4) - c_p(T_2 - T_1)}{c_p(T_3 - T_2)} \qquad [3.4]$$

The efficiency of the thermal gun can be expressed without the second term of the numerator because the compression is taking place inside the compressor. Then

$$\eta = \frac{\text{heat released}}{\text{heat supplied}} = \frac{c_p(T_3 - T_4)}{c_p(T_3 - T_2)} \qquad [3.5]$$

The above formula can be expressed in other terms. In thermodynamics, the properties of a gas are described by enthalpy and specific heats. The ratio of the specific heat at constant pressure c_p to the specific heat at constant volume c_v of ideal gas is

$$\gamma = \frac{c_p}{c_v} \qquad [3.6]$$

Taking into account the isentropic *p-T* relation, the pressure ratio between states 3 and 4 (entry-exit of nozzle) is expressed as

$$r = p_3 / p_4 \qquad [3.7]$$

where r = the pressure ratio,

p_3 = the pressure inside the combustion chamber,

p_4 = the pressure at the exit of the nozzle.

The relationship between the pressure, specific heats and temperatures is as follows [Cohen, 1996:39]:

$$r^{\frac{(\gamma-1)}{\gamma}} = \frac{T_3}{T_4} \qquad [3.8]$$

Then, the efficiency of the thermal gun can be expressed in terms of the pressure ratio and the ratio of specific heats as follows:

$$\eta = 1 - \left(\frac{1}{r}\right)^{\frac{(\gamma-1)}{\gamma}} \qquad [3.9]$$

It can be seen that the efficiency of an ideal Brayton cycle and hence the thermal gun depends only on the pressure ratio and the nature of the gas, i.e. on the efficiency of the combustion process. The higher the pressure ratio and ratio of specific heats, the higher the efficiency.

The combustion temperature rise ΔT depends on the fuel/air ratio and gas properties. For common hydrocarbon fuels, these values have been determined and are given in standard fuel combustion tables. However, the combustion efficiency is difficult to measure accurately. In practice it is assumed that combustion is nearly complete.

For the thermal gun, the efficiency can be expressed as a ratio of kinetic energy of the jet to the rate of energy supplied in the fuel [Cohen, 1996:89].

$$\eta = \frac{m(U_4^2 - U_3^2)/2}{m_f Q_{net,p}} \quad [3.10]$$

where m = the mass flow rate, kg/s,

$Q_{net,p}$ = the fuel net calorific value at constant pressure, kJ/kg,

m_f = the fuel consumption, kg/s.

The fuel net calorific value at constant pressure $Q_{net,p}$ is equal in magnitude but opposite in sign to the enthalpy of combustion reaction and can be taken from tables for common fuel compositions. For hydrocarbon fuel, containing 13,92% H and 86,08% C, the net calorific value is $Q_{net,p}$ = 43 100 kJ/kg [Cohen, 1996:59].

Once the fuel/air f ratio is known, the fuel consumption can be calculated as

$$m_f = f \cdot m \quad [3.11]$$

3.1.2 Governing Equations

The conservation laws for two consecutive stages of the gas cycle are as follows:

Conservation of mass: $m = \rho_1 A_1 U_1 = \rho_2 A_2 U_2$ [3.12]

Conservation of momentum: $c_p(T_2 - T_1) + \frac{1}{2}(U_2^2 - U_1^2) = 0$ [3.13]

Conservation of energy: $c_p(T_2 - T_1) = 0$ [3.14]

Stagnation pressure and temperature are the properties of the gas that are used with static values to determine the combined thermodynamic and mechanical state of the stream. The relationship between the stagnation pressure and the pressure of the moving stream is as follows [Cohen, 1996:93]:

$$\frac{p_0}{p} = \left(1 + \frac{\gamma - 1}{2} M^2\right)^{\frac{\gamma}{\gamma-1}} \qquad [3.15]$$

where M = Mach number.

The formula for the flow velocity in the nozzles is as follows:

$$U = \left[\frac{2\gamma}{\gamma - 1} R T_0 \left\{1 - \left(\frac{p}{p_0}\right)^{\frac{(\gamma-1)}{\gamma}}\right\}\right]^{\frac{1}{2}} \qquad [3.16]$$

where R = the gas constant, J/kg K.

The flow velocity depends also on the geometry of a nozzle. From a designing point of view, it is important to use an expression relating the area A of a nozzle at a given section of a nozzle to the area A^* that would be required for sonic flow (M = 1) at the nozzle throat.

These areas are related as follows [Moran, 1998:431]:

$$m = \rho_1 \cdot A_1 \cdot U_1 = \rho^* \cdot A^* \cdot U^* \qquad [3.17]$$

and

$$\frac{A}{A^*} = \frac{1}{M}\frac{p^*}{p}\left(\frac{T}{T^*}\right)^{\frac{1}{2}} \qquad [3.18]$$

where ρ^*, U^*, p^* and T^* are the gas parameters when M =1.

The relationship between nozzle diameter ratio, velocity and Mach number is [Moran, 1998:431]:

$$\frac{A}{A^*} = \frac{1}{M}\left[\left(\frac{2}{\gamma+1}\right)\left(1+\frac{\gamma-1}{2}M^2\right)\right]^{\frac{(\gamma+1)}{2(\gamma-1)}} \qquad [3.19]$$

where A^* = the area when $M = 1$ at stagnation conditions, m^2,

A = the nozzle area at a given section along the nozzle axis, m^3.

For a given value of A/A^* there are two values for the Mach number, one subsonic and one supersonic. The variations of A/A^* with M is given in the references [Moran, 1998:431]. From the above it can be seen that to accelerate a fluid subsonically, a convergent nozzle must be used, but once $M = 1$ is achieved, further acceleration to $M > 1$ can occur only in a divergent nozzle. Therefore, a converging-diverging nozzle is required. Furthermore, the Mach number of unity, $M = 1$, can only occur at the location of a nozzle where the cross-sectional area is a minimum, i.e. in the throat.

The back pressure, i.e. the atmospheric pressure, must be taken into account in the nozzle calculations because it influences nozzle geometry. Decreases in back pressure result in shock waves occurring inside of the diverging section of the nozzle. For example, the supersonic jet Concorde has variable throat and exit diameters.

3.2 Analytical Modelling of the Thermal Gun

Multiphase approach in these calculations is aimed at achieving gas flow characteristics. The analytical modelling does not include full coupling of dilute and discrete phases because this is modelled in the CFD analysis. Since the combustion gas flow is predominant in the thermal gun it is assumed that particles do not significantly influence the temperature of the flow. The Lagrangian approach with phase coupling for particle velocities is applied in the CFD modelling.

The air flow from the compressor is divided into two flow streams. One stream flows directly to the combustion chamber (Fig. 3.3). The other stream carries the abrasives to the delivery nozzle. The two streams meet in the combustion chamber before entering the blasting nozzle. Therefore, the multiphase flow in the thermo-abrasive gun consists of a cold air/abrasive flow and combustion gases.

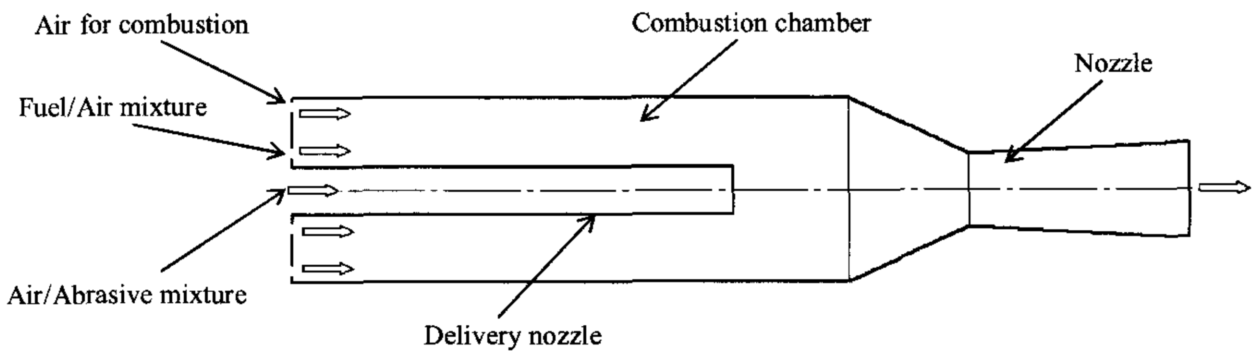

Figure 3.3. Diagram of the HVAF system

3.2.1 Air/Abrasive Flow

In order to calculate gas and particle exit velocities, as well as the effective nozzle geometry, relevant physical properties of the mixture of streams need to be determined. The procedure for calculating multiphase flows was described by Crowe (1998).

The total mass flow rate includes the mass flow rate for the combustion stream and the mass flow rate for the abrasive stream.

$$m_{total} = m_{comb} + m_{airp} \qquad [3.20]$$

where m_{comb} = the mass flow rate of air directed to combustion, kg/s,

m_{airp} = the mass flow rate of air directed to propel particles, kg/s.

The air/abrasive stream is a two-phase flow consisting of a continuous phase and dispersed phase. The mass flow rate of air, which propels abrasives must include the loading of particles and is determined as follows:

$$m_{abr} = m_{airp}(1+z) \qquad [3.21]$$

where z = the total loading.

$$z = \frac{M_d}{M_c} \qquad [3.22]$$

where M_d = the mass flow rate of dispersed phase, kg/s,

M_c = the mass flow rate of continuous phase, kg/s.

The volume fraction of air and abrasives can be obtained from the above mass flow rates. The density of the mixture can be calculated as:

$$\rho_{mix} = \alpha_{air}\rho_{air}(1+z) \qquad [3.23]$$

where: α_{air} = the volume fraction of air,

ρ_{air} = the density of air, kg/m^3.

The calculation of variables of a multiphase flow depends on whether the flow is dilute or dense, which can be determined using the ratio of the distance between the particles to the particle average diameter given as

$$\frac{l}{D_d} = \sqrt[3]{\frac{\pi}{6} \cdot \frac{1+\alpha_{abr}}{\alpha_{abr}}} \qquad [3.24]$$

where l = the distance between particles, m,

D_d = the particle diameter, m,

α_{abr} = the volume fraction of abrasives.

If the ratio l/D_d is greater than 10 the flow is considered dispersed and individual particles could be treated as isolated particles with little influence of the neighbouring elements on the drag or heat transfer rate.

The characteristics of the air/abrasive mixture need to be calculated for further calculations of the nozzle geometry. The specific heat of the air/abrasive mixture is as follows:

$$c_{p_m} = c_{p_{air}} \left(\frac{1 + z \cdot c_{p_d} / c_{p_{air}}}{1+z} \right) \qquad [3.25]$$

where $c_{p_{air}}$ = the specific heat of air, J/kg K,

c_{p_d} = the specific heat of Al_20_3, J/kg K.

The gas constant of the air/abrasive mixture is

$$R_{cold} = \frac{c_{p_m}(\gamma - 1)}{\gamma} \qquad [3.26]$$

3.2.2 Mixing of the Air/Abrasive and the Combustion Flows

Abrasives are carried by the compressed air through the delivery nozzle into the combustion chamber where they mix with the combustion gases. The air/abrasive two-phase flow is regarded as a cold stream. The mixing of the hot and cold flows takes place inside the combustion chamber as shown in Figure 3.4.

The parameters of the air/abrasive cold stream are denoted as: m_{cold} ,T_{cold} , p_{cold}, D_{cold}. The parameters of the hot stream are denoted as: m_{hot} , T_{hot}, p_{hot}, D_{hot}. The parameters of the mixed stream at the entry of the nozzle are denoted with index 3, which corresponds with the gas cycle state (Fig. 3.2): m_3, T_3 , p_3 , D_3.

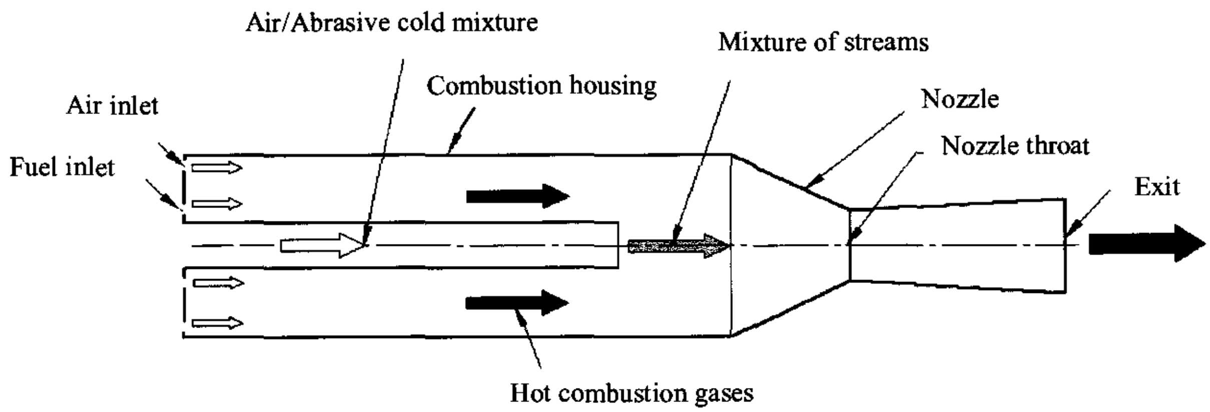

Figure 3.4. Diagram of the mixing of the streams

The momentum equation must balance to satisfy the conservation of momentum as follows (Fig. 3.4):

$$(m_{cold} \cdot U_{cold} + p_{cold} \cdot A_{cold}) + (m_{hot} \cdot U_{hot} + p_{hot} \cdot A_{hot}) = m_3 \cdot U_3 + p_3 \cdot A_3 \qquad [3.27]$$

Assuming that the flow is isentropic at the end of the combustion chamber and the static pressure is uniform across the combustion chamber, i.e. $p_{hot} = p_{cold}$. Then, equation [3.29] can be solved by means of iterations assuming a Mach number in the combustion chamber.

The pressure ratio is then calculated using equation [3.15]. From equation [3.15], the stagnation pressure is:

$$p_{hot} = \frac{p_0}{\left(1 + \frac{\gamma - 1}{2} M^2\right)^{\frac{\gamma}{\gamma - 1}}} \qquad [3.28]$$

The temperature ratio for the hot stream is calculated using [Moran, 1998:431]:

$$\frac{T_0}{T_{hot}} = \left[1 + \left(\frac{\gamma - 1}{2}\right) M^2\right] \qquad [3.29]$$

The stagnation temperature is then

$$T_{hot} = \frac{T_0}{\left[1 + \left(\frac{\gamma - 1}{2}\right) M^2\right]} \qquad [3.30]$$

The stagnation velocity of the hot stream can be calculated from the conservation of mass.

$$U_{hot} = \frac{m_{hot} \cdot R_{gas} \cdot T_{hot}}{p_{hot} \cdot A_{hot}} \qquad [3.31]$$

The stagnation velocity of the cold stream (air/abrasives) from the conservation of mass is

$$U_{cold} = \frac{m_{cold} \cdot R_{cold} \cdot T_{cold}}{p_{cold} \cdot A_{cold}} \qquad [3.32]$$

The values of the mass flow rate, the velocities and the areas are substituted into equation [3.27] and the value of the momentum for incoming streams is obtained.

Now parameters for the right-hand side of equation [3.27] need to be obtained and the equation must be balanced (See page A5 of Appendix A). The temperature of the mixture at state 3 can be found from the balance of enthalpy as follows:

$$h_{hot} - h_{cold} = h_{mix} \qquad [3.33]$$

The mass flow rate of the mixture at the nozzle entry (state 3) using the conservation of mass is

$$m_3 = m_{cold} + m_{hot} \qquad [3.34]$$

A number of iterations are required in order to find the mixture pressure and temperature. This is necessary to balance the momentum equation because there are two unknowns. First the Mach number is guessed. Then, the stagnation temperature of the mixture is found using equation [3.30] from the following ratio:

$$T_3 = \frac{T^0_{mix}}{T_{ratio}} \tag{3.35}$$

In order to determine the stagnation pressure of the mixture the velocity is chosen according to the Mach number. The stagnation pressure is then calculated using

$$p_3 = \frac{m_3 \cdot R_{mix} \cdot T_3}{A_3 \cdot U_3} \tag{3.36}$$

If equation [3.27] is balanced, the parameters m_3, T_3, and p_3 are used as the flow characteristics at the entry to the nozzle (See page A7 of Appendix A).

3.2.3 Nozzle Geometry

The nozzle throat diameter, the entry diameter and exit diameter are calculated using the standard tables for compressible flows in nozzles. If the combustion efficiency coefficient is included in the calculation then the pressure ratio between the states 3 and 4 is determined as follows [Cohen, 1996:403]:

$$\frac{p_{03}}{p_4} = \frac{1}{\left[1 - \frac{1}{\eta}\left(\frac{\gamma-1}{\gamma+1}\right)\right]^{\gamma/(\gamma-1)}} \tag{3.37}$$

where p_{03} = the stagnation pressure in the combustion chamber, MPa,

p_4 = the critical pressure or the pressure at the nozzle throat, MPa.

The critical pressure or the pressure at the nozzle throat is found again from the ratio:

$$p_4 = \frac{p_{03}}{p_{ratio}} \quad [3.38]$$

Since the area of the nozzle throat is unknown it is necessary to calculate the gas temperature, density and velocity at the exit.

$$T_4 = T_{03} \cdot \left(\frac{2}{\gamma + 1} \right) \quad [3.39]$$

The mixture density in the nozzle throat is

$$\rho_4 = \frac{p_4}{RT_4} \quad [3.40]$$

where R = the gas constant of the final mixture, J/kg K.

The gas velocity in the nozzle throat is

$$U_4 = \sqrt{(\gamma R T_4)} \quad [3.41]$$

The throat area per mass flow is determined as [Cohen, 1996:101]

$$A_S = \frac{A_4}{m} = \frac{1}{\rho_4 U_4} \quad [3.42]$$

where $m = m_3$, the total mass flow, kg/s.

The nozzle throat area and diameter are determined using the above equation as follows:

$$A_4 = m A_S \quad [3.43]$$

$$D_4 = \sqrt{\frac{4 A_4}{\pi}} \quad [3.44]$$

The specific thrust is [Cohen, 1996:87]:

$$F_s = (U_4 - U_3) + \frac{A_4}{m}(p_4 - p_3) \qquad [3.45]$$

The full thrust is:

$$F = mF_S \qquad [3.46]$$

The *T-s* diagram of the states within the nozzle is shown in Figure 3.5. From state 3 to state 4 an isentropic expansion takes place. Figure 3.6 shows the Laval nozzle with the entry (state 3) and the exit (state 4) corresponding to the gas cycle.

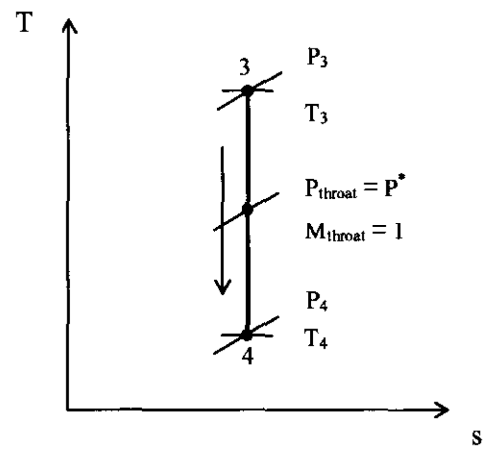

Figure 3.5. *T-s* diagram of expansion in the nozzle, Moran (1998)

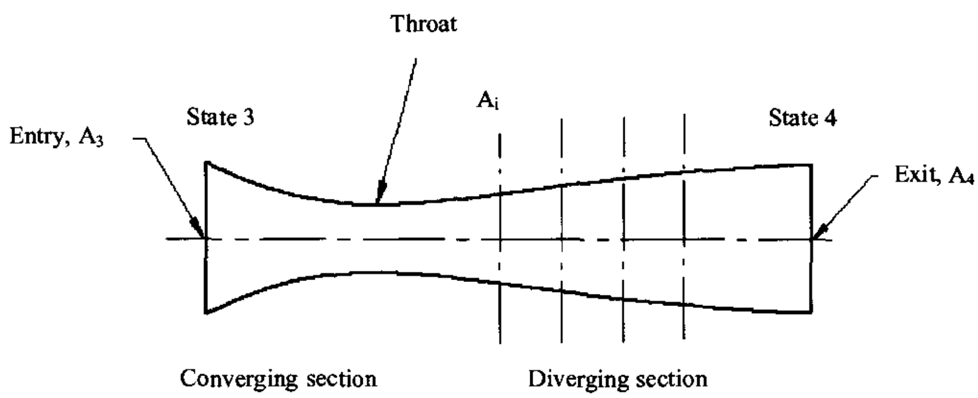

Figure 3.6. Diagram of a Laval nozzle with the gas cycle states

The relationship between the change of nozzle diameter along the axis and a velocity of flow (Mach number) is given by equation [3.19]. The flow is considered isentropic with $M = 1$ at the throat and the diverging portion acting as a nozzle. A normal shock should be at the nozzle exit. The gas flow is modelled as an ideal gas with γ = 1,4. Therefore, the tables for compressible flows can be used [Moran, 1998:432]. The input to the reference table is the ratio of areas, $\frac{A}{A^*}$. Since $M = 1$ at the throat $A^* = A_{throat}$. Hence the ratio of diameters is

$$\frac{A}{A^*} = \frac{A_4}{A_{throat}} = \frac{D_4}{D_{throat}}. \qquad [3.47]$$

Given the value to diameter D_4 the ratio can be found. It is important to find such a value of D_4 that will provide a complete expansion of gas. This means that the pressure p_4 at the exit should be equal or close to the atmospheric pressure. Then a normal shock takes place at the exit of the nozzle. If the pressure p_4 is greater than the atmospheric pressure then the flow is *underexpanded*, and a maximum velocity is not achieved. If, on the other hand, the pressure p_4 is less than the atmospheric pressure the flow is *overexpanded* and a normal shock takes place inside the nozzle, which would also slow the flow.

The calculation of the flow properties of the thermal gun is shown in Appendix A. From the numerical modelling, the calculated flow characteristics at state 3, which is at the entry to the nozzle, are shown in Table 3.1 (See page A7 of Appendix A).

Table 3.1. The flow characteristics at state 3

Property	**Value**
Density, kg/m^3	3,20
Specific heat, J/kg K	1052
Gas constant, J/kg K	300
Mass flow rate, kg/s	0,186
Temperature, K	1477
Pressure, MPa	0,775

The geometry of the nozzle converging section was chosen according to the thermal gun dimensions. The entry nozzle diameter was chosen the same as the diameter of the inner combustion chamber. The length of the converging section was chosen according to the length of the nozzle holder (See Appendix E).

According to the calculation shown in Appendix A, the nozzle included angle of the diverging section should be 5° - 6°. Figure 3.7 shows the optimum nozzle bore geometry with a fixed nozzle throat of 16 mm and included angle of 5°. The nozzle varying parameters are the length of the diverging section from 50 to 150 mm and the corresponding exit diameters. Because the nozzle wears out, the minimum range of diameters were chosen for the design.

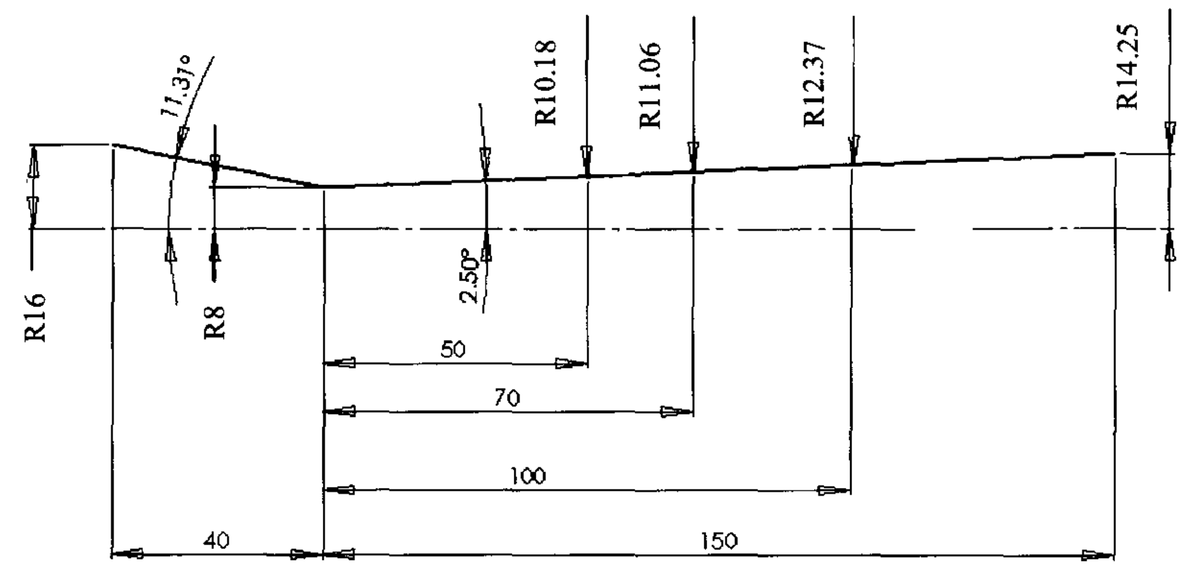

Figure 3.7. Calculated optimum bore geometry of a thermo jet nozzle

The external surface of the nozzles is exposed to natural cooling (free convection) or to forced cooling. Appendix B includes the diagrams of different arrangements of the nozzles fitted to the thermal gun.

If a nozzle is not covered by an housing, the cooling takes place in the atmosphere, e.g. free convection. It has been noticed that the WC nozzles start oxidizing if they are cooled in the atmosphere. It is assumed that cobalt, which is a binder, starts reacting with the oxygen and forms a yellowish powder. The ceramic nozzles were modelled with and without forced cooling to assess the stresses.

The forced cooling on the diverging section of a nozzle was achieved in two different ways. In the first arrangement a portion of the compressed air from the system/gun was directed to the nozzle outer surface. In the other arrangement, a suction effect of supersonic flow was used, where the nozzle was covered with an housing with suction holes (See Appendix B). The housing is longer than the nozzle and has a diameter twice that of the nozzle outer diameter in order to create a suction channel. The tests showed that this method provided sufficient cooling of the diverging section of the WC nozzles.

3.3 Turbulence Modelling

Turbulence modelling is important in designing high velocity air flame systems because they employ premixed flames. Mathematical models of turbulence are used to determine the Reynolds stresses and turbulent scalar fluxes. These models comprise additional differential or algebraic equations that relate the stresses and scalar fluxes to averaged properties of the turbulence field and also provide a framework for calculating these properties. Special models can also be employed to characterise the flow near solid walls.

The models used for general applications are variations of the well known k-ε model, all consisting of transport equations for the turbulent kinetic energy k and its dissipation rate ε. The 'standard' model, in which the high (turbulent) Reynolds number forms of the k and ε equations were used in conjunction with algebraic 'law of the wall' representations of flow, heat and mass transfer for the near-wall region.

The size of the scales of turbulence determines the character of the turbulent flame Turns (2000). The Kolmogorov scale is the smallest length scale associated with a turbulent flow, and as such is representative of the dimension at which the dissipation of turbulent kinetic energy to fluid internal energy occurs. In order to calculate the Kolmogorov length scale l_K, the Reynolds number must be estimated, based on the integral scale l_0. It is assumed that the relative turbulence intensity is approximately 10% and that the integral length scale about l_0 = 1/10 the combustion chamber diameter.

Referring to Figure 3.8, the combustion zone is divided into three sectors. The first zone is the combustion inlet, the second zone is the primary zone and the third zone is the dilution zone.

In order to calculate mass flow rates the proportions of air, fuel and abrasives must be estimated in each zone. It was estimated that there are approximately 45% of the oxidizer in the inlet and the primary zone. In the dilution zone, the density of air/abrasive mixture was taken into account. The fuel mass flow was included in all three stages. The fuel/air ratio was chosen as 0,02 according to the measured mass flow rates at normal operating conditions. The pressure of the compressed air at the intake was taken as 5 bar ($500\cdot10^3$ Pa). The temperatures in the zones from the previous calculations are 300 K, 1800 K and 1477 K, respectively.

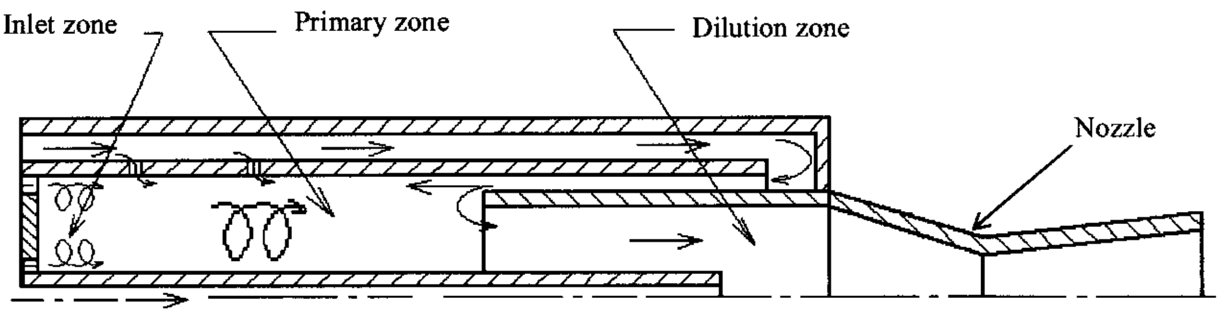

Figure 3.8. Combustion zones of the thermo-abrasive gun model

The mass flows at the combustion inlet and in the primary zone are the same and can be calculated as follows:

$$m_i = 0,45 \cdot m_{total} + 0,02 \cdot m_{total} = 0,45 \cdot 0,12 + 0,02 \cdot 0,12 = 0,056 \text{ kg/s} \quad [3.48]$$

At the end of the dilution zone, the mass flow rate includes the air/abrasive mixture and is $m_3 = 0,186$ kg/s as calculated in Appendix A.

The densities in each zone, using equation [3.40], are:

$$\rho_i = \frac{p_4}{R\,T_4} = \frac{500\cdot10^3}{289\times300} = 5,76 \text{ kg/m}^3 \quad [3.49]$$

$$\rho_{ii} = \rho_i \cdot \frac{T_i}{T_{ii}} = 5,76\frac{300}{1800} = 0,96 \text{ kg/m}^3 \quad [3.50]$$

$$\rho_{iii} = \rho_{mix} = 1,58 \text{ kg/m}^3 \quad [3.51]$$

The velocities in each zone, using equation [3.12], are calculated as follows:

$$U_i = \frac{m_i}{\rho_i \cdot A_i} = \frac{0{,}056}{5{,}76 \cdot 0{,}00018} = 8{,}2\,\text{m/s} \qquad [3.52]$$

$$U_{ii} = \frac{0{,}056}{0{,}96 \cdot 0{,}00018} = 49{,}4\,\text{m/s} \qquad [3.53]$$

$$U_{iii} = \frac{0{,}186}{1{,}58 \cdot 0{,}00126} = 90\,\text{m/s} \qquad [3.54]$$

These values are similar to the ones obtained in Appendix A (equation [A.11], page A5). The velocities of the hot stream and the mixed streams were $U_{hot} = 47$ m/s and $U_{mix} = 80\,\text{m/s}$ respectively.

Reynolds numbers based on the mean flow are:

$$R_{Li} = \frac{\rho U_i D}{\mu} = \frac{5{,}76 \cdot 8{,}2 \cdot 0{,}03}{184{,}8 \cdot 10^{-7}} = 7{,}7 \cdot 10^4 \qquad [3.55]$$

$$R_{Lii} = \frac{\rho U_{ii} D}{\mu} = \frac{0{,}96 \cdot 49 \cdot 0{,}03}{637{,}8 \cdot 10^{-7}} = 2{,}2 \cdot 10^4 \qquad [3.56]$$

$$R_{Liii} = \frac{\rho U_{iii} D}{\mu} = \frac{1{,}58 \cdot 90 \cdot 0{,}04}{550{,}8 \cdot 10^{-7}} = 1{,}03 \cdot 10^5 \qquad [3.57]$$

where: μ = the viscosities at certain temperatures,

D = the diameters of the zones, m.

Reynolds numbers based on the turbulence quantities are:

$$R_{loi} = \frac{\rho U'_i l_0}{\mu} = \frac{5{,}76 \cdot 0{,}1 \cdot 8{,}2 \cdot 0{,}003}{184{,}8 \cdot 10^{-7}} = 770 \qquad [3.58]$$

$$R_{loii} = \frac{\rho U'_{ii} l_0}{\mu} = \frac{0{,}96 \cdot 0{,}1 \cdot 49 \cdot 0{,}003}{637{,}8 \cdot 10^{-7}} = 220 \qquad [3.59]$$

$$R_{loiii} = \frac{\rho U'_{iii} l_0}{\mu} = \frac{1{,}58 \cdot 0{,}1 \cdot 90 \cdot 0{,}004}{550{,}8 \cdot 10^{-7}} = 1030 \qquad [3.60]$$

The Kolmogorov scales are [Turns, 200:433]:

$$\frac{l_0}{l_K} = R_{l_0}^{3/4} \text{ and } l_0 = \frac{D}{10} \qquad [3.61]$$

where: l_0 = the largest length scale, mm,

l_K = the smallest length scale, mm,

D = the combustion chamber diameter, $D = 40$ mm.

Hence,

$$l_{Ki} = l_0 \cdot R_{l_0}^{3/4} = \frac{40}{10} \cdot 770^{-0{,}75} = 0{,}00139\,\text{mm} \qquad [3.62]$$

$$l_{Kii} = l_0 \cdot R_{l_0}^{3/4} = 4 \cdot 220^{-0{,}75} = 0{,}07\,\text{mm} \qquad [3.63]$$

$$l_{Kiii} = l_0 \cdot R_{l_0}^{3/4} = 4 \cdot 1030^{-0{,}75} = 0{,}022\,\text{mm} \qquad [3.64]$$

The calculated scales are small, with the smallest one at the inlet, which represent the thickness of the smallest vortex tubes or filaments that permeate a turbulence flow.

The results of the analytical and numerical modelling are used in the advanced design of a thermal gun, which is shown in the next Section.

4. DESIGN OF THE THERMAL GUN

4.1 Advanced Design of the Thermal Gun

The main difference between the initial and advanced designs is in the way the fuel/air mixture is obtained (Fig. 4.1). The main portion of the oxidizer enters the combustion chamber in an opposite direction to the flow, providing more efficient mixing of fuel and air. Also, the fuel ejection passages are spiral grooves and not holes as in the initial design. This results in high efficiency of the combustion process and more power output.

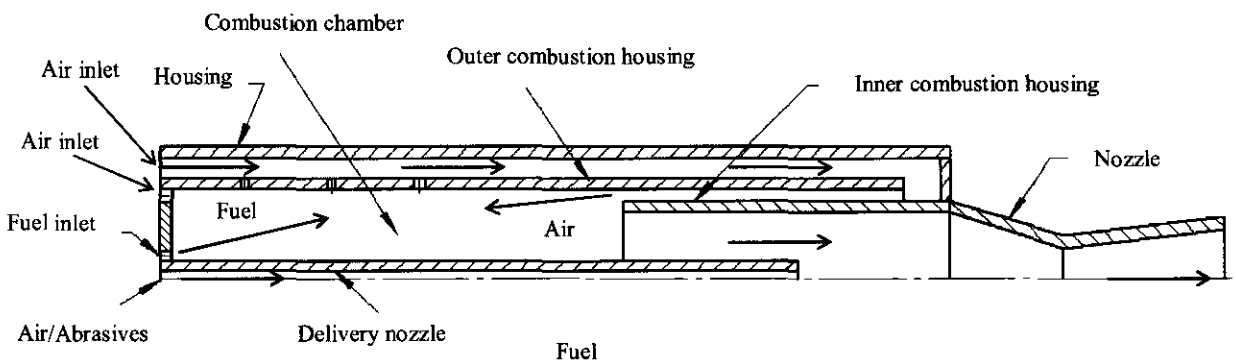

Figure 4.1. Sectional diagram of the improved design of the thermal gun

In the advanced design, the fuel and air first mix in annular passage C (Fig. 4.2). Then the fuel/air mixture is ejected through intersecting spiral grooves N of the injector. As the fuel goes though the spiral grooves it is further broken into fine droplets travelling at high velocity and having vortex movements.

The compressed air for combustion is supplied through hole A (Fig. 4.2). The main steam of the compressed air is first directed to annular passage, D. Then it goes through holes E in the outer combustion chamber housing, into spiral annular passage F, and into the combustion chamber. The spiral grooves accelerate the air flow, which helps to penetrate the air deeper into the combustion chamber. A portion of this air enters the combustion chamber through the radial holes in the outer combustion housing. While going through the annular passages D and F, the air temperature increases by absorbing the heat from the combustion housings.

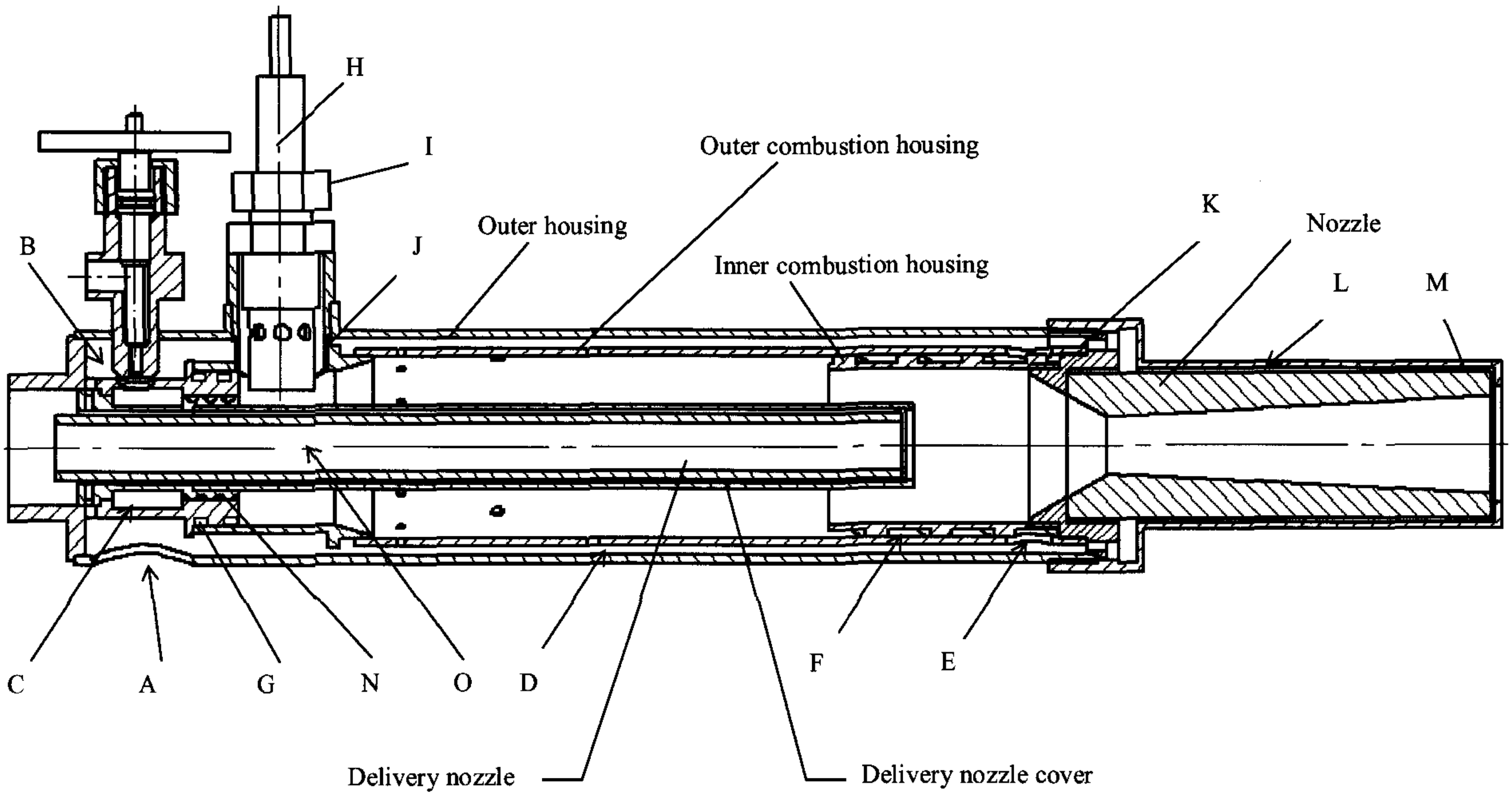

Figure 4.2. Schematic cross section of the advanced design of the thermal-gun

The fuel/air mixture stream and hot air meet in the middle of combustion chamber. This is a final stage of fuel-air mixing.

The main stream of the compressed air enters the combustion chamber in a direction opposite to the stream of fuel/air mixture creating turbulence, which results in a greater mixing of combustion components. The high quality of the fuel/air mixture provides complete combustion, leaving no carbon deposits inside the gun.

The other air stream is directed through spiral grooves G. The purpose of these grooves is to protect the outer combustion chamber housing walls from the fuel droplets depositing on it. This air also cools the housing.

The other feature of the new design is cooling of the nozzle. Small portion of the air from annular passage D goes through holes K in the nozzle holder. This air is used for cooling the nozzle by creating a forced air flow in annular passage L between the nozzle and the housing. The air escapes through holes M in the housing. More details can be found in Appendix E.

The abrasive/air mixture is supplied through the delivery nozzle (Fig 4.2). The flow is then directed through a converging-diverging nozzle. The concentricity of the delivery and the main nozzles is important for particles not to hit the sides of the main nozzle. Otherwise the main nozzle is worn unevenly and turbulence occurs in the flow.

The diameter of the delivery nozzle plays an important role in performance of the thermal gun. The bigger the internal diameter the more abrasive can pass through and, the performance is therefore better. The internal diameter of the delivery nozzle should be within 9 to 13 mm. However, there is a limitation on the external diameter of the nozzle, which is determined by the wall thickness of the nozzle. If the external diameter were too big it would occupy more space of the combustion chamber. Hence, there would be less space for the combustion process and less efficiency of the system, otherwise the size of the chamber must be increased.

The diameters of the delivery nozzle are dependant on a nozzle material and manufacturing processes. The delivery nozzle material must be heat resistant because the nozzle is inside of the area of high combustion temperatures. Also, the delivery nozzle material should be wear resistant as it delivers abrasives at relatively high speed, causing extensive wear.

In this research, two types of the delivery nozzle material were tested. These were stainless steel 310 and tungsten carbide. The former was a standard size pipe of half inch inside diameter. The latter one was a specially designed and pressed WC nozzle. The stainless steel delivery nozzles withstood the heat effect, but they wore out relatively quickly by abrasives. The tungsten carbide nozzles could not stand the high temperatures and oxidized on the outside surface. The solution was to place the tungsten carbide nozzle inside a cover of stainless steel pipe to protect the former from the heat. This is shown in the advanced design of the thermal gun (Fig. 4.2).

The distance between the exit of delivery nozzle and the main nozzle is 12 - 20 mm, which was established experimentally. If the delivery nozzle is too close to the main nozzle it blocks the passage of the hot gases and the thermal gun chokes. If the delivery nozzle is too far from the main nozzle the back pressure is too high and abrasives slow down. The performance of blasting, in this case, is significantly reduced. Also small particles of abrasives are burnt because they stay in the hot gas flow longer.

The delivery nozzle ideally should also have a form of a Laval nozzle. This would decrease wall resistance and increase the velocity of the flow. However, the size, the material and the manufacturing constraints do not allow such a design of the delivery nozzle. For example, tungsten carbide or ceramic nozzles require a wall thickness of 3 - 4 mm. At a nozzle length of 220 mm and a small wall thickness the manufacturing processes become too expensive.

As the result of tests the specifications of the thermal gun were established. They are presented in Tables 4.1 – 4.4.

Table 4.1 Process operating specifications

Characteristic	**Value**
Compressed air flow rate, m^3/h	200 – 320
Fuel consumption, l/h	5,0 – 8,0
Abrasive particles flow rate, m^3/h	0,10 – 0,15
Maximum particle size, mm	2,00
Pressure at the entry into the system, MPa	0,3 – 0,9

Table 4.2 Specifications of the combustion chamber housing

Inside diameter, mm	40 - 48
Wall thickness, mm	2 - 2,5
Length, mm	190 - 220

Table 4.3 Specifications of the blasting nozzle

Diameter of critical section, mm	14,0 -18,0
Included exit angle	$2° – 5°$
Length of diverging part, mm	70 – 100

Table 4.4 Specifications of the delivery nozzle

Internal diameter, mm	9,0 -13,0
External diameter not more than, mm	17
Distance from the exit to the blasting nozzle, mm	12 – 20

4.2 Ignition System

A new method of igniting HVAF apparatus evolved in this research. The method is based on achieving a flame by means of a flame glow plug. Flame glow plugs are used for preheating diesel engines operating in cold regions. The diagram of the flame glow plug is shown in Figure E.11 of Appendix E.

Referring to Figure 4.2, flame glow plug H is positioned on the top of the gun. The heating element of the flame glow plug is positioned inside the combustion chamber. The fuel is supplied to the flame glow plug through fuel inlet I. An injector inside the flame glow plug dispenses a small quantity of fuel depending on the pressure in the fuel line. The conditions for the flame glow plug to ignite had to be similar to those on diesel engines. Therefore, holes J in the plug housing were made in order to provide passages for air for igniting a flame. If the air stream is too strong it cools down the heating element and no ignition takes place. On the other hand, too little air would not ignite a flame. The sizes and positions of the holes for the air passage were determined experimentally to achieve reliable ignition of the flame glow plug. Small amounts of fuel and air are supplied to the flame glow plug while it is heated up to 1000°C. It takes 15 – 20 seconds to ignite a flame. Once there is a flame inside the combustion chamber, the main air and fuel are simultaneously opened and combustion is achieved.

4.3 Nozzle Designs and Materials

The nozzle bore geometry was determined in Section 3 and Appendix A (pages A7 – A12). The nozzle external geometry depends on a type of material, a fabrication process and a cooling method. The possible nozzle materials include tungsten carbide, hot pressed SiC, nitride-bonded SiC and SIALON. The material properties are shown in Table B.1 of Appendix B.

In this investigation, five different types of WC nozzles were used of which one was a conventional sandblasting nozzle (Fig. 4.3) and four types of WC nozzles were designed and manufactured. The designed WC nozzles differ in the nozzle throat diameter and the length of the diverging section. The nozzles were manufactured by Powder Industries (Pty) Ltd, situated in Johannesburg. All the WC nozzles were made of the same material.

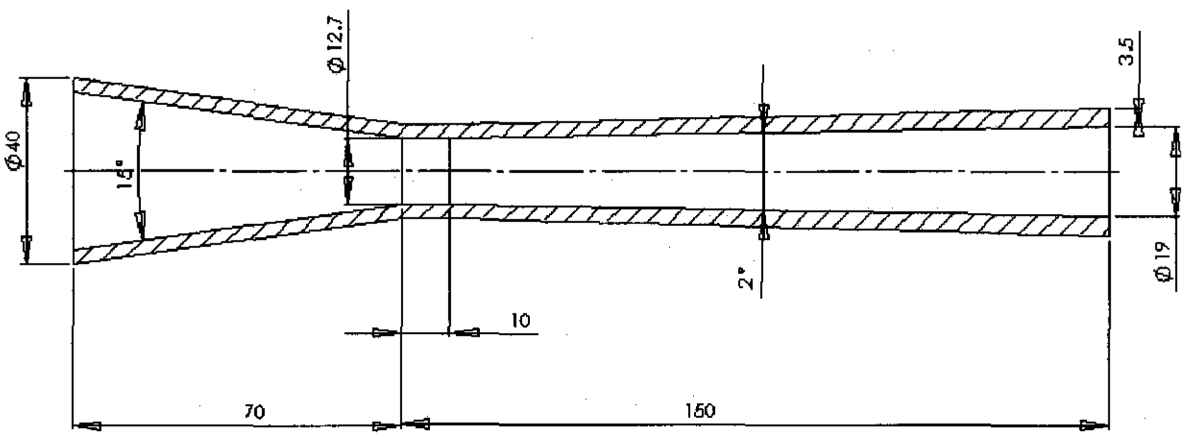

Figure 4.3. Diagram of the conventional abrasive blasting WC nozzle

The conventional abrasive blasting WC nozzle has a Laval shape with a straight piece at the beginning of the delivering section (Fig. 4.3). This is made specifically for keeping the nozzle throat at the same size during wear. A productivity of conventional sandblasting is very sensitive to the size of the nozzle throat. A small increase in the nozzle throat diameter results in a substantial pressure drop.

Two short WC nozzles were made from the standard nozzles by machining the pre-sintered billets (Fig. 4.4). The billets were first pressed in the existing form and pre-sintered. Then, the workpieces were cut to two sizes of 50 mm and 70 mm length of the diverging section. The nozzle bore was machined from 12,75 mm to 15 mm diameter afterwards. Because of that the wall thickness got smaller than 3 mm in some places of the nozzles. The nozzles were then finally sintered. The sections of the nozzles are shown in Figure 4.4.

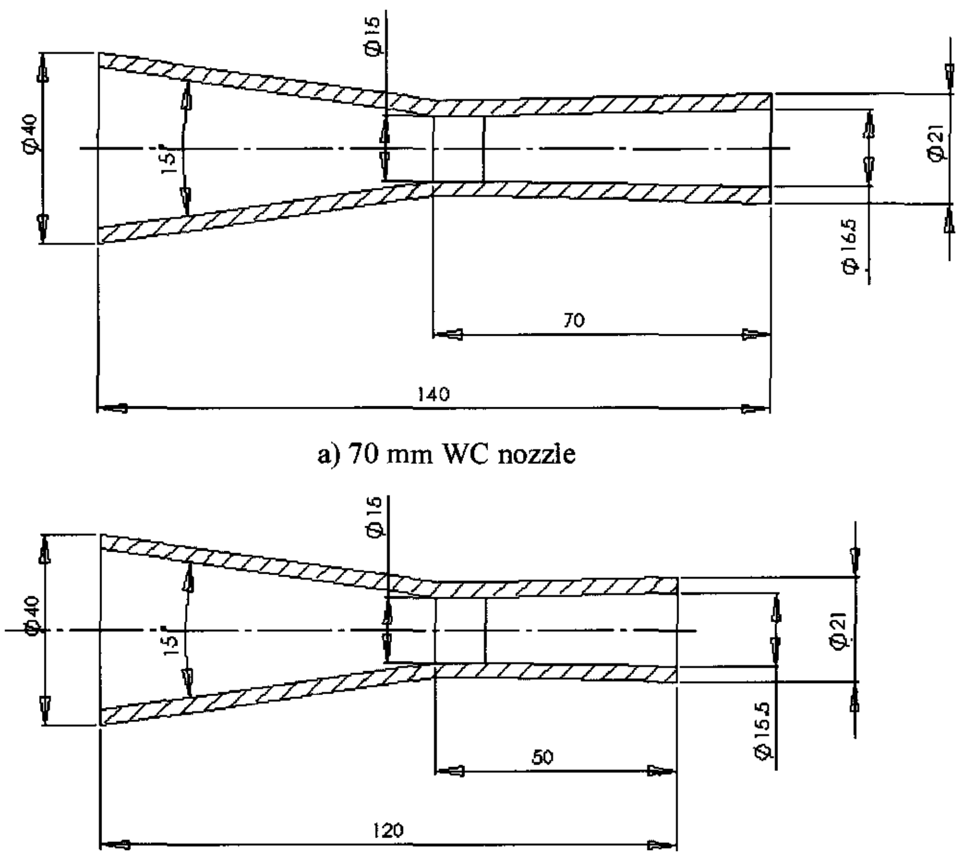

a) 70 mm WC nozzle

b) 50 mm WC nozzle

Figure 4.4. Sections of the WC nozzles with 15 mm bore size

The geometry of the 50 mm and 70 mm nozzles is not completely satisfactory because of the long converging section, which does not fit inside the nozzle holder, as can be seen in Figure B.3 of Appendix B. Therefore, it is more difficult to cool down the diverging section of the nozzle. However, the nozzles were made for a purpose of testing the nozzle throat and the length of diverging section in correlation with a speed of blasting.

Figure 4.5 shows two WC nozzles, which were specially designed. They have the same length but a different nozzle throat size. The two nozzle throat diameters were 16 and 17 mm, which were chosen according to the calculation done in Section 3. These nozzles were manufactured from the specially manufactured billet. The converging section of the nozzles was designed to fit inside the nozzle holder for cooling purposes. The outer surface of the diverging section was made cylindrical to achieve effective forced cooling because it provides an even size of the cooling passage along the nozzle axis (Figure B.2 of Appendix B).

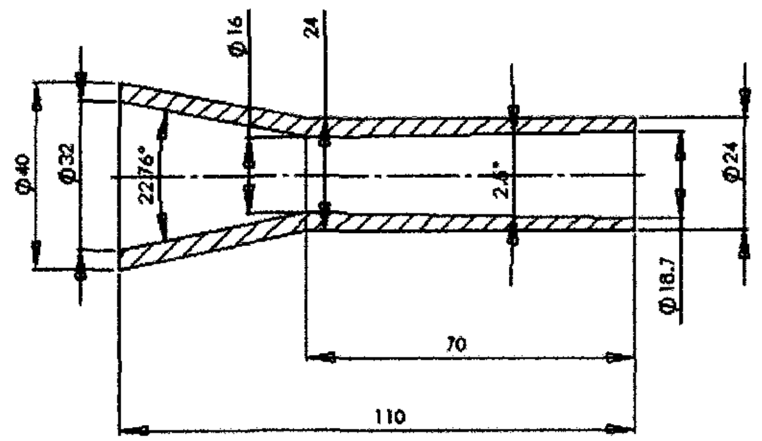

a) 16 mm bore size

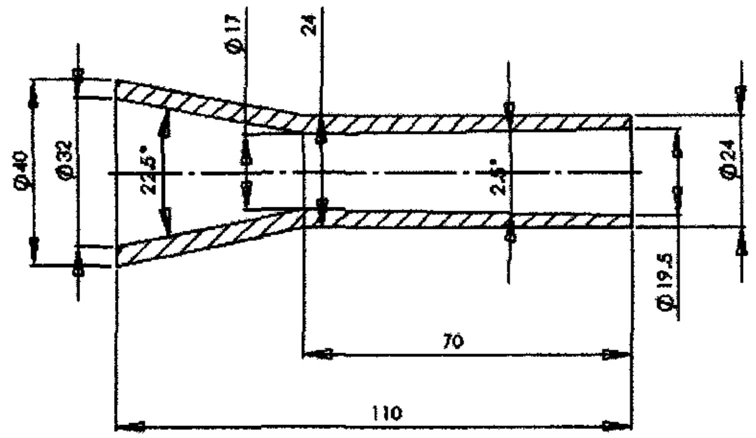

a) 17 mm bore size

Figure 4.5. Sections of the WC nozzles with 16 and 17 mm bore sizes

Other types of conventional sandblasting nozzle designs were also tested in this research. For example, Figure 4.6 shows a WC nozzle, which is used for blasting inside pipes and called an angle nozzle. The angle nozzle does not have the diverging section, instead it has three circumferential exit holes at an angle of 60° to the nozzle axis. Angle nozzles are used for blasting inside pipes of diameter from 70 to 250 mm.

SIALON blasting nozzles, used in this research, were produced by a company known as Boride Inc. The SIALON blasting nozzle has the same geometry as a WC conventional nozzle (Fig. 4.3).

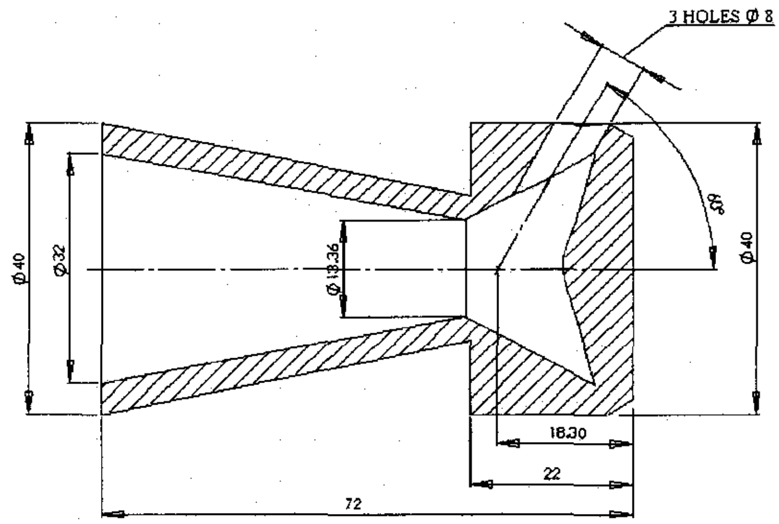

Figure 4.6. Section of the WC nozzle for blasting inside pipes

Two types of SiC nozzles were made locally for testing. The geometry of the nozzles made of hot pressed SiC and nitride-bonded SiC is shown in Figure 4.7. The manufacturer could only make the geometry shown. The geometry of the diverging section complies with the calculated geometry. The converging section was shorter because of the manufacturing constraints. The angle of the diverging section could not be made bigger than 3^0 because it would reduce the wall thickness.

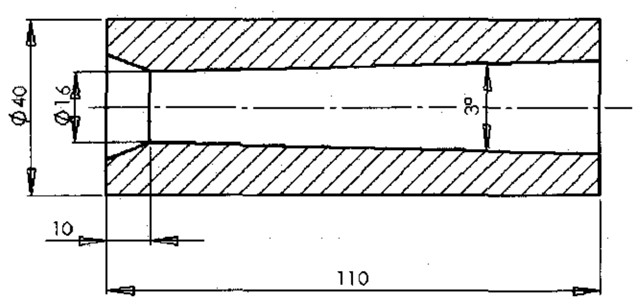

Figure 4.7. Section of the SiC nozzle

The geometries of the thermal gun and the nozzles are used in the computational fluid dynamics analysis shown in the next Section.

5. COMPUTATIONAL MODELLING OF THE THERMAL GUN

5.1 Basic Conservation Equations

The modelling of the process inside the thermal gun was done with computational fluid dynamics software, namely STAR-CD. The following basic conservation equations are applied in the modelling within STAR-CD software:

5.1.1 Flow Field

The mass and momentum conservation equations for general incompressible and compressible fluid flows and a moving coordinate frame (the 'Navier Stokes' equations) are, Warsi (1981):

$$\frac{1}{\sqrt{g}}\frac{\partial}{\partial t}\left(\sqrt{g}\rho\right)+\frac{\partial}{\partial x_j}\left(\rho\tilde{u}_j\right)=s_m \qquad [5.1]$$

$$\frac{1}{\sqrt{g}}\frac{\partial}{\partial t}\left(\sqrt{g}\rho u_i\right)+\frac{\partial}{\partial x_j}\left(\rho\tilde{u}_j u_i-\tau_{ij}\right)=-\frac{\partial p}{\partial x_i}+s_i \qquad [5.2]$$

where t = time,

x_i = Cartesian coordinate $(i = 1, 2, 3)$,

u_i = the absolute fluid velocity component in direction,

$\tilde{u}_j$ = the relative velocity between fluid and local (moving) coordinate frame that moves with velocity u_{cj},

p = the piezometric pressure,

ρ = the density,

τ_{ij} = the stress tensor components,

s_m = the mass source,

s_i = the momentum source components,

$\sqrt{g}$ = the determinant of metric tensor.

5.1.2 Heat Transfer

The total Chemico-Thermal enthalpy is formed by summing up the mechanical energy conservation and the static enthalpy equations. The general form of the total enthalpy conservation equation for a fluid mixture is as follows, Patankar (1980):

$$\frac{1}{\sqrt{g}}\frac{\partial}{\partial t}\left(\sqrt{g}\rho H\right)+\frac{\partial}{\partial x_j}\left(\rho\tilde{u}_j H - F_{h,j} - u_i\tau_{ij}\right)=\frac{1}{\sqrt{g}}\frac{\partial}{\partial t}\left(\sqrt{g}p\right)-\frac{\partial}{\partial x_i}\left(u_{cj}p\right)+s_i u_i + s_h \qquad [5.3]$$

where T = the temperature,

H = the chemico-thermal enthalpy,

$F_{h,j}$ = the diffusional energy flux in direction x_j,

s_h = the energy source.

5.1.3 Conduction and Conjugate Heat Transfer

Conduction and conjugate heat transfer is applicable to conjugate heat transfer problems, i.e. those in which the temperature is to be simultaneously determined within a fluid and a neighbouring solid. For this purpose, it is assumed that the solid is isotropic, so that within it the following degenerate form of equation applies:

$$\frac{\partial(\rho e)}{\partial t}=\frac{\partial}{\partial x_j}\left(k\frac{\partial T}{\partial x_j}\right)+s_e \qquad [5.4]$$

where $e = c_v T$ is the specific internal energy and the thermophysical properties of the solid material. Heat generation/dissipation may be specified using s_e, as in the fluid.

In the STAR-CD solution procedure, the energy equations for the fluid and solid are solved simultaneously and continuity of energy flux is enforced at the fluid/solid interfaces.

5.1.4 Turbulence Modelling

It is generally recognised that turbulence modelling is a complex problem and has a considerable degree of approximation. The main options of turbulence modelling available in STAR-CD software are the variations of the k–ε model, all comprising transport equations for the turbulent kinetic energy k and its dissipation rate ε. STAR-CD software provides both linear and non-linear turbulence models. All the linear models are unable to model anisotropic effects. Non-linear models, on the other hand, may prove a better alternative for flows where anisotropy, turbulence intensity gradients or secondary strain rates are important.

The linear models included in STAR-CD software are as follows:

- The 'standard' model, in which the high (turbulent) Reynolds number forms of the k and ε equations are used in conjunction with algebraic 'law of the wall' representations of flow, heat and mass transfer for the near-wall region.
- The low Reynolds number model in which general transport equations for k and ε are solved everywhere, including the near-wall regions. 'Law of the wall' representations are therefore not required.
- The 'Renormalisation Group' (RNG) version of the k-ε model, which is employed in high Reynolds number form in conjunction with 'law of the wall' functions.
- A modified version of the k–ε model, known as Chen's k-ε model, which employs both the production and dissipation time scales in closing the dissipation equation. This model is also utilised in high Reynolds number form in conjunction with 'law of the wall' functions.
- 'Two-layer' models, in which the near-wall flow is simulated via one-equation low Reynolds number model consisting of a transport equation for k and an algebraic prescription for the turbulence length scale. The solution is matched to that of the standard k-ε equations at the 'edge' of the viscosity-influenced region.

All forms of the k-ε and k-l linear models contained in STAR-CD software assume that the turbulent Reynolds stresses and scalar fluxes are linked to the ensemble-averaged flow properties in an analogous fashion to their laminar flow counterparts. See Launder and Spalding (1974).

$$-\overline{\rho u_i' u_j'} = 2\mu_t s_{ij} - \frac{2}{3}\left(\mu_t \frac{\partial u_k}{\partial x_k} + \rho k\right)\delta_{ij} \qquad [5.6]$$

$$\overline{\rho u_j' h'} = -\frac{\mu_t}{\sigma_{h,t}} \frac{\partial h}{\partial x_j} \qquad [5.7]$$

$$\overline{\rho u_j' m_m'} = -\frac{\mu_t}{\sigma_{h,t}} \frac{\partial m_c}{\partial x_j} \qquad [5.8]$$

where

$$k \equiv \frac{\overline{u_i' u_i'}}{2} \qquad [5.9]$$

is the turbulent kinetic energy, μ_t is the turbulent viscosity, $\sigma_{h,t}$ and $\sigma_{m,t}$ are the turbulent Prandtl and Schmidt numbers, respectively. The above equations effectively define these quantities.

The turbulent viscosity is linked to k and ε via

$$\mu_t = f_\mu \frac{C_\mu \rho k^2}{\varepsilon} \qquad [5.10]$$

or to k and l via

$$\mu_t = f_\mu C_\mu^{1/4} \rho k^{1/2} l \qquad [5.11]$$

where C_μ is an empirical coefficient, usually taken as a constant, and is another coefficient, to be defined when the individual model variants are presented. The turbulent Prandtl and Schmidt numbers are also empirical quantities that are usually assigned constant and equal values.

An expression relating k, ε and l is as follows:

$$l = C_\mu^{3/4} \frac{k^{3/2}}{\varepsilon} \qquad [5.12]$$

a) Standard k-ε Turbulence Model

The transport equations of the standard k-ε turbulence model (linear and non-linear) are as follows, El Tahry (1983):

Turbulence energy

$$\begin{aligned}&\frac{1}{\sqrt{g}}\frac{\partial}{\partial t}\left(\sqrt{g}\rho k\right)+\frac{\partial}{\partial x_j}\left[\rho\tilde{u}_j k-\left(\mu+\frac{\mu_t}{\sigma_k}\right)\frac{\partial k}{\partial x_j}\right]=\\&=\mu_t\left(P+P_B\right)-\rho\varepsilon-\frac{2}{3}\left(\mu_t\frac{\partial u_i}{\partial x_i}+\rho k\right)\frac{\partial u_i}{\partial x_i}+\mu_t P_{NL}\end{aligned} \qquad [5.13]$$

where

$$P\equiv 2s_{ij}\frac{\partial u_i}{\partial x_i} \qquad [5.14]$$

$$P_B\equiv -\frac{g_i}{\sigma_{h,t}}\frac{1}{\rho}\frac{\partial \rho}{\partial x_j} \qquad [5.15]$$

$$P_{NL}=-\frac{\rho}{\mu_t}\overline{u_i u_j}\frac{\partial u_i}{\partial x_j}-\left[P-\frac{2}{3}\left(\frac{\partial u_i}{\partial x_i}+\frac{\rho k}{\mu_t}\right)\frac{\partial u_i}{\partial x_j}\right] \qquad [5.16]$$

P_{NL} is an empirical coefficient, $P_{NL} = 0$ for linear models. The first term on the right-hand side of equation [5.13] represents turbulent generation by shear and normal stresses and buoyancy forces, the second viscous dissipation, and the third amplification or attenuation due to compressibility effects. The last term accounts for the non-linear contributions.

Turbulence dissipation rate

$$\begin{aligned}&\frac{1}{\sqrt{g}}\frac{\partial}{\partial t}\left(\sqrt{g}\rho\varepsilon\right)+\frac{\partial}{\partial x_j}\left[\rho\tilde{u}_j\varepsilon-\left(\mu+\frac{\mu_t}{\sigma_\varepsilon}\right)\frac{\partial\varepsilon}{\partial x_j}\right]=\\&=C_{\varepsilon1}\frac{\varepsilon}{k}\left[\mu_t P-\frac{2}{3}\left(\mu_t\frac{\partial u_i}{\partial x_i}+\rho k\right)\frac{\partial u_i}{\partial x_i}\right]+C_{\varepsilon3}\frac{\varepsilon}{k}\mu_t P_B-C_{\varepsilon2}\rho\frac{\varepsilon^2}{k}+C_{\varepsilon4}\rho\varepsilon\frac{\partial u_i}{\partial x_i}+C_{\varepsilon1}\rho\frac{\varepsilon}{k}\mu_t P_{NL}\end{aligned} \qquad [5.17]$$

Table 5.1: Values assigned to the standard *k*-ε turbulence-model coefficients

C_μ	σ_k	σ_ε	σ_h	σ_m	$C_{\varepsilon 1}$	$C_{\varepsilon 2}$	$C_{\varepsilon 3}$	$C_{\varepsilon 4}$	k	E
0,09	1,0	1,22	0,9	0,9	1,44	1,92	0 or 1,44	-0,33	0,42	9,0

b) RNG k-ε Turbulence Model

The formulation employed in STAR-CD software for the RNG *k*-ε turbulence model is as follows, Yakhot (1992):

Turbulence energy

$$\frac{1}{\sqrt{g}}\frac{\partial}{\partial t}\left(\sqrt{g}\rho k\right)+\frac{\partial}{\partial x_j}\left[\rho\tilde{u}_j k-\frac{\mu_{eff}}{\sigma_k}\frac{\partial k}{\partial x_j}\right]=\mu_t\left(P+P_B\right)-\rho\varepsilon-\frac{2}{3}\left(\mu_t\frac{\partial u_i}{\partial x_i}+\rho k\right)\frac{\partial u_i}{\partial x_i} \quad [5.18]$$

Turbulence dissipation rate

$$\begin{aligned}&\frac{1}{\sqrt{g}}\frac{\partial}{\partial t}\left(\sqrt{g}\rho\varepsilon\right)+\frac{\partial}{\partial x_j}\left[\rho\tilde{u}_j\varepsilon-\frac{\mu_{eff}}{\sigma_\varepsilon}\frac{\partial\varepsilon}{\partial x_j}\right]=\\&=C_{\varepsilon1}\frac{\varepsilon}{k}\left[\mu_t P-\frac{2}{3}\left(\mu_t\frac{\partial u_i}{\partial x_i}+\rho k\right)\frac{\partial u_i}{\partial x_i}\right]+C_{\varepsilon3}\frac{\varepsilon}{k}\mu_t P_B\\&-C_{\varepsilon2}\rho\frac{\varepsilon^2}{k}+C_{\varepsilon4}\rho\varepsilon\frac{\partial u_i}{\partial x_i}-\frac{C_\mu\eta^3\left(1-\eta/\eta_0\right)}{1+\beta\eta^3}\frac{\rho\varepsilon^2}{k}\end{aligned} \quad [5.19]$$

where

$$\eta\equiv S\frac{k}{\varepsilon} \quad [5.20]$$

$$S\equiv\left(2s_{ij}s_{ij}\right)^{1/2} \quad [5.21]$$

η_0 and β are empirical coefficients shown in Table 5.2.

The distinctive feature of the RNG *k*-ε model is the additional, last term in the dissipation equation. This is a modelled form of a term that arises from the RNG analysis and represents the effect of mean flow distortion on ε.

Table 5.2 Values assigned to standard the RNG k-ε turbulence-model coefficients

C_μ	σ_k	σ_ε	σ_h	σ_m	$C_{\varepsilon 1}$	$C_{\varepsilon 2}$	$C_{\varepsilon 3}$	$C_{\varepsilon 4}$	k	E	η	β
0,085	0,719	0,719	0,9	0,9	1,42	1,68	0 or 1,44	-0,387	0,4	9,0	4,38	0.012

Most research studies in this field suggest the use of the standard $k-\varepsilon$ model or the RNG k-ε model for modelling turbulence of combustion flows. Reitz and Rutland (1995) studied combustion and turbulence models of a diesel engine and concluded that there were minor differences in the predicted pressure and heat release rates between the standard and RNG turbulent models.

The use of turbulence models requires imposition of the appropriate boundary conditions. The types of boundaries requiring particular attention are walls (especially when the high Reynolds number models are used) and inflow streams.

The turbulence-modelling options for wall boundary conditions available in STAR-CD offer two ways of imposing the no-slip conditions on walls and calculating the resulting boundary layers. These are the 'Two layer' and 'Wall function' approaches.

a) Two layer approach

The no-slip conditions are applied directly and the boundary layers are computed by solving the mass, momentum and turbulence equations within them. In this approach, the wall regions are treated the same way as the interior flow, with the no-slip condition imposed at the boundary cell faces. The only distinction is that at some distance from the wall a switch is made from the high Reynolds number $k-\varepsilon$ model to the selected low Reynolds number k-l or mixing length model. A fine mesh of at least 15 cross-stream grid points is employed near the wall, up to a thickness sufficient to encompass the near-wall region.

b) Wall function approach

In the wall function approach, algebraic relations based on the 'known' distributions of velocity, temperature and turbulence parameters in a one-dimensional equilibrium flow are used to 'bridge' the boundary layer. Thus, they effectively provide turbulence boundary conditions at the layer's outer edge for the solution of the turbulence transport equations.

For the purposes of numerical calculation, the 'law of the wall' distributions of velocity, temperature and other variables are assumed to prevail across the boundary layer. The latter is spanned by a single grid cell whose central node is assumed to be positioned at a distance of ~30-100y^+ units from the wall. If the node is placed too close, the utility of the wall functions is lost; if it is placed too far away, then the profiles are more likely to have departed from their assumed shape. The wall functions are used to link the fluxes through the wall face of the boundary cell to those at the central node. They are also used to modify the calculation of the 'source' terms in the turbulence transport equations.

5.1.5 Combustion Modelling

Combustion modelling is a key element in the modelling of HVAF systems. Combustion is a phenomenon, which involves thermo-chemistry and fluid dynamics. Veynante and Vervisch (2002) highlighted the following features of combustion modelling:

- The fluid mechanical properties of the combustion systems must be well known to carefully describe the mixing of the reactants and, more generally, all transfer phenomena occurring in turbulent flames (heat transfer, molecular diffusion, convection, turbulent transport etc.).
- Detailed chemical reaction schemes are necessary to estimate the consumption rate of the fuel, the formation of combustion products and pollutant species. A precise knowledge of the chemistry is absolutely required to predict ignition, stabilization or extinction of reaction zones together with pollution.
- Two (liquid fuel) and three (solid fuel) phase systems may be encountered. Liquid fuel injection is a common procedure and the three-dimensional spatial distribution of gaseous reactants depends on complex interaction between the breakdown of the liquid sheets, the vaporization of the liquid, turbulent mixing, and droplet combustion.
- Radiation heat transfer is generated within the flame by some species and carbon particles resulting from soot formation and transported by the flow motion.

HVAF combustion is especially difficult to model. For example, if liquid fuel is used, sub-models are required for turbulence, spray injection, atomisation, break-up, coalescence, vaporization, ignition, premixed combustion, diffusion combustion, wall heat transfer, and emissions (soot and NO_x). All of these sub-models must work together in turbulent flow fields.

Because of a high velocity of the flow, combustion inside the thermal gun is considered turbulent. In turbulent combustion, the differences are further complicated by the complexities of chemical kinematics and the strong non-linear coupling of the turbulence and the chemistry, Bilger (2000). Turbulent combustion is applicable to industrial furnaces, internal combustion engines, turbines, explosions etc.

A flame structure is an important element of turbulent combustion. There are three types of flame structures. These are non-premixed, premixed and partially premixed flames.

- Non-premixed combustion is of practical importance in diesel engines, liquid fuel gas turbines, furnaces and fires. Most non-premixed problems are of the type that involves mixing and reaction of only two streams, one of fuel and the other of oxidant.
- Premixed combustion is of practical importance in spark-ignition engines, modern gas-fuelled gas turbine engines, jet engine afterburners and explosions. Here the fuel and air are essentially premixed to a mixture that is uniform in composition and temperature. Combustion occurs by the propagation of a front separating essentially unburnt mixture from essentially fully-burnt mixture.
- Partially premixed combustion is found in many furnaces where the fuel is partially premixed with so-called "primary air" before entering the combustor. This is also the situation in gas turbines with pre-vaporisers. Stratified charge engines and the so-called homogeneous charge compression ignition engine have considerable premixing of the fuel.

In the design of the thermal gun, the fuel and air are partially premixed before entering the combustion chamber. Therefore, the models of partially premixed flames are considered to be applicable to the model of the thermal gun.

There are two general approaches in solving combustion reactions, chemical kinetics and the Probability Density Function (PDF) method or their combinations and variations. Chemical kinetics is concerned with the mechanisms and rates of reaction of chemical species at the molecular level. This information is essential for modelling purposes, but highly system-specific (i.e. dependent on the nature of reactants, pressure, temperature, etc.) and often difficult to obtain. Reaction mechanisms vary in size and complexity from simple schemes involving a few species and a single reaction step, e.g. the irreversible reaction, to highly complex systems with thousands of species and hundreds of reactions. For example, Haworth et al. (2000) proposed a chemical kinematics for propane-air combustion consisting of 73 reactions. Many commercial computational fluid dynamics software do not allow such a number of reactions to be modelled. For example, the version of STAR-CD software, used in this research, can only model up to 50 chemical reactions.

Simple, so called 'artificial' reaction schemes are often constructed as approximations to the more complex ones, to make them more tractable to analysis. The accuracy of the analysis is then dependent on the validity of the approximations.

If the flow is turbulent, the conventional method of solving for the average values of the species concentrations, temperature and other variables gives rise to further complications when the chemical reactions are to be evaluated; because these are usually non-linear functions. Additional 'turbulent reaction' modelling is therefore necessary to evaluate the average reaction rates. Such models are available but they have their own sets of underlying approximations and uncertainties, Veynante and Vervisch (2002). Moreover, these models are non-universal and depend on the type of flame structure, i.e. non-premixed, premixed and partially premixed models.

According to Bilger (2000), many systems with some primary air admixed with the fuel have a flame structure with diffusion-controlled reaction zones with diffusion essentially in the direction of the mixture fraction gradient and they can be satisfactorily modelled by models developed for non-premixed flames, i.e. PDF. Saxena and Pope (1999) also indicated that a PDF approach is the most suited method for turbulent-reactive flows since complex reactions can be treated without modelling assumptions.

The standard Presumed Probability Density Function (PPDF) model was developed to predict non-premixed or 'diffusion' flames formed at the interface between separately-introduced fuel-bearing and oxidant-bearing streams. This model employs the 'fast-kinetics' assumption, which results in having turbulent mixing between the streams as the rate-controlling process.

The standard PPDF model described by Richardson et al. (1953) characterises the mixing process in terms of:

1. The time-average fields of the mixture fraction f and its mean square fluctuations or variance, defined as

$$g_f \equiv f'^2 \qquad [5.22]$$

where f' is the instantaneous fluctuation about the mean and the overbar denotes the time average. Each field is governed by its own differential transport equation.

2. A presumed form of probability density function (PDF) for the instantaneous mixture fraction $\hat{f}$, which depends on the above mentioned variables and is denoted by $P(f)$.

The instantaneous temperature $\hat{T}$, density $\hat{\rho}$ and species $\hat{m}$ concentrations can each be uniquely related to f. Their time-average values can then be determined from

$$\phi = \int_0^1 \hat{\phi}(f)P(f)df \qquad [5.23]$$

Where $\hat{\phi}$ stands for any of the above mentioned variables. Thus, the complete model consists of the transport equations for f and g_f, the presumed PDF, $P(f)$ and the set of $\hat{\phi}(f)$ relations for ^T, ^m and $\hat{\rho}$.

The mixture fraction f is obtained by solving the following equation, Richardson et al. (1953):

$$\frac{1}{\sqrt{g}}\frac{\partial}{\partial t}\left(\sqrt{g}\rho f\right)+\frac{\partial}{\partial x_j}\left[\rho\tilde{u}_j f-\left(\rho D_f+\frac{\mu_t}{\sigma_{f,t}}\right)\frac{\partial f}{\partial x_j}\right]=s \qquad [5.24]$$

where $\sigma_{f,t}$ = the turbulent Schmidt number,

D_f = is the molecular diffusivity of constituent f,

μ = the dynamic viscosity,

The source term S represents the addition of fuel into the gaseous phase originating from a second phase, e.g. diesel fuel droplets or coal particles.

The equation for the variance g_f is as follows:

$$\frac{1}{\sqrt{g}}\frac{\partial}{\partial t}\left(\sqrt{g}\rho g_f\right)+\frac{\partial}{\partial x_j}\left[\rho\tilde{u}_j g_f-\left(\rho D_g+\frac{\mu_t}{\sigma_g}\right)\frac{\partial g_f}{\partial x_j}\right]=\frac{2\mu_t}{\sigma_g}\left(\frac{\partial f}{\partial x_j}\right)^2-C_D\rho\frac{\varepsilon}{k}g_f \qquad [5.25]$$

The presumed PDF form is a β function given by

$$P(f)=\frac{f^{a-1}(1-f)^{b-1}}{\int_0^1 f^{a-1}(1-f)^{b-1}df} \qquad [5.26]$$

where

$$a\equiv\frac{f}{g_f}\left[f(1-f)-g_f\right] \qquad [5.27]$$

$$b\equiv\frac{(1-f)}{f}a \qquad [5.28]$$

The functions $\hat{\phi}(f)$ are derived from the particular assumptions made about the instantaneous reactions and are specific to each fuel/oxidant combination. The principal assumptions are:

- The reactions are 'fast', leading to thin burning zones embedded in the turbulent flow field.
- The thermo-chemical state at any point within such a zone is uniquely related to f. This assumption strictly requires that the zone be adiabatic, although empirical means of correcting for heat losses have been devised.

Based on the results of the literature search, combustion modelling in this research was mainly done with the PPDF model, although a chemical kinetic model of a 3-step combustion reaction was also applied to compare the models.

5.1.6 Multiphase Flow Modelling

The Lagrangian/Eulerian approach is used by STAR-CD software for solving multiphase flows, in which the conservation equations of mass, momentum and energy for the dispersed phase are written for each individual element. The governing equations for the continuous phase are expressed in Eulerian form and are suitably modified to take account of the presence of the dispersed phase. For flows involving a (comparatively) small number of dispersed elements, it is possible to solve a set of the aforementioned Lagrangian equations for every element. However, if the number of particles is large, a statistical approach is more practical. The total population is represented by a finite number of computational parcels (samples), each of which represents a group (cluster) of elements having the same properties. The number of samples must be large enough so that the properties of the full population are well represented. This can be assessed, in the absence of any other measures, by performing calculations with different numbers of samples and comparing the results.

For the dispersed phase, STAR-CD software uses the Lagrangian conservation equations for momentum, mass and energy, which were described in Section 1 (equations [1.4] – [1.13]). For the continuous phase, the conservation equations with modifications are as follows:

1. Account is taken of the displacement of the carrier fluid by the dispersed phase, measured by the fractional volume α_c. The necessary modifications to the fluid equations are:
   (a) Replacement of the density ρ_c and effective viscosity μ_{eff} in the transport terms on the left-hand side by the products $\alpha_c\ \rho_c$ and $\alpha_c\ \mu_{eff}$, respectively.
   (b) Multiplication of the right-hand terms representing volume-integrated sources and other effects by α_c.

2. Inter-phase transfer effects are allowed for by including the appropriate source/sink terms, derived from the Lagrangian equations.

The Lagrangian equations, when integrated over the control volume, yield the changes in the momentum, mass and energy of each discrete element between its entry and exit. The sum of these changes for all elements crossing the volume provides, with change of sign, the net momentum, mass and energy exchanged with the carrier fluid. These are the 'source terms' for the continuous phase equations.

5.2 Model Physics

The model of the thermal gun consists of a combustion chamber and different nozzle models. The combustion chamber of the thermo-abrasive gun is similar to a can-type combustion chamber of a gas turbine, Cohen (1996), scaled down to a hand-held device. The combustion chamber has a number of sets of air inlets placed circumferentially at the combustor head to promote maximum mixing and flame stabilisation (Fig. 5.1).

Similar to a ramjet, the nozzle is directly coupled to the combustion chamber. A nozzle bore diameter of 16 mm was used in the simulation. This was calculated using the multiphase flow properties obtained in Section 3. The lengths of the nozzle diverging section were chosen as 50, 70, 100, 120 and 150 mm. These values were alternatively used for the simulation. Different nozzle geometries (straight and Laval-type) were also modelled in order to compare the velocities of the gas flow and the abrasives.

The air used for combustion enters through a number of inlets (Fig. 5.1). Approximately 80% of the air, directed to the combustion chamber, enters through inlet 1 and travels between the outer and inner combustion housings. This air enters the combustion zone in an opposite direction to the flame, creating the turbulence needed for mixing of fuel and air. A small portion of this air passes through the holes in the outer combustion housing creating additional turbulence and improving premixing of fuel and air.

Approximately 20% of the air, directed to the combustion chamber, enters the combustion zone swirling through sets of inlets. The first set (not shown) is nearest to fuel inlet 3. This stream mixes with fuel at the entry to the combustion zone. The second set (Inlet 2) is at the wall of the combustion chamber housing. Air passing though this inlet protects the combustion housing wall from overheating by forming a high velocity air layer.

The fuel stream is injected through inlet 3. The air/abrasive mixture enters the combustion zone through the delivery nozzle (Inlet 4), which is concentric with the combustion housing.

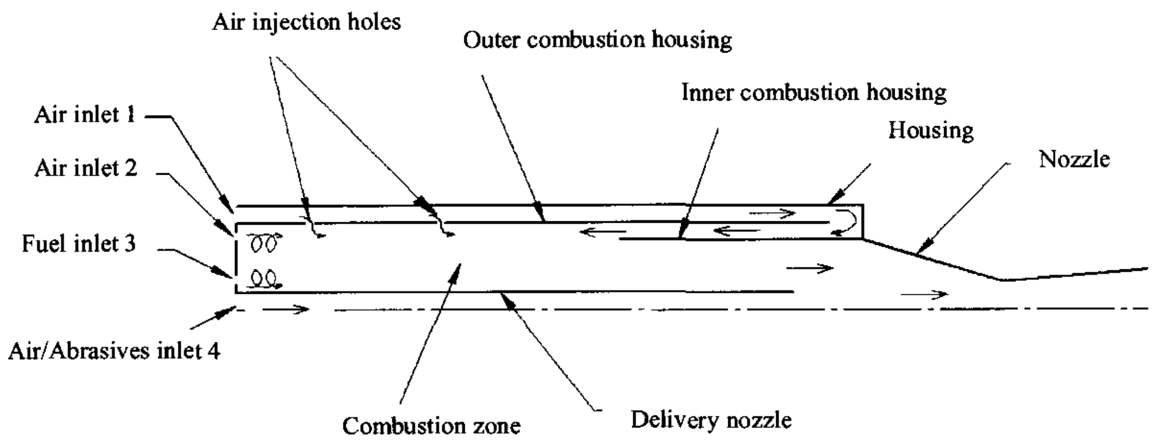

Figure 5.1. Schematic of a half cross section of the model

The outer housing was specified as a *non-slip wall* with the turbulence parameters. The delivery nozzle and the combustion housings where modelled as *baffles* (zero thickness cells). For the generic nozzle model, the nozzle was specified as a *non-slip wall* with the heat flux to account for cooling and radiation properties. For the 70 mm nozzle model, the nozzle wall and the cooling air streams were modelled with solid and fluid cells respectively. This was done in order to execute a conjugate heat transfer analysis in solids.

The following modelling strategy was used:

- cylindrical coordinate system with hexahedral cells,
- inlet, outlet, cyclic and wall boundary conditions,
- steady, compressible and non-isothermal flow options,
- combustion models with the PPDF analysis and 3-stage chemical reaction,
- the standard k-ε turbulence and RNG models for the turbulence characteristics,
- walls with the heat flux, radiation and material properties,
- two-phase Lagrangian model for particles.

The physical properties of air are assumed were set as follows:

- air was assumed to be composed of 23,2% oxygen and 76,8% nitrogen, by mass,
- the pressure was 5 bar,
- the temperature was 293 K,
- the density varied according to Presumed Probability Density Function (PPDF) with pressure,

- the molecular viscosity was $1{,}81\cdot 10^{-5}$ Pa s,
- the specific heat at 300 K was 1006 J/kg K,
- the thermal conductivity was $2{,}637\cdot 10^{-2}$ W/m K.

5.3 Meshing and Boundary Conditions

The thermal gun model dimensions were taken from the physical model designed previously (Fig. 5.2). A mesh of finite volumes was constructed using hexahedral cells having the following dimensions:

- 10° sectors in the combustion chamber cross section with 1mm radius segments,
- 2 mm on the length along the model length.

The total number of cells of the initial model varies from 15 000 to 27 000 depending on the nozzle length (Fig. 5.3). A grid-sensitive study was done after the initial solution was obtained. The results of the grid-refinement are shown in Section 5.6.

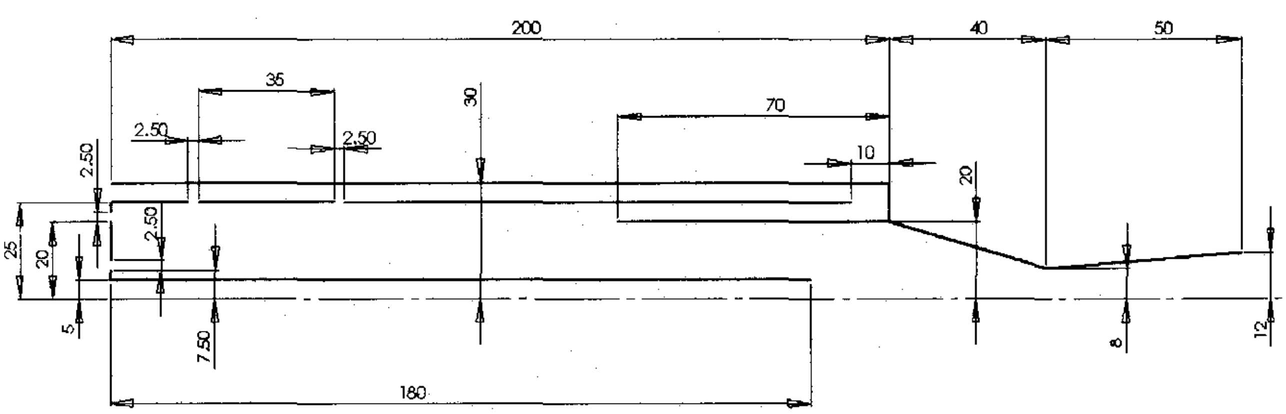

Figure 5.2. Schematic of a half cross section of the model with the dimensions

The delivery nozzle, the outer and inner combustion housings where modelled as *baffles* with the injection holes as shown in Figure 5.4 in blue colour.

accumulates much less heat flux than 150 mm long nozzle. Therefore, it is believed that the temperature does not exceed the critical level for oxidation of cobalt.

The WC nozzles were made by Powder Industries (Pty) Ltd. A semi-quantitative EDS (weight percent) analysis showed: 89,9% W, 8,7% Co and 1,4% Ti. Atomic proportions were as follows: 74% W, 22% Co and 4% Ti.

The temperature of the outer surface of the WC nozzles was measured with a thermocouple connected to a computer, which was running *PICO Technology* software for recording temperatures. All the thermal gun settings were similar to industrial trials. The recording time interval was set to 1 second. The graph of temperature is shown in Figure 7.6. The temperature recordings were done for heating up and cooling down stages of the thermal gun operation with free cooling of the nozzle. The thermal gas was started, and when the temperature stabilised the gun was turned off and recordings were continued to observe temperatures while cooling the nozzle down.

Referring to Figure 7.6, point 1 represents the start of the thermal gun. In approximately 20 seconds the temperature of the outer surface jumped by 60°C (point 2). Then, there was a period of stability for about 60 seconds (point 3). After that the temperature jumped again to 220°C in 20 seconds (point 4) and stabilised at 240°C. The total time from the start of the thermal gun was approximately 2 minutes.

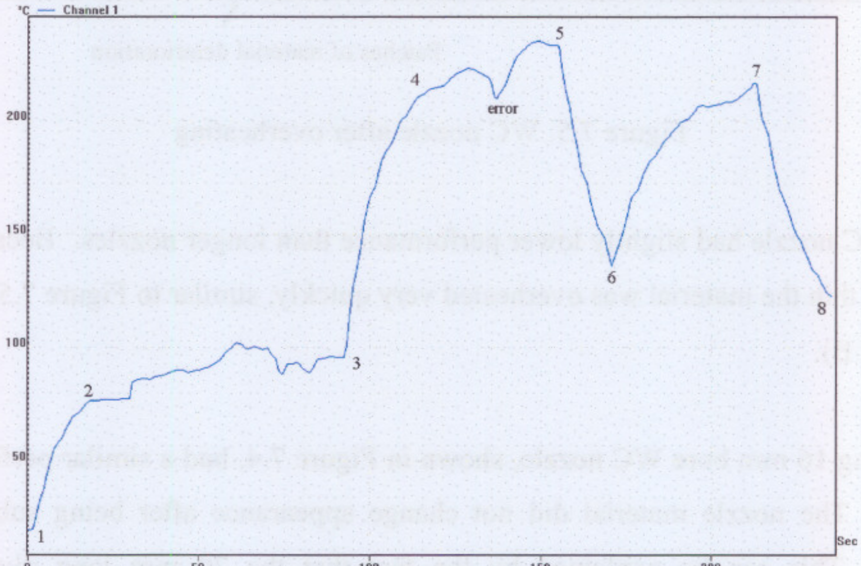

Figure 7.6. Recorded nozzle outer surface temperatures

When the thermal gun was turned off (point 5) the temperature sharply deceased from 240°C to 130°C within 10 seconds (point 6). Then the outside temperature increased to 220°C for 50 seconds (point 7). And after that the temperature started to decrease (point 8). The temperature graph shows that there are a number of sharp changes of temperature in heating up and cooling down.

Figure 7.7 shows the results of the finite element analysis of the short WC nozzle. Two nodes temperatures are shown, outer node and inner node of the nozzle. This model was developed for the low temperature range of the thermal gun. This graph corresponds with the actual results obtained from the tests (270°C) for the outer surface temperature. In the FEA results, it appears that the temperature of the inner surface node follows some oscillatory behaviour in the first 25 seconds before it stabilises. This can be some kind of a numerical phenomenon attributed to ALGOR software code. For example, ALGOR software uses thermal *stiffness*, which is basically the conduction of the thermal boundary element determined as follows:

$$Stiffness = \frac{1000000 \cdot \text{Thermal conductivity of material}}{\text{Average length of diagonal across element}} \qquad [7.1]$$

However, in this case, thermal *stiffness* is unknown because a node temperature can fluctuate to a certain degree due to a conduction coefficient, which depends on the flow velocity.

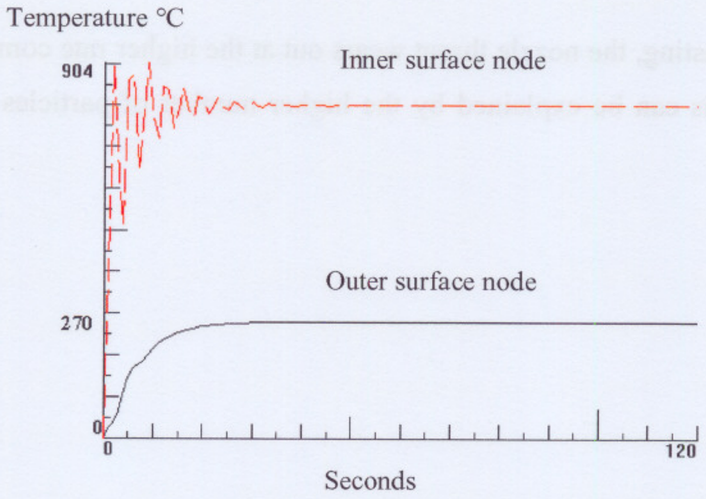

Figure 7.7. FEA temperature graph

The results of a conjugate heat transfer of STAR-CD software showed much higher temperature of the nozzle outer surface for free convection (600°C) than in the experiments. This can be explained by a relatively large computational grid of the solid material in the CFD model.

7.4 Nozzle Wear Tests

No data on wear was obtained for the hot pressed SiC and SIALON nozzles because the nozzles cracked. The SIALON nozzles, which withstood thermal shock for some time, did not wear out when blasting with fine abrasives (0,6 mm). But, when blasting with coarse abrasives (1,2 mm), the SIALON nozzle tended to wear, which is believed to have been caused by micro cracks.

The WC nozzles showed good resistance to abrasion even at much higher particle velocities. During the trails, the WC nozzle did not show any wear after 3 tons of abrasives were put through the nozzle. It is believed that the reason for slower wear of the thermo-abrasive nozzles is a relatively low volume of abrasives per unit time compared to conventional blasting.

The nozzle wear mechanism is also different compared to conventional blasting. In the thermo-abrasive blasting, the nozzle throat wears slower than the nozzle exit. This can be explained by considerably higher particle velocities at the nozzle exit than at the throat.

In conventional blasting, the nozzle throat wears out at the higher rate compared to other sections of the nozzle. This can be explained by the higher number of particles per unit area of cross section of nozzle.

8. CONCLUSIONS

The analytical and computational models show a close correlation between the simulated and the actual characteristics of the flow, such as: velocities, thrust and temperatures. The CFD model showed a stable combustion process within the small combustion area of the thermal gun and this was confirmed by tests on the working prototype of the advanced thermal gun.

The nozzle models were verified on the real nozzles. The nozzle bore geometry was developed by means of modelling and empirically. The stable combustion and high blasting performance was achieved with a nozzle bore diameter of 14 - 16 mm for the thermal gun with a 48 mm diameter of the combustion chamber.

From the analytical and computational models, the flow parameters in the nozzle were obtained. According to the results of the modelling the temperature of the inner surface of the diverging section of a blasting nozzle can reach 800°C to 1100°C within first 100 seconds from the start of the system while the outer surface of a nozzle is at much lower temperatures. This creates temperature gradients in the nozzle especially if the nozzle material has low thermal conductivity. The time interval for the temperature rise was confirmed by experiments.

The thermo-jet nozzle is subjected to different kinds of thermal shock. The most severe thermal shock occurs at the start of the system. Another kind of thermal shock takes place when combustion is interrupted, then the nozzle is subjected to quenching thermal shock from the relatively cold compressed air. Ceramics are known for low resistance to quenching. Some ceramic nozzles broke during the quenching experiments.

During sudden shutdown of the system, when there is no cooling air at all, the nozzle material is also subjected to a thermal shock, which can be even more detrimental to the nozzle. In this situation, the heat from the thermal gun internal components, such as the combustion chamber housings and the nozzle holder is transferred to the nozzle in the places of contact. The heat flux is applied to the relatively small area of the nozzle. This creates local sites of heat concentration. During the experiments, when the gun was shut off completely, the outer surface temperature dropped sharply by 100°C within 5 seconds and then rose again by 100°C during the next 10 seconds (Figure 7.5). This results in the localised contraction and expansion in the material structure leading to cracks in the nozzle material.

It is concluded that for the initial thermal shock, it does not matter if the outer surface of the nozzle is cooled down naturally or by forced cooling. However, during the prolonged operation of the thermal gun, forced cooling is essential for the WC nozzles to prevent oxidation of the cobalt.

The ceramic nozzles were made of hot pressed SiC, wet cast nitride-bonded SiC and SIALON. The geometries of the ceramic nozzles were chosen according to the limitations of the manufacturing processes, having the nozzle bore diameter of 16 mm, the diverging section of 100 mm long with the included angle of 3°. The hot pressed SiC, and SIALON nozzle materials failed in thermal loading during the start of the system, which is attributed to the material properties and the manufacturing processes. The wet cast nitride-bonded SiC showed better thermal shock resistance properties, but the material structure was too porous for sandblasting nozzles.

The WC nozzles showed overall good results in thermal shock resistance and mechanical wear. The nozzle bore diameters of 14, 15 and 16 mm were tested depending on the power output of a compressor. The 14 mm nozzle bore diameter is recommended with air compressors producing less than 250 cubic feet per minute (CFM). For 400 CFM compressors, the 15 mm nozzle bore diameter is the most suitable, and 16 mm nozzle bore diameter should be used for 700 – 1000 CFM compressors.

The nozzles with the lengths of nozzle diverging section between 0 and 50 mm showed low rates of blasting because abrasives did not gain acceleration. The nozzles with 70 – 150 mm long diverging sections achieved high cleaning rates. However, the 150 mm long WC nozzles deteriorated on the outer surface at high temperatures, possibly due to oxidation of the cobalt. The inner surface of the WC nozzles did not show any sign of oxidation. This could be explained by lower concentration of oxygen in the combustion gas.

The length of the nozzle diverging section is an important factor in determining particle velocity and blasting productivity. Although the particle velocity increases with nozzle length, the rate of velocity increase does not justify the length of the diverging section of thermo-abrasive nozzles above 70 – 100 mm. Furthermore, a long diverging section is overheated by the combustion gas and may result in a nozzle material deterioration.

For general abrasive blasting, the included angle of the diverging section should be $3^{\circ} - 5^{\circ}$ to cover a wider area. In the case of hard coating removal, a straight bore nozzle should be used as it gives more cutting energy.

The new design of the thermal gun proved to be more efficient and versatile than the initial design. The new method of mixing air and fuel increases power output. The advanced thermal gun has outperformed the initial thermal gun in all tests. The new ignition method using a flame glow plug proved to be reliable and consistent.

The CFD model can be used in further studies, such as: stress analysis of combustion housings, design of HVAF systems, effects of different abrasive media on productivity, etc.

Future Work

This study of the thermo-abrasive gun and the nozzle should be taken further to thermal spraying applications. The existing thermal spraying process is expensive due to the cost of equipment and consumables. The thermo-abrasive gun is much cheaper to run because it uses only compressed air and paraffin/diesel. The fuel consumption is approximately 5 litres per hour.

It is envisaged that the WC nozzle can be used for metal spraying applications without water cooling. This would make the system simpler and more economical. For example, the copper nozzle used for thermal spraying, lasts approximately 100 hours.

The reason why HVAF systems are not used in thermal spraying is that up to now there were no reliable working thermal guns. The initial trials of thermal spraying using the thermal gun described in this study, showed good results regarding speed and quality of spraying.

In future work on thermal spraying, the following should be investigated:

1. WC nozzles with emphasis on adhesion of molten materials such as metals, cermets and ceramics
2. Nozzle wear using different coating materials and parameters
3. Productivity and quality of coating

9. REFERENCES

Bilger, R.W., 2000. Future progress in turbulent combustion research. *Progress in Energy and Combustion Science*, Vol. 26, pp. 367-380.

Botto, D., Zucca, S., Gola, M.M., 2003. A methodology for on-line calculation of temperature and thermal stress under non-linear boundary conditions. *International Journal of Pressure Vessels and Piping*, 80, pp. 21–29.

Browning, J., 1994. *Extreme energy method for impacting abrasive particles against a surface to be treated*. US Patent 5,283,985.

Browning, J., 1983. *High Velocity Flame Jet Internal Burner for Blast Cleaning and Abrasive Cutting*. US Patent 4,384,434.

Butters, G., 1981. *Plastic Pneumatic conveying and bulk storage*. New York: Appl. Sci. Pub., 247 p.

Cohen, H., Rogers, G.F.C., Saravamuttoo, H.I.H., 1996. *Gas turbine theory*. Cornwall: Addison Wesley Longman, 414 p.

Crowe, C., Sommerfeld, M., Tsuji, Y., 1998. *Multiphase flows with droplets and particles*. London: CRC Press, 496 p.

Drotsky, J.G., 1994. *Strength of material for technicians*. 3rd ed. Durban: McGraw-Hill, 372 p

El Tahry, S.H., 1983. k- ε equation for compressible reciprocating engine flows. *AIAA*, *J. Energy*, 7(4), pp. 345–353.

Evans, A.G., Marshall, D.B., 1980. Wear mechanism in ceramics. *Fundamentals of friction and wear of materials, ASM*, pp. 439-452.

Evdokimenko, Y., et al. 1997. *High Velocity Flame Jet Apparatus for Thermoabrasive Cutting or Cleaning or for the Application of Protective Coatings*. US Patent 5,607,342.

Galchenko, L., et al., 1982. *Method of thermal treatment of components.* N 967144, Krivoy Rog: Krivoy Rog Gorny Institute.

Glandus, J.C., 1981. *Rupture fragile et resistance aux chocs thermiques de ceramiques a usages mecaniques.* Ph.D.dissertation, University of Limoges.

Glushko, V., et al., 1973. *Thermodynamic and thermo physical characteristics of fuels.* Moscow.

Haworth, D.C., et al. 2000. Numerical simulation of turbulent propane–air combustion with nonhomogeneous reactants. *Combustion and Flame, The Combustion Institute,* 121, pp. 367 – 417.

Huber, N., and Sommerfeld, M., 1998. *Modelling and numerical calculations of dilute-phase pneumatic conveying in pipe systems.* Powder Technology, pp.90-101.

John J., 1984. *Gas Dynamics,* 2nd edition. Englewood Cliffs, N.J.: Prentice Hall, 464 p.

Kaleberda, V., et al. 1982. *Method of engineering calculations of generators of gaseous jets.* Kharkov: Kharkov Aviation Institute, 86 p.

Kamiya, H., Sekiya,Y., Horio M., 2001. Thermal stress fracture of rigid ceramic filter due to char combustion in collected dust layer on filter surface. *Powder Technology* 115, pp. 139–145.

Kesler, O., et al. 1998. Measurement of residual stress in plasma-sprayed metallic, ceramic and composite coatings. *Materials Science and Engineering,* A257, pp. 215–224.

Kingery, W.D., 1955. Factors affecting thermal stress resistance of ceramic materials. *Journal of American Ceramic Society,* pp. 3 –15&38.

Kocabicak, U., et al. 1999. Comparison of the developed thermal stress in $Al_2 0_3$-SG, ZrO_2-12%Si + Al and ZrO_2-SG coating systems subjected to thermal loading. *Materials and Design 20,* pp. 287–290.

Kotov, S., Gorlach, I.A., Dubetsky, I., 2000. *Materials treatment apparatus and process.* South African Patent 2000/2862.

Launder, B.E., Spalding, D.B., 1974. The numerical computation of turbulent flows. *Comp. Meth. in Appl. Mech. and Eng.*, 3, pp. 269-289.

Metselaar, H.S.C, et al. 2002. Wear of ceramics due to thermal stress: a thermal severity parameter. *Wear* 249, pp. 962–970.

Moran, M.J., Shapiro, H.N., 1998. *Fundamentals of engineering thermodynamics.* New York: John Wiley & Sons, Inc., 896 p.

Mostaghimi, J., et al. 2003. Modelling thermal spray coating processes: a powerful tool in design and optimization. *Surface and Coatings Technology* 163 –164, pp. 1 –11.

Oberkampf, W.L., et al. 1996. *Journal of Thermal Spray Technologies.* 5, pp. 53 –81.

Ozisik, M.N., 1985. *Heat Transfer. A Basic Approach.* Singapore: McGraw Hill, 576 p.

Panda, P.K., 22, et al. 2002. Thermal shock and thermal fatigue study of alumina, *Journal of the European Ceramic Society*, pp. 2187 – 2196.

Panda, P.K., et al. 2002. Thermal shock and thermal fatigue study of ceramic materials on a newly developed ascending thermal shock test equipment. *Science and Technology of Advanced Materials* 3, pp. 327–334.

Patankar, S. V., 1980. *Numerical Heat Transfer and Fluid Flow.* Washington, D.C.: Hemisphere Pub., 197 p.

Rauenzahn, R.M., Tester, J.W., 1991. Numerical simulation and field testing of flame-jet thermal spallation drilling. *Model development, Int. J. Heat Trans.*, 3493, pp. 895-808.

Reitz, R.D., Rutland, C.J., 1995. Development and testing of diesel engine CFD models. *Progress in Energy and Combustion Science*, Vol. 21, pp. 173-196.

Richardson, J.M., Howard, Jr., H.C., and Smith, R.W., 1953. The relation between sampling tube measurements and concentration fluctuations in a turbulent gas jet. *4th Symp. on Combustion*, pp. 814-817.

Sabadash, V., 1982. *Specifics of designing generators of gaseous jets.* Kharkov: Kharkov Aviation Institute, 86 p.

Saxena, V., Pope, S.B., 1999. PDF Simulations of turbulent combustion incorporating detailed chemistry. *Combustion and Flame, The Combustion Institute,* 117, pp. 340 –350.

Schwetz, K.A., 1995. Wear of boron Carbide Ceramics by abrasive waterjets. *Wear = Usure =Verschleiss, Vol,* 181-183, pp. 148-155.

Seavey, M., 1985. Abrasive blasting above 100 psi. *Journal of Protective Coatings & Linings,* USA, pp. 26 -37.

Settles, S., Garg, S., 1995. A Scientific view of the productivity of abrasive blasting nozzles. *Journal of Protective Coatings & Linings.* USA, pp. 28 -101.

Shigietaka, W., et al., 1993. The Effect of Impact Angles of Jet Streams in the Abrasive Water Jet Cutting of SiN Ceramics. *Journal of the Ceramic Society of Japan,* Vol, 101, pp. 1265-1269.

Sinha, N., et al., 1995. *Proceeding of the 8th National Thermal Spray Conference.* Houston, pp. 199 –206.

Tashiro, et al., 1995. Numerical prediction of saltation velocity for gas-solid two-phase flow in horizontal pipe, *ASME Fluids Engineering Conference.* USA ASME, Vol, 228, pp. 135-140.

Turns, S.R., 2000. *An Introduction to Combustion.* 2nd Ed. Boston: McGraw Hill, 676 p.

Ucar, V., et al. 2001. Use of the finite element technique to analyze the influence of coating material, material phase state and the purity on the level of the developed thermal stresses in plasma coating systems under thermal loading conditions. *Surface and Coating Technology,* 142-144, pp. 950 – 953.

Varushin, V., 1973. *Thermal gun,* N 1712-5, Krivoy Rog: Krivoy Rog Gorny Institute.

Veynante, D., Vervisch, L., 2002. Turbulent combustion modeling. *Progress in Energy and Combustion Science,* 28, pp. 193-266.

Warsi, Z.V.A., 1981. Conservation form of the Navier-Stokes equations in general nonsteady coordinates. *AIAA Journal,* 19, pp. 240–242.

Weibull, W., 1939. A statistical theory of the strength of materials. *Proc Roy Swedish Inst Engng* Res; 151, pp. 1 –45.

White, R., 1996. *Air and Fuel Mixing Chamber for a Tunable Velocity Thermal Spray Gun.* US Patent 5,520,334.

Wilkinson, M.A., Tester, J.W., 1993. Experimental measurement of surface temperatures during flame-jet induced thermal spallation. *Rock Mech. Rock Engng.* 26(1), pp.29-62.

Yakhot, V., et al. 1992. Development of turbulence models for shear flows by a double expansion technique. *Phys. Fluids*, A4(7), pp. 1510–1520.

Zhou, Y.C., Hashida, T., 2001. Coupled effects of temperature gradient and oxidation of thermal stress in thermal barrier coating systems. *International Journal of Solids and Structures.* 38, pp. 4235 – 4264.

APPENDIX A

NUMERICAL MODELLING OF THE THERMAL GUN

1. Flow Parameters

The calculations shown below are based on the analytical modelling done in Section 3.

A typical air compressor, used for abrasive blasting, produces a volumetric flow rate of 6 m^3/min at 5 bar pressure. By using flow meters fitted to both air lines, it was determined that approximately 65% of the entrant flow goes directly to the combustion chamber and 35% to propel abrasives. This corresponds to mass flow rates of 0,08 kg/s and 0,04 kg/s respectively.

From the practical experiments it was found that approximately 4 kg of abrasives were used per minute of blasting, i.e. M_d = 4 kg/min = 0,066 kg/s. The air flow rate is $M_c = m_{airp}$= 0,04 kg/s.

The total loading is

$$z = \frac{M_d}{M_c} = \frac{0{,}066}{0{,}04} = 1{,}67 \qquad \text{[A.1]}$$

where M = mass flow rates of dispersed (M_d) and continuous (M_c) phases, kg/s

Then, the mass flow rate of the air/abrasive mixture with loading Z is

$$m_{abr} = m_{airp}(1+Z) = 0{,}04 \cdot (1+1{,}67) = 0{,}106 \,\text{kg/s} \qquad \text{[A.2]}$$

The density of the mixture using equation [3.23] is

$$\rho_{abrmix} = \alpha_{air}\rho_{air}(1+z) = 0{,}9995 \cdot 1{,}2 \cdot (1+1{,}67) = 3{,}20 \ \text{kg/m}^3 \qquad \text{[A.3]}$$

The ratio of the distance between the particles to the particle average diameter using equation [3.24] is

$$\frac{l}{D_d} = \left(\frac{\pi}{6} \cdot \frac{1+\alpha_{abr}}{\alpha_{abr}}\right)^{\frac{1}{3}} = \left(\frac{\pi}{6} \cdot \frac{1+0{,}0005}{0{,}0005}\right)^{\frac{1}{3}} = 10{,}13 \qquad \text{[A.4]}$$

Because the ratio is greater than 10 the flow is considered dispersed. In this case, individual particles could be treated as isolated particles with little influence of the neighbouring elements on the drag or heat transfer rate.

At 300 K the specific heat of the air/abrasive mixture from equation [3.25] is

$$c_{p_m} = c_{p_{air}} \frac{1 + z\dfrac{c_{p_d}}{c_{p_{air}}}}{1+z} = 1007 \frac{1 + 1{,}67 \cdot \dfrac{1080}{1007}}{1 + 1{,}67} = 1052 \text{ J/kg K} \qquad \text{[A.5]}$$

where $c_{p_{air}}$ = the specific heat of air, $c_{p_{air}}$ =1007 J/kg K at 300 K [Turns, 200:653],

c_{p_d} = the specific heat of $Al_2 0_3$, c_{p_d} = 1080 J/kg K [Kocabicak, 1999:288].

The gas constant of the air/abrasive mixture from equation [3.26] is

$$R_{cold} = \frac{c_{p_m}(\gamma - 1)}{\gamma} = \frac{1052 \cdot (1{,}4 - 1)}{1{,}4} = 300 \text{ J/kg K} \qquad \text{[A.6]}$$

where R_{cold} = the gas constant of the air/abrasive stream, further called a cold stream,

γ = the ratio of specific heats, γ = 1,4 for ideal gas properties of air [Moran, 1998:755].

Referring to Figure 3.4, the dimensions of the thermal gun were taken from the initial thermal gun design. Assuming isentropic flow the properties of the cold and hot flows are as follows:

(a) The properties of the cold stream are:

$m_{cold} = m_{abr}$ = 0,106 kg/s

T_{cold} = 300 K

$p_{cold} = p_{hot}$

D_{cold} = 9,5 mm (A_{cold} = 0,113 10^{-3} m^2)

(a) The properties of the hot stream are:

$m_{hot} = m_{com}$= 0,08 kg/s

$T_{hot} = 1800$ K

$p_{hot} = p_{cold}$

$D_{hot} = D_{chamber} - D_{cold}$ ($A_{hot} = 0{,}118\ 10^{-2}\ m^2$)

(c) The properties of the mixed stream at the entry of the nozzle are denoted as:

$m_3 = m_{cold} + m_{hot}$

T_3

p_3

$D_3 = 40$ mm ($A_3 = 0{,}126\ 10^{-2}\ m^2$)

The left-hand-side of the momentum equation [3.27] is calculated first.

The stagnation pressure and temperatures of the hot stream need to be calculated. A Mach number inside a combustion chamber is assumed. Selecting the Mach number of $M = 0{,}3$ and using equation [3.15] the pressure ratio is:

$$\frac{p_0}{p_{hot}} = \left[1+\left(\frac{\gamma-1}{2}\right)\cdot M^2\right]^{\frac{\gamma}{\gamma-1}} = \left[1+\left(\frac{1{,}333-1}{2}\right)\cdot 0{,}3^2\right]^{\frac{1{,}333}{1{,}333-1}} = 1{,}06 \qquad \text{[A.7]}$$

The stagnation pressure becomes.

$$p_{hot} = \frac{p_0}{1{,}06} = \frac{0{,}8}{1{,}06} = 0{,}752\,\text{MPa} \qquad \text{[A.8]}$$

where p_0 = the pressure inside the combustion chamber, MPa

The temperature ratio from equation [3.31] is

$$\frac{T_0}{T_{hot}} = \left[1+\left(\frac{\gamma-1}{2}\right)\cdot M^2\right] = \left[1+\left(\frac{1{,}333-1}{2}\right)\cdot 0{,}3^2\right] = 1{,}2 \qquad \text{[A.9]}$$

The stagnation temperature is

$$T_{hot} = \frac{T_0}{1{,}2} = \frac{1800}{1{,}2} = 1773\,\mathrm{K} \qquad [A.10]$$

where: T_0 = the temperature inside the combustion chamber, K

The stagnation velocity of the hot stream is then

$$U_{hot} = \frac{m_{hot} \cdot R_{gas} \cdot T_{hot}}{p_{hot} \cdot A_{hot}} = \frac{0{,}08 \cdot 287 \cdot 1773}{752 \cdot 10^3 \cdot 0{,}00118} = 47 \text{ m/s} \qquad [A.11]$$

where: R_{gas} = the gas constant, for combustion gas, R_{gas} = 287 J/kg K [Cohen, 1996:56]

The stagnation velocity of the cold stream is

$$U_{cold} = \frac{m_{cold} \cdot R_{cold} \cdot T_{cold}}{p_{cold} \cdot A_{cold}} = \frac{0{,}106 \cdot 300 \cdot 300}{752 \cdot 10^3 \cdot 0{,}000113} = 109 \text{ m/s} \qquad [A.12]$$

The right-hand side of the momentum equation [3.27] is calculated as shown below.

$$\begin{aligned}&(m_{cold}U_{cold} + p_{cold}A_{cold}) + (m_{hot}U_{hot} + p_{hot}A_{hot}) = \\ &= (0{,}106 \cdot 109 + 752 \cdot 10^3 \cdot 0{,}113 \cdot 10^{-3}) + (0{,}08 \cdot 47 + 752 \cdot 10^3 \cdot 0{,}118 \cdot 10^{-2}) = 983\end{aligned} \qquad [A.13]$$

From the tables [Moran, 1998:757] the enthalpy of the mixture is

$$h_{mix} = h_{hot} - h_{cold} = h_{1773} - h_{300} = 2003{,}3 - 300{,}16 = 1700{,}14 \text{ kJ/kg K} \qquad [A.14]$$

From the ideal gas table [Moran, 1998:757] the stagnation temperate of the mixture is $T^0_{mix} = 1500\,\mathrm{K}$.

The mass flow of the mixture at the nozzle entry is

$$m_3 = m_{cold} + m_{hot} = 0{,}106 + 0{,}08 = 0{,}186 \text{ kg/s} \qquad [A.15]$$

In order to find the mixture pressure and temperature a number of iterations are required. These are necessary to balance the momentum equation because there are two unknowns. First the Mach number is guessed, $M = 0,3$. Then the temperature of the mixture is found using equation [3.29]

$$\frac{T_{mix}^0}{T_3} = \left[1 + \left(\frac{\gamma - 1}{2}\right) \cdot M^2\right] = \left[1 + \left(\frac{1,333 - 1}{2}\right) \cdot 0,3^2\right] = 1,015 \quad [A.16]$$

$$T_3 = \frac{T_{mix}^0}{1,008} = \frac{1500}{1,008} = 1477\,\text{K} \quad [A.17]$$

In order to determine the pressure of the mixture the velocity is chosen $U_3 = 80$ m/s. The pressure is then

$$p_3 = \frac{m_3 \cdot R_{mix} \cdot T_3}{A_3 \cdot U_3} = \frac{0,186 \cdot 300 \cdot 1477}{0,126 \cdot 10^{-2} \cdot 80} = 0,775\,\text{MPa} \quad [A.18]$$

The right hand side of equation [3.27] is then

$$0,186 \cdot 80 + 775180 \cdot 0,126 \cdot 10^{-2} = 987 \text{ kg m/s} \quad [A.19]$$

The value of the left hand side of equation [A.13] was 983 kg m/s. The values of equations [A.19] and [A.13] are relatively close. This means that the momentum equation is balanced.

The calculated flow characteristics at state 3, which is at the entry to the nozzle, are as follows:
$m_3 = 0,186$ kg/s
$T_3 = 1477$ K
$p_3 = 0,775$ MPa
$A_3 = 0,126\ 10^{-2}$ m^2

2. Critical Diameter of the Nozzle

Assuming constant specific heat the pressure ratio between the states 3 and 4 using equation [3.37] is

$$\frac{p_{03}}{p_4}=\frac{1}{\left[1-\frac{1}{\eta}\left(\frac{\gamma-1}{\gamma+1}\right)\right]^{\gamma/(\gamma-1)}}=\frac{1}{\left[1-\frac{1}{0.95}\left(\frac{1.333-1}{1.333+1}\right)\right]^{1,333/(1,333-1)}}=1,914 \quad [A.20]$$

where η = the efficiency of the combustion process, which is considered to be nearly complete, η = 0,95

The critical pressure or the pressure at the nozzle throat is

$$p_4=\frac{p_{03}}{1,914}=0,775\cdot 0,52=0,403\,\text{MPa} \quad [A.21]$$

Since the area of the nozzle throat is unknown it is necessary to calculate the temperature at the exit first, which is found from the ratio and the temperature in a combustion chamber as follows:

$$T_4=T_{03}\cdot\left(\frac{2}{\gamma+1}\right)=1477\cdot\left(\frac{2}{1,333+1}\right)=1266\,\text{K} \quad [A.22]$$

The mixture density in the nozzle throat is

$$\rho_4=\frac{p_4}{RT_4}=\frac{403\cdot 10^3}{300\cdot 1266}=1,06\,\text{kg/m}^3 \quad [A.23]$$

where R = the gas constant of the final mixture, $R = R_{cold}$ = 300 J/kg K

The gas velocity in the nozzle throat is

$$U_4=\sqrt{(\gamma\cdot R\cdot T_4)}=\sqrt{1,333\cdot 300\cdot 1266}=711\ \text{m/s} \quad [A.24]$$

The throat area per mass flow is determined as follows:

$$A_S=\frac{A_4}{m}=\frac{1}{\rho_4\cdot U_4}=\frac{1}{1,06\cdot 711}=0,001325\ \text{m}^2\cdot\text{s/kg} \quad [A.25]$$

The nozzle throat area and the diameter are determined using equation [A.25] as follows:

$$A_{throat} = A_4 = m \cdot A_S = 0{,}18 \cdot 0{,}001325 = 0{,}000239 \text{ m}^2 \qquad \text{[A.26]}$$

$$D_{throat} = \sqrt{\frac{4 \cdot A_4}{\pi}} = \sqrt{\frac{4 \cdot 0{,}000239}{\pi}} = 0.0174 \,\text{m} \qquad \text{[A.27]}$$

The specific thrust using equation [3.45] is

$$F_s = (U_4 - U_3) + \frac{A_4}{m}(p_4 - p_a) = (711 - 80) + 0{,}001325 \times (403 - 100) \times 10^3 = 1032 \,\text{N s/kg} \qquad \text{[A.28]}$$

The full thrust using equation is:

$$F = m \cdot F_S = 0{,}18 \cdot 1032 = 186 \text{ N} \qquad \text{[A.29]}$$

3. Geometry of Nozzle Bore

In the above section the nozzle was considered as a converging nozzle with the exit at the critical diameter $D_{throat}= D_4$. In this section the complete converging-diverging nozzle geometry is calculated. The nozzle throat diameter was determined using equation [A.27] as 17,4 mm. The nozzle throat wears out by abrasives to a bigger size, therefore, the diameter should be made at the lower limit. The 16 mm size of the critical diameter was chosen for modelling. Ideally the nozzle should have smooth curves. In practice, the geometry of the nozzle is simplified (Fig. A.1).

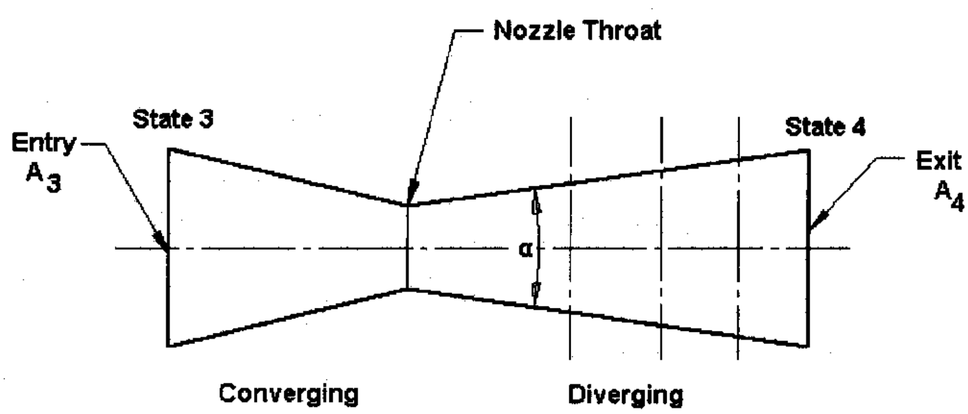

Figure A.1 Diagram of the simplified Laval nozzle

The relationship between the change of nozzle diameter along the axis and a velocity of flow (Mach number) is determined from [3.19]. Tables with the variations of A/A^* with M are given in literature [Moran, 1998:432].

The length of the diverging portion of the nozzle was considered to be 100 mm. Three exit diameters were examined. These were 24, 26 and 27 mm. The sizes correspond to the included nozzle angles of approximately 4,6°, 5,7° and 6° respectively. The atmospheric pressure was taken as 0,101 MPa. The calculations are as follows:

For D_4 = 24 mm $\frac{A_4}{A^*} = \frac{24}{16} = 1{,}5$ [A.30]

For the area ratio of 1,5 the Mach number, the temperature and pressure ratio are found from the Table [Moran, 1998:432].

$$M_4 = 1{,}85$$
$$\frac{T_4}{T_3} = 0{,}59$$
$$\frac{p_4}{p_3} = 0{,}160$$

The corresponding values of the pressure, the temperature and the velocity at the exit are:

$$T_4 = T_3 \cdot 0{,}59 = 1477 \cdot 0{,}59 = 871\,\mathrm{K} \quad \text{[A.31]}$$

$$p_4 = p_3 \cdot 0{,}16 = 0{,}775 \cdot 0{,}16 = 0{,}124 > 0{,}101\,\mathrm{MPa} \quad \text{[A.32]}$$

$$U_4 = M_4 \cdot \sqrt{\gamma \cdot R \cdot T_4} = 1{,}85 \cdot \sqrt{1{,}4 \cdot 300 \cdot 871} = 1118\,\mathrm{m/s} \quad \text{[A.33]}$$

Since the backpressure is greater than the atmospheric pressure $p_4 > p_{atm}$ the flow is *underexpanded*. This means that the exit diameter is too small.

For D_4 = 27 mm $\frac{A_4}{A^*} = \frac{27}{16} = 1{,}69$ [A.34]

For area ratio of 1,69, the Mach number, the temperature and pressure ratio from the table [Moran, 1998:432] are

$$M_4 = 2$$
$$\frac{T_4}{T_3} = 0,55$$
$$\frac{p_4}{p_3} = 0,127$$

The corresponding values of the pressure, the temperature and velocity at the exit are:

$$T_4 = T_3 \cdot 0,55 = 1477 \cdot 0,55 = 812\,\mathrm{K} \qquad [A.35]$$

$$p_4 = p_3 \cdot 0,127 = 0,775 \cdot 0,127 = 0,098 < 0,101\,\mathrm{MPa} \qquad [A.36]$$

$$U_4 = M_4 \cdot \sqrt{\gamma \cdot R \cdot T_4} = 1,9\sqrt{1,4 \cdot 300 \cdot 812} = 1109\,\mathrm{m/s} \qquad [A.37]$$

Since the backpressure is less than the atmospheric pressure $p_4 < p_{atm}$ the flow is *overexpanded* and a normal shock takes place inside the nozzle. This means that the exit diameter is too big.

For $D_4 = 26$ mm $\frac{A_4}{A^*} = \frac{26}{16} = 1,62$ [A.38]

For area ratio of 1,62 the Mach number, the temperature and pressure ratio from the table [Moran, 1998:432] are

$$M_4 = 1,95$$
$$\frac{T_4}{T_3} = 0,57$$
$$\frac{p_4}{p_3} = 0,135$$

The corresponding values of the pressure, the temperature and velocity at the exit are:

$$T_4 = T_3 \cdot 0,57 = 1477 \cdot 0,57 = 841\,\mathrm{K} \qquad [A.39]$$

$$p_4 = p_3 \cdot 0{,}135 = 0{,}775 \cdot 0{,}135 = 0{,}1046\,\text{MPa} \qquad \text{[A.40]}$$

$$U_4 = M_4\sqrt{\gamma \cdot R \cdot T_4} = 1{,}95 \cdot \sqrt{1{,}4 \cdot 300 \cdot 841} = 1158\,\text{m/s} \qquad \text{[A.41}$$

The calculated backpressure is very close to the atmospheric pressure, indicating the correct exit diameter, which can be between 26 and 27 mm for a *perfectly expanded* flow. A normal shock takes place at the nozzle exit.

The real working conditions may vary. For example, the pressure and the temperature of the compressed air can fluctuate, depending on the conditions of the compressor. Therefore, in practice the nozzle throat and exit diameter can vary too. The nozzle included angle of the diverging section for these conditions should be 5° - 6°. Because the nozzle wears out the minimum range of diameters were chosen for design.

Figure A.2 shows the nozzle geometry with a fixed nozzle throat of 16 mm an included angle of 5°. The variable nozzle parameters are the length of the diverging section from 50 to 150 mm and the corresponding exit diameters. The converging section was chosen according to the available sizes of the nozzle holder of the thermal gun.

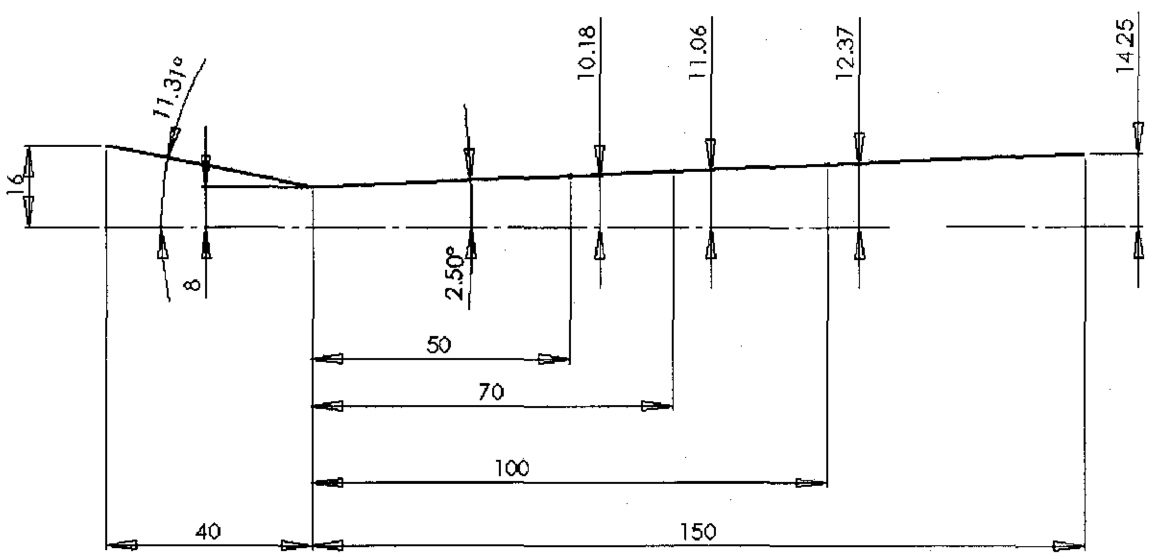

Figure A.2 Calculated optimum bore geometry of a thermo jet nozzle

APPENDIX B

NOZZLE DESIGNS

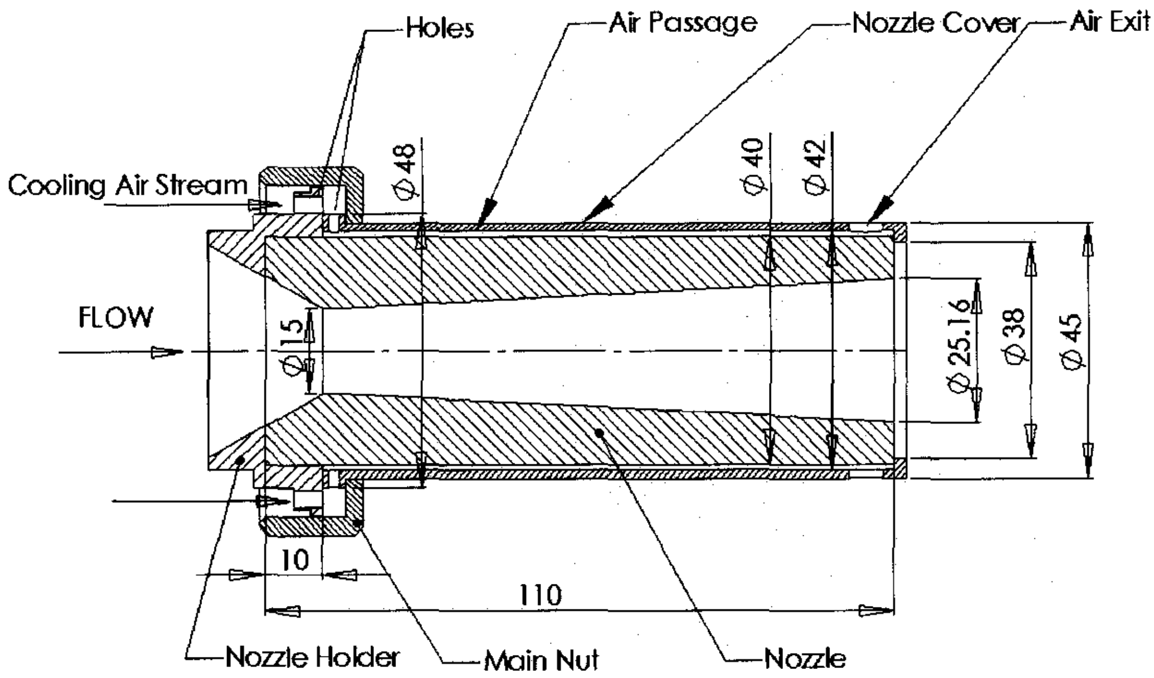

Figure B.1 Schematic section of the SiC nozzle arrangement with forced cooling

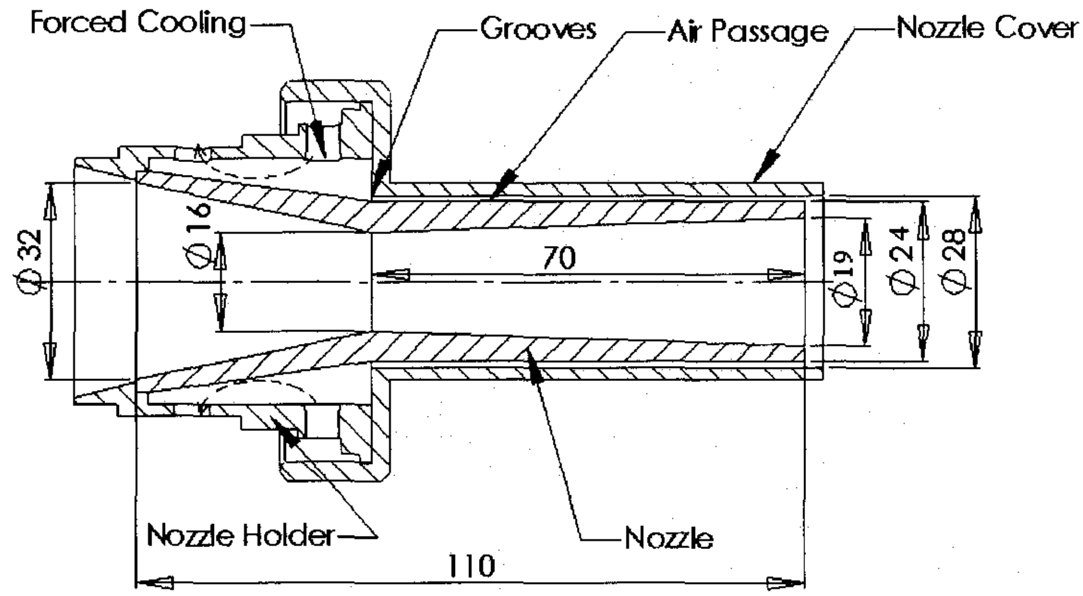

Figure B.2 Schematic section of the WC nozzle arrangement with forced cooling

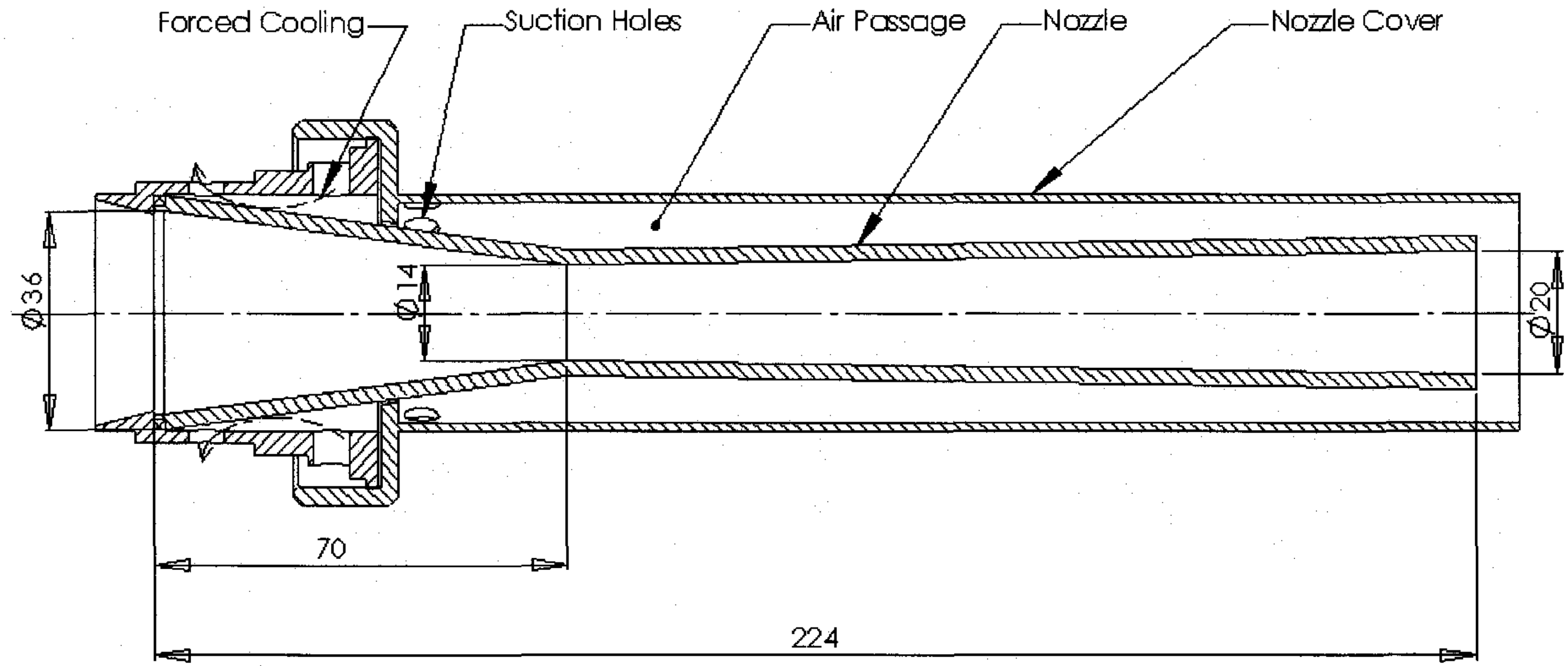

Figure B.3 Schematic section of the WC and SIALON nozzle arrangement with suction cooling